Universität Rostock

Traditio et Innovatio

Kumulative Dissertation

Directional transport in interacting Floquet systems

Helena Drüeke

Institut für Physik
Mathematisch-Naturwissenschaftliche Fakultät
Universität Rostock

Betreuer: Prof. Dr. Dieter Bauer
Gutachter: Prof. Dr. Lars Bojer Madsen

https://doi.org/10.18453/rosdok_id00004816

eingereicht und verteidigt 2024

Abstract

Floquet systems are temporally periodic systems. The periodic drive can be internal or external. An external drive might, for example, be an external laser field. An internal drive means the system itself is changing, such as the position or potential depth of lattice sites. Floquet systems can exhibit interesting effects, which would be impossible in static systems. This thesis investigates the influence of interaction on three Floquet systems.

In the first system, we show that the interaction between two particles leads to their directional transport in a system of two linear (one-dimensional) chains. This effect is only possible due to the internal Floquet drive, which, for this system, is the alternating movement of the particles.

Our second system is a two-dimensional Floquet topological insulator. Topological insulators are characterized by an insulating bulk and conducting edges. Our system, a modified Rudner–Lindner–Berg–Levin model, is topologically insulating only due to its periodic drive. We investigate a diagonal potential and find that it switches the path of the topological edge states.

The final system has a laser field as an external drive, unlike the first two systems, which have an internal drive. Two-dimensional hexagonal nanoribbons emit high-order harmonics due to their interaction with the laser. We find that the strength and polarization of these harmonics depend on the edge structure of the nanoribbons, as well as on an alternating potential on their lattice sites.

Zusammenfassung

Floquet-Systeme sind zeitlich periodische, getriebene Systeme. Der Antrieb kann intern sein, das heißt das System selbst ändert sich, wie zum Beispiel die Position der Gitterplätze oder die Tiefe ihrer Potentiale. Ein externer Antrieb kann beispielsweise ein externes Laserfeld sein. Floquet-Systeme können interessante Effekte zeigen, die in statischen Systemen unmöglich wären. Diese Dissertation untersucht den Einfluss von Wechselwirkung in drei Floquet-Systemen.

In unserem ersten System von zwei eindimensionalen Ketten führt die Wechselwirkung zwischen zwei Teilchen zu ihrem gerichteten Transport. Dieser Effekt ist nur aufgrund des internen Floquet-Antriebs möglich. In diesem System ist der Floquet-Antrieb die abwechselnde Bewegung der Teilchen.

Unser zweites System ist ein zweidimensionaler Floquet-topologischer Isolator. Topologische Isolatoren sind gekennzeichnet durch einen isolierenden Kern und leitende Ränder. Unser System, ein modifiziertes Rudner–Lindner–Berg–Levin-Modell, ist nur aufgrund seines periodischen Antriebs topologisch isolierend. Wir untersuchen, wie ein Potential auf der Diagonale den Weg der topologischen Randzustände beeinflusst.

Während die ersten beiden Systeme durch einen internen Antrieb periodisch getrieben werden, untersuchen wir in unserem dritten System den externen Antrieb eines Laserfelds. Zweidimensionale hexagonale Nanoribbons emittieren hohe Harmonische aufgrund ihrer Wechselwirkung mit dem Laser. Die Stärke und Polarisationsrichtung dieser Harmonischen hängen von der Randstruktur der Nanoribbons ab, sowie von einem alternierenden Potential auf den Gitterplätzen.

Table of contents

List of publications

[1] H. Drüeke and D. Bauer: "Robustness of topologically sensitive harmonic generation in laser-driven linear chains", *Physical Review A* 99.5 (2019), 053402, DOI: 10.1103/PhysRevA.99.053402

[2] H. Drüeke and D. Bauer: "High-harmonic spectra of hexagonal nanoribbons from real-space time-dependent Schrödinger calculations", *The European Physical Journal Special Topics* 230.23 (2021), 4065–4070, DOI: 10.1140/epjs/s11734-021-00188-9

[3] H. Drüeke, M. Meschede, and D. Bauer: "Steering edge currents through a Floquet topological insulator", *Physical Review Research* 5.2 (2023), 023056, DOI: 10.1103/PhysRevResearch.5.023056

[4] H. Drüeke and D. Bauer: "Interaction-induced directional transport on periodically driven chains", *Physical Review Research* 6.2 (2024), 023032, DOI: 10.1103/PhysRevResearch.6.023032

[5] J. Beck, M. Heinrich, M. Meschede, H. Drüeke, F. Piccioli, S. Weidemann, J. Feis, D. Bauer, and A. Szameit: "Drive-induced Non-local Interactions and Topological Bulk Transport of Extended Doublons", *submitted for publication* (2024)

Part I.

Context and summary

1. Introduction

To introduce the topic of this thesis, we will use the metaphor of a screw to explain its title, *Directional transport in interacting Floquet systems*.

Floquet systems are temporally periodic [6], i.e., they repeat in regular time intervals. Section 2.1 of this thesis describes the theoretical background of Floquet theory. The periodic drives of Floquet systems are either internal or external. In internally driven systems, intrinsic properties of the system change, for example potential strengths or lattice positions. Laser fields are an example of external drives. An applied example of a Floquet system would be a screw, where the external drive would be the turning of a screwdriver. After one full rotation, the screwdriver is again in its initial configuration.

Directional transport is one possible effect of a Floquet drive. The drive can move particles such as electrons or atoms so that, at the end of a driving cycle, they are no longer (and neither again) in their initial positions. A more abstract transport phenomenon would be the emission of light. The emitted photons constitute an energy transport. The photons' frequency may differ from that of the drive. Section 2.4 gives a theoretical description of this process, called high-order harmonic generation. In the metaphor, the rotation of the screwdriver results in the movement of a screw into a piece of wood. (Depending on the direction of rotation, the screw might also move out of the wood.) The periodic rotation leads to a linear motion in a direction perpendicular to the plane of rotation.

Interaction is necessary for some of the transport processes in Floquet systems. For a laser field to act as the external drive of a Floquet system, the light must interact with the particles to affect them. Chapter 5 describes our study on how hexagonal nanoribbons interact with a laser field. The light-matter interaction leads to the emission of high-order harmonics. The metaphorical screwdriver needs to engage the head of the screw. Otherwise, it cannot turn the screw.

Interaction can also change the direction of transport in a Floquet system. One class of materials in which this happens is called (Floquet-)topological insulators. Sections 2.2 and 2.3 explain their theoretical background. (Floquet-)topological insulators have an insulating bulk and a conducting edge. In the insulating bulk,

the particles return to their initial locations at the end of the Floquet driving cycle. The particles at the boundary move along the edge due to the periodic drive. In Chapter 4, we study how interaction steers the directional edge states in a two-dimensional Floquet-topological insulator.

In an internally driven Floquet system, the interaction between particles can also be a prerequisite for transport. We study this in a system comprising two interacting particles on one-dimensional chains, as described in Chapter 3. The particles perform a bound, directional motion due to the combination of their interaction and the internal Floquet drive. In the picture of the screwdriver, imagine that the screw does not go into a piece of wood but through (predrilled) holes in two sheets of metal, to bolt them together. On its own, the screw cannot achieve this task. It must be combined with a nut on the other side of the metal to hold it in place. A wrench needs to hold the nut in place while the screwdriver turns the screw. (Or the screwdriver holds the screw while the wrench turns the nut.) The interaction between screw and nut is necessary to achieve the desired effect.

Structure of this thesis This thesis is a cumulative one and consists of two parts. Part I gives the context for the research and summarizes the results, as described above. It also contains an outlook in Chapter 6, and a bibliography.

Part II contains the three publications that make up the central part of this thesis, in Chapters 7, 8, and 9. Since all papers are open-access publications, they are each reprinted in their entirety. The reprints contain their respective bibliographies.

2. Theory

2.1. Floquet theory

Although the Floquet theorem came before it, perhaps more widely known today is a similar approach, called Bloch ansatz [7]. Bloch's theorem applies to the solutions of the Schrödinger equation in a spatially periodic potential

$$V(\mathbf{r}) = V(\mathbf{r} + \mathbf{R}) \quad \forall\, \mathbf{r}\ , \tag{2.1}$$

with lattice vector $\mathbf{R}$. It states that these solutions can be written as the product of plane waves $\mathrm{e}^{\mathrm{i}\mathbf{k}\cdot\mathbf{r}}$ and periodic functions $u(\mathbf{r}) = u(\mathbf{r} + \mathbf{R})$,

$$\varphi(\mathbf{r}) = \mathrm{e}^{\mathrm{i}\mathbf{k}\cdot\mathbf{r}}\, u(\mathbf{r})\ . \tag{2.2}$$

The solutions themselves have the same lattice periodicity as the potential, except for a phase,

$$\varphi(\mathbf{r} + \mathbf{R}) = \mathrm{e}^{\mathrm{i}\mathbf{k}\cdot(\mathbf{r}+\mathbf{R})}\, u(\mathbf{r} + \mathbf{R}) = \mathrm{e}^{\mathrm{i}\mathbf{k}\cdot\mathbf{R}}\, \mathrm{e}^{\mathrm{i}\mathbf{k}\cdot\mathbf{r}}\, u(\mathbf{r}) = \mathrm{e}^{\mathrm{i}\mathbf{k}\cdot\mathbf{R}}\, \varphi(\mathbf{r})\ . \tag{2.3}$$

The resulting probability density is periodic as well,

$$p(\mathbf{r} + \mathbf{R}) = |\varphi(\mathbf{r} + \mathbf{R})|^2 = \left|\mathrm{e}^{\mathrm{i}\mathbf{k}\cdot\mathbf{R}}\, \varphi(\mathbf{r})\right|^2 = \left|\mathrm{e}^{\mathrm{i}\mathbf{k}\cdot\mathbf{R}}\right|^2 |\varphi(\mathbf{r})|^2 = |\varphi(\mathbf{r})|^2 = p(\mathbf{r})\ . \tag{2.4}$$

Bloch theory is used in calculations on crystalline solids, e.g., for electronic band structures.

Floquet theory [6] is equivalent to Bloch theory, except it treats temporal periodicity instead of spatial periodicity. Numerous applications of Floquet theory have been studied. An overview can be obtained from the recent reviews [8–11]. An introduction suitable for readers new to this field can be found in the pedagogical handbook by Rudner and Lindner [12].

The Floquet theorem applies to sets of linear differential equations with periodic coefficients. For instance, we use it to solve the time-dependent Schrödinger equation

$$\mathrm{i}\hbar\, \frac{\mathrm{d}}{\mathrm{d}t}\varphi(t) = \hat{H}(t)\, \varphi(t) \tag{2.5}$$

with a temporally periodic Hamiltonian

$$\hat{H}(t) = \hat{H}(t + T) \quad \forall\, t\ . \tag{2.6}$$

According to Floquet's theorem, the states

$$\varphi_n(t) = \exp\left(\frac{\varepsilon_n t}{\mathrm{i}\hbar}\right)\psi_n(t) \tag{2.7}$$

with temporally periodic states $\psi_n(t) = \psi_n(t+T)$ and quasienergies ε_n form a complete set of orthonormal solutions. Inserting Eq. 2.7 into Eq. 2.5 yields

$$\left(\varepsilon_n + \mathrm{i}\hbar\frac{\mathrm{d}}{\mathrm{d}t}\right)\psi_n(t) = \hat{H}(t)\psi_n(t)\ . \tag{2.8}$$

The Floquet states are an advantageous basis for describing the system dynamics. Any solution of the Schrödinger equation can be written as a superposition of the Floquet states,

$$\varphi(t) = \sum_n a_n\varphi_n(t)\ . \tag{2.9}$$

The following subsections will explain two approaches for solving the time-dependent Schrödinger equation (2.5) with a temporally periodic Hamiltonian: the direct solution for piecewise-constant systems and the method of Floquet blocks.

2.1.1. Piecewise-constant systems

The time evolution operator $\hat{U}(t,t_0)$ describes the system's temporal evolution from time t_0 to time t,

$$\varphi(t) = \hat{U}(t,t_0)\,\varphi(t_0)\ . \tag{2.10}$$

It is evident from this definition that

$$\hat{U}(t,t) = \hat{1}\ \ \forall t \tag{2.11}$$

and

$$\hat{U}(t_2,t_0) = \hat{U}(t_2,t_1)\,\hat{U}(t_1,t_0)\ \ \forall t_1,t_2\ . \tag{2.12}$$

Inserting Eq. 2.10 into Eq. 2.5 yields

$$\mathrm{i}\hbar\frac{\mathrm{d}}{\mathrm{d}t}\hat{U}(t,t_0)\,\varphi(t_0) = \hat{H}(t)\,\hat{U}(t,t_0)\,\varphi(t_0)\ . \tag{2.13}$$

This must be true for any initial state $\varphi(t_0)$ and we obtain an equation of motion for the time evolution operator [13],

$$\mathrm{i}\hbar\frac{\mathrm{d}}{\mathrm{d}t}\hat{U}(t,t_0) = \hat{H}(t)\,\hat{U}(t,t_0)\ . \tag{2.14}$$

For constant Hamiltonians, this is solved by

$$\hat{U}(t,t_0) = \exp\left(\frac{t-t_0}{\mathrm{i}\hbar}\hat{H}\right)\ . \tag{2.15}$$

For a temporally periodic Hamiltonian, we are interested in the stroboscopic (Floquet) time evolution operator, which is defined as $\hat{U}(T) = \hat{U}(T, 0)$. Solving the equation

$$\hat{U}(T)\,\psi_n(0) = \lambda_n\,\psi_n(0) \tag{2.16}$$

gives the Floquet eigenstates $\psi_n(0)$, and the Floquet energies ε_n are calculated from the eigenvalues $\lambda_\mathrm{F} = \exp\left(\varepsilon_\mathrm{F} T/(\mathrm{i}\hbar)\right)$. Choosing the correct branch cut for the complex logarithm in

$$\varepsilon_n = \frac{\mathrm{i}\hbar \ln(\lambda_n)}{T} \tag{2.17}$$

limits ε_n from $-\pi\hbar/T$ to $\pi\hbar/T$.

Generally, the Floquet operator $\hat{U}(T)$ which solves the equation of motion (2.14) is not easy to calculate. For piecewise-constant Hamiltonians, however, it is straightforward. For example, for a driving period consisting of four equal-time phases of duration $\tau = T/4$,

$$\hat{H}(t) = \begin{cases} \hat{H}_1 & 0 < t \leq \tau \\ \hat{H}_2 & \tau < t \leq 2\tau \\ \hat{H}_3 & 2\tau < t \leq 3\tau \\ \hat{H}_4 & 3\tau < t \leq 4\tau = T \end{cases}, \tag{2.18}$$

we split the Floquet operator into four parts according to (2.12) and use (2.15) for the resulting constant Hamiltonians to arrive at

$$\hat{U}(T) = \hat{U}(4\tau, 3\tau)\,\hat{U}(3\tau, 2\tau)\,\hat{U}(2\tau, \tau)\,\hat{U}(\tau, 0) \tag{2.19}$$

$$= \exp\left(\frac{\tau}{\mathrm{i}\hbar}\hat{H}_4\right) \exp\left(\frac{\tau}{\mathrm{i}\hbar}\hat{H}_3\right) \exp\left(\frac{\tau}{\mathrm{i}\hbar}\hat{H}_2\right) \exp\left(\frac{\tau}{\mathrm{i}\hbar}\hat{H}_1\right)\ , \tag{2.20}$$

a simple multiplication of matrix exponentials.

2.1.2. Floquet blocks

If $\hat{H}(t)$ is not piecewise-constant, calculating $\hat{U}(T)$ is more complicated. We could numerically approximate $\hat{H}(t)$ in many piecewise-constant time intervals. But we can also solve the time-dependent Schrödinger equation with a temporally periodic Hamiltonian (2.5) by another method, using Floquet blocks. (The following derivation parallels the one in [12].)

We start with a Fourier expansion. The periodic Hamiltonian $\hat{H}(t)$ and the states $\psi_n(t)$ can both be represented as Fourier series

$$\hat{H}(t) = \sum_m \exp(-\mathrm{i}m\omega t)\,\hat{H}^{(m)}, \tag{2.21}$$

$$\psi_n(t) = \sum_m \exp(-\mathrm{i}m\omega t)\,\psi_n^{(m)}, \tag{2.22}$$

where $\omega = \frac{2\pi}{T}$. They are entirely determined by the sets of their Fourier components $\hat{H}^{(m)}$ and $\psi_n^{(m)}$. The series index $m \in \mathbb{Z}$ may take any integer number.

Inserting the Fourier expansions into Eq. 2.8 results in

$$(\varepsilon_n + m\hbar\omega)\,\psi_n^{(m)} = \sum_{m'} \hat{H}^{(m-m')}\,\psi_n^{(m')}. \tag{2.23}$$

We interpret Eq. 2.23 as an eigenvalue equation in Fourier harmonic space,

$$\mathcal{H}\,\boldsymbol{\psi}_n = \varepsilon_n\,\boldsymbol{\psi}_n\ . \tag{2.24}$$

The vector $\boldsymbol{\psi}_n$ contains all Fourier components,

$$\boldsymbol{\psi}_n = \begin{pmatrix} \vdots \\ \psi_n^{(m-1)} \\ \psi_n^{(m)} \\ \psi_n^{(m+1)} \\ \vdots \end{pmatrix} \tag{2.25}$$

and the matrix $\mathcal{H}$ is

$$\mathcal{H} = \begin{pmatrix} \ddots & \ddots & \ddots & \ddots & \ddots \\ \ddots & H^{(0)} - (m-1)\hbar\omega & H^{(-1)} & H^{(-2)} & \ddots \\ \ddots & H^{(1)} & H^{(0)} - m\hbar\omega & H^{(-1)} & \ddots \\ \ddots & H^{(2)} & H^{(1)} & H^{(0)} - (m+1)\hbar\omega & \ddots \\ \ddots & \ddots & \ddots & \ddots & \ddots \end{pmatrix}, \tag{2.26}$$

with the time-averaged Hamiltonian $H^{(0)} = \frac{1}{T}\int_0^T dt\, H(t)$. $\mathcal{H}$ is a block matrix (partitioned matrix) composed of blocks (submatrices) of size $d \times d$, where d is the dimension of $\hat{H}(t)$. The infinite-dimensional matrix $\mathcal{H}$ describes the solutions to our finite-dimensional problem (Eq. 2.5). Therefore, the solutions to Eq. 2.24 must be linearly dependent. Indeed, the spectrum of $\mathcal{H}$ contains infinitely many shifted copies of the system's Floquet spectrum. The energy of each Floquet state can be shifted by multiples of $\hbar\omega$ while leaving the state unchanged (up to a phase shift). We only need to determine those Floquet states with Floquet energies ε in the Floquet-Brillouin zone, $-\hbar\omega/2 < \varepsilon \leq \hbar\omega/2$. The physical interpretation of the Floquet-Brillouin zone is that the energy of a periodically driven system is only conserved up to the absorption or emission of integer multiples of the driving frequency $\hbar\omega$.

2.2. Topological insulators

A topological insulator (TI) is a material whose bulk is electrically insulating while its surface is electrically conducting. In order to understand TIs, let us first recapitulate the quantum Hall effect.

2.2.1. Quantum Hall effect

Classical Hall effect

Edwin Hall discovered this eponymous effect in 1879 [14] in a sheet of gold leaf while working on his PhD. When a conductor is placed in a magnetic field, a current I flowing through it (perpendicularly to the magnetic field lines) is deflected in a direction perpendicular to both the magnetic field and the current. This deflection leads to a measurable voltage U_{H}, called Hall voltage. The Hall resistance is defined as

$$R_{\mathrm{H}} = \frac{U_{\mathrm{H}}}{I} \ . \tag{2.27}$$

It depends on the magnetic field strength and the material.

The magnetic field breaks the time-reversal symmetry. (For example, the Lorentz force [15] on a charged particle moving through a magnetic field changes its sign when the direction of motion (i.e. time) is reversed.) As we will see later, topological insulators break time-reversal symmetry by other mechanisms, resulting in similar effects without external magnetic fields.

Quantum Hall effect

In a magnetic field, the possible electron energies become quantized, convined to the so-called Landau levels [16]. Higher field strengths cause a wider spacing of the Landau levels. Therefore, fewer levels are filled. The number of filled Landau levels determines the Hall resistance, which becomes quantized itself [17]. At low temperatures, in two-dimensional electron systems, this effect is measurable and the Hall resistance is

$$R_{\mathrm{H}} = \frac{h}{\nu e^2} \tag{2.28}$$

with the elementary charge e and Planck constant h.

Integer quantum Hall effect

The divisor ν (in Equation 2.28) can take integer values; the effect is then called integer quantum Hall effect. Theoretically predicted (but not believed) in 1975 [18], it was experimentally demonstrated by Klaus von Klitzing in 1980 [19] in a silicon-based metal–oxide–semiconductor field-effect transistor (MOSFET). He received the Nobel Prize in Physics in 1985 [20] for his discovery. The von Klitzing constant $R_\mathrm{K} = \frac{h}{e^2}$ is named after him.

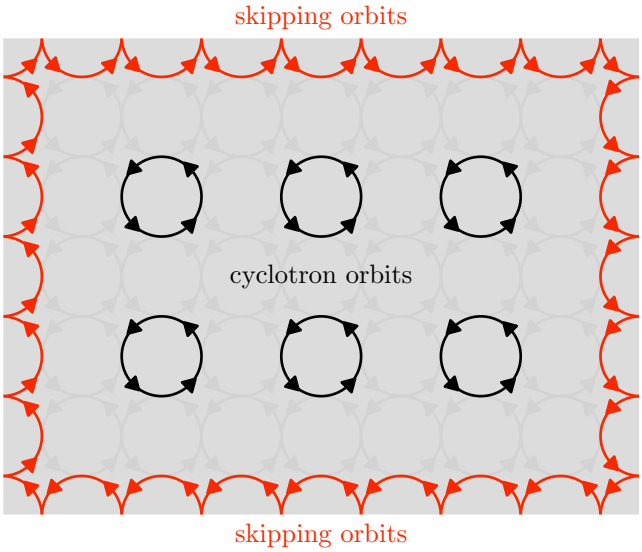

Figure 2.1.: Sketch of cyclotron orbits (in the bulk) and the resulting edge currents in a two-dimensional material exhibiting a quantum Hall effect. The magnetic field in perpendicular to the plane of the material.

The magnetic field induces a circular motion of the electrons (cyclotron orbits) in a two-dimensional material, as illustated in Figure 2.1. The electrons remain localized. They are not mobile, which makes the bulk of the material an insulator. Along the boundaries of the material, the electrons collide with the edge and cannot complete their orbits. Because they can only orbit in one direction, they repeat a series of half-orbits, leading to directional transport: an edge current.

Fractional quantum Hall effect

Although not necessary for the storyline of this thesis, the fractional quantum Hall effect is included for completeness: In the fractional quantum Hall effect, ν (in Equation 2.28) takes fractional values. It was experimentally discovered by Daniel Tsui, Horst Störmer, and Arthur Gossard in 1982 [21]. Robert Laughlin found its theoretical explanation (a many-electron wave function leading to fractionally

charged quasiparticles) in 1983 [22]. Laughlin, Störmer, and Tsui received the Nobel Prize in Physics in 1998 [23].

2.2.2. Haldane model

In a topological insulator, the time-reversal symmetry is not broken by an external magnetic field but instead by intrinsic properties of the material. Topological insulators are a broad field of research, and several textbooks exist on the topic [24–26].

In 1988, Duncan Haldane proposed a hexagonal model system in which complex hoppings break time-reversal symmetry [27]. He received the Nobel Prize in Physics in 2016 [28] for this work.

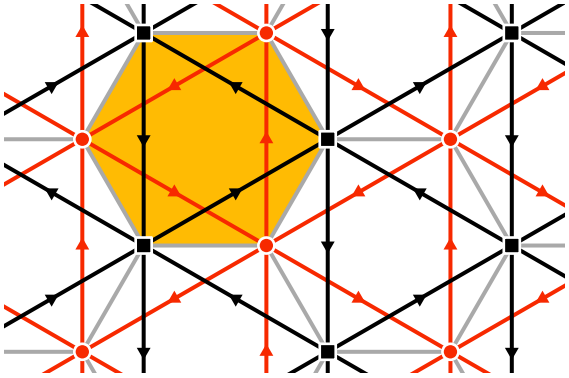

Figure 2.2.: Sketch of the Haldane model, showing the lattice sites and the hoppings between them. The unit cell (marked by an orange hexagon) comprises two lattice sites, A and B (marked by red circles and black squares). Gray lines mark the first-neighbor hoppings t_1. They are real-valued and, therefore, the same in both directions. Black and red lines with arrows indicate the direction of the complex-valued second-neighbor hoppings t_2.

The Haldane model is defined on a two-dimensional hexagonal lattice, as shown in Figure 2.2. It models a two-dimensional semimetal. The system's parameters can be adjusted to break inversion symmetry, which turns it into a normal semiconductor. If time-reversal symmetry is broken, however, the system exhibits an integer quantum Hall effect. If both symmetries are broken at the same time, the relative strength of the perturbations determines the resulting state [27].

The total flux through each lattice cell (also called a plaquette, marked by the orange hexagon in Fig. 2.2) is fixed to zero. Because the phase accumulated on a closed path must equal the enclosed flux, we can explicitly set the hoppings between lattice sites. The first-neighbor hoppings t_1 must be real-valued, and no phase is accumulated on

the hexagonal orbit around the plaquette because it encloses a complete unit cell and, therefore, zero flux. The second-neighbor hoppings t_2, on the other hand, are complex-valued. A complete cycle (following second-neighbor hoppings along a triangle marked by red or black arrows) does not enclose a complete unit cell and, therefore, possibly non-zero flux, accumulating a non-zero phase. With a non-real value t_2, the direction of the second-neighbor hoppings becomes significant. If a particle hops in the opposite direction, it accumulates an opposite phase. Therefore, the complex-valued second-neighbor hoppings break time-reversal symmetry, just as an external magnetic field would. The Haldane model has an insulating bulk and edge currents. It is a model of a two-dimensional topological insulator. Many other models exist, and we categorize them in the following subsection.

2.2.3. Categorization of topological insulators

Topological invariants

Non-zero topological invariants characterize topological materials. To illustrate the concept of a topological invariant, let us look back at a system with an integer quantum Hall effect (as described in Subsection 2.2.1). The integer ν in Equation 2.28 is the topological invariant of the system. It characterizes the quantized Hall resistance. If ν vanishes ($\nu \to 0$), the Hall resistance becomes infinite ($R_\mathrm{H} \to \infty$) and no edge current occurs. The system exhibits no integer quantum Hall effect and is not topological.

Many topological invariants exist, classifying systems of different dimensions and symmetries (particle number conservation and time reversal). Kitaev condensed the invariants for these different systems into a periodic table [29].

Higher-order topological insulators

Higher-order topological insulators differ from first-order topological insulators in the difference between the dimension of their edge states and the dimension of the whole system. In first-order topological insulators, the dimension of the topological edge state is $n - 1$, where n is the dimension of the material. Examples are zero-dimensional corners in one-dimensional materials, one-dimensional edges in two-dimensional materials, and two-dimensional surfaces in three-dimensional materials. In higher-order topological insulators, the dimension of the edge state is smaller than $n - 1$. Second-order topological edge states are, for example, zero-dimensional corners in two-dimensional materials and one-dimensional edges in three-dimensional materials. Zero-dimensional corners in three-dimensional materials are third-order topological edge states.

Topological materials

While topological effects were first described for electronic systems, the same concepts can be used to describe topological effects in a vast array of physical systems. In spin systems, they may be used for quantum computations [30]. Applied to mechanical waves [31–33], they can be used to construct metamaterials with tailored responses [34, 35]. We will explain topological effects in photonic systems [36–41] in more detail in the following section on Floquet-topological insulators.

2.3. Floquet-topological insulators

The time-reversal symmetry is also broken in so-called Floquet-topological insulators (FTIs). In contrast to Hall materials and topological insulators, this symmetry breaking is not caused by a magnetic field or imaginary hoppings but instead by time-dependent hoppings. The reviews [10, 42] provide an introduction and overview. FTIs can be used to create metamaterials [43]. Floquet engineering [44], i.e., the control of quantum systems using time-periodic external fields, is used to modify band structures [11] and in ultrafast spintronics [45–47].

Floquet-topological invariants

Floquet-topological insulators can be classified into a periodic table [48], extending the one for (non-Floquet) topological insulators [29]. Recently, invariants were systematically studied for higher-order Floquet-topological insulators [49].

2.3.1. Rudner–Lindner–Berg–Levin model

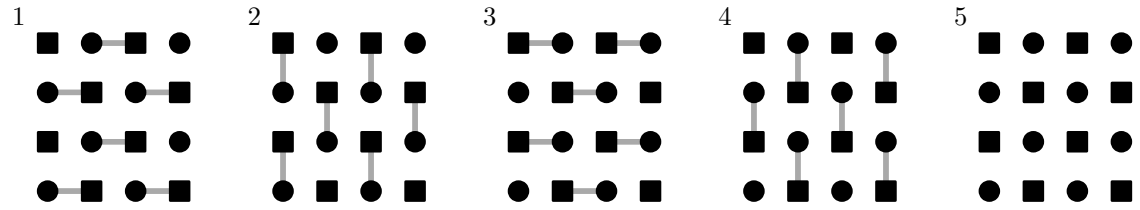

Figure 2.3.: Sketch of the five driving phases of the Rudner–Lindner–Berg–Levin model. The black circles and squares mark the sites of the two sublattices A and B. The gray lines indicate the hoppings J in the first four phases.

The Rudner–Lindner–Berg–Levin (RLBL) model [50] is an anomalous FTI on a square grid. As shown in Figure 2.3, the driving scheme of the RLBL model consists

of five phases. In each of the first four phases, a hopping term J couples each lattice site to one of its nearest neighbors. The hoppings define two sublattices, A and B, which form a checkerboard pattern. A sublattice potential δ_{AB} separates the on-site energies of the two sublattices. In the fifth phase, all hopping amplitudes are zero, and only the sublattice potential is active.

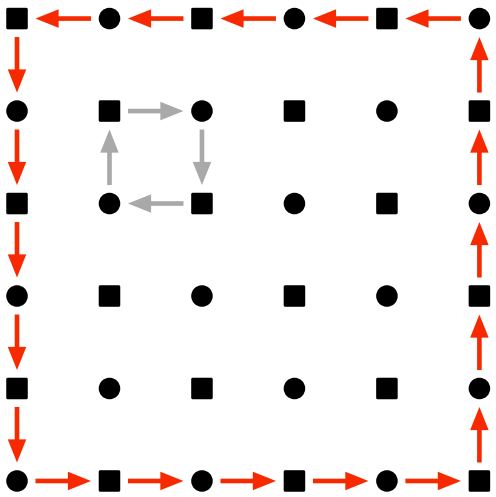

Figure 2.4.: Particle paths in the Rudner–Lindner–Berg–Levin model. The gray arrows show the path of a particle around a plaquette in the bulk of the system. The red arrows show the edge current.

The time $T/5$ (in relation to the hopping term J) of each phase is such that a particle transfers perfectly between neighboring sites in each step. Following a particle within the bulk of the system, it performs a discretized, clockwise "cyclotron orbit" around a plaquette (a smallest square in the lattice), as shown by the gray arrows in Figure 2.4. The particle returns to its origin at the end of the driving cycle. These closed orbits make the bulk isolating, in analogy to the quantum Hall effect (see Subsection 2.2.1). Also, as in the quantum Hall effect, the particles on the edge cannot complete the cyclotron orbits. This leads to an edge current in a counter-clockwise direction, as shown by the red arrows in Figure 2.4.

We investigated a modified version of the RLBL model in [3], which is part of this thesis (see Chapter 8).

2.3.2. Experimental realization

Experimental realization in optical lattices

Optical lattices are a viable experimental platform for implementing Floquet-topological insulators. In an optical lattice [51, 52], the arrangement of multiple laser beams forms a standing wave. Depending on the number of laser beams involved, the interference pattern can be a periodic structure in not just one but also in two or three dimensions. The Stark shift allows the trapping of neutral atoms. The light field is off-resonance from one of the electronic transitions of the atoms. It, therefore, induces a dipole moment in each atom. This dipole moment then interacts with the light, resulting in a force on the atom. Depending on the sign of the detuning (of the laser), the atoms accumulate on the intensity minima or maxima. The atoms must be at (ultra-)cold temperatures to suppress random motion away from their lattice sites.

The correspondence between a Floquet-topological insulator model and its realization in an optical lattice is easily apparent. The sites of the lattice in the topological model are the sites of the optical lattice. The particles are the cold atoms. The modulation of the lasers achieves a temporal change of the lattice.

A large variety of FTIs have been implemented in optical lattices (see review [53]). One-dimensional [54–56], two-dimensional [57–59], and second-order [60] FTIs have been studied, as well as systems with large topological numbers and multiple edge modes [61].

Experimental realization in photonic waveguides

Photonic waveguides can be written into transparent materials by femtosecond lasers [62, 63]. Focusing the laser pulse inside the material creates a high optical intensity in the focal volume. This intensity can lead to permanent structural changes, such as a modified refractive index. The focal point is steered (in all three dimensions) through the bulk of the material on a predetermined path. It thereby writes the desired refractive index pattern. The Schrödinger equation is replaced by the coupled-mode equations for light propagation in the waveguides, which model an analogous behavior. Light pulses are sent into individual waveguides, which act as the sites of the lattice. They propagate along the waveguide (this direction is usually called z), which corresponds to a temporal evolution. The distance between neighboring waveguides governs the transmission of light between them, corresponding to the hopping between lattice sites.

Rechtsman et al. achieved the first experimental implementation of an FTI in photonic waveguides in 2013 [64]. Since then, a wide variety of experiments were performed [36, 40]. For example, experiments on Anderson insulators [65], in which

disorder causes the topological behavior. Recently, progress has been made on the topic of non-Hermitian [66, 67] and non-linear [68] systems. Photonic FTIs are a possible avenue towards quantum computing [30, 69].

2.4. High-order harmonic generation

High-order harmonic generation (HHG) is an interaction process between matter (atoms, solids, clusters) and an external driving laser field. HHG is only one of several possible strong-field interactions between atoms and lasers [70]. Two other processes are above-threshold ionization [71, 72] and non-sequential multiple ionization [73, 74].

2.4.1. High-order harmonic generation in atoms

HHG can occur in the interaction of laser light with many different kinds of matter. We will first look at HHG in atoms because the process is easier to understand than in more complex systems (such as solids). Additionally, HHG was first observed experimentally in rare gases (in the late 1980s) [75, 76]. Since then, many different experimental setups have been used to investigate HHG and significantly improve the efficiency of the process [77–79].

Three-step model

The theoretical explanation for HHG in atoms was developed in the late 1980s and early 1990s [80–87]. In the following, we describe the three-step model proposed by Corkum in 1993 [87].

Step 1: Ionization In the first step, ionization occurs: the electron is removed from the atom. Depending on the strength of the laser, different ionization processes can take place. Figure 2.5 shows sketches of the three different ionization processes. The relevant property that distinguishes between them is the Keldysh parameter [88–90]

$$\gamma = \sqrt{\frac{I_\mathrm{p}}{2U_\mathrm{p}}} \,. \tag{2.29}$$

For weak fields ($\gamma > 1$), multiphoton ionization occurs as depicted in Figure 2.5 (a). The electron absorbs multiple photons until it has sufficient energy to escape the attractive potential of the atom. The laser does not significantly distort the

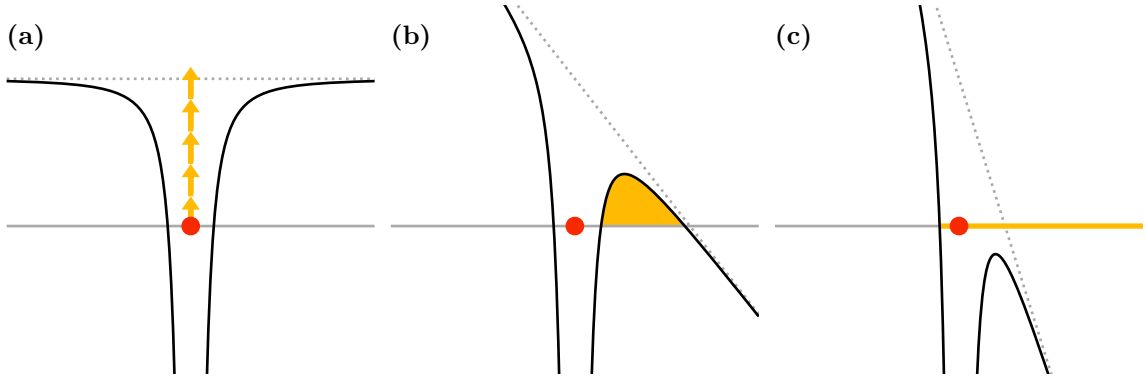

Figure 2.5.: Binding potentials for different ionization regimes. (a) Multiphoton ionization: the electron (red circle) absorbs multiple photons and escapes from the binding potential. (b) Tunneling: the electron tunnels through the tilted potential. (c) Barrier-suppression: the electron is free due to the strong distortion of the potential.

potential. This ionization regime is not typical for HHG, because HHG occurs for strong fields.

Stronger fields ($\gamma < 1$) significantly distort (tilt) the binding potential (Figure 2.5 (b)). The electron tunnels through the resulting barrier and out of the atom. In this tunneling regime, the ionization rate depends exponentially on the field strength [91].

For very strong fields, we enter the barrier-suppression regime [92, 93] (Figure 2.5 (c)). The laser suppresses the potential barrier below the energetic level of the electron, which can then freely move out from the atom without tunneling. The ionization rate is higher than in the tunneling regime, but lower than what the tunneling formulas predict when used for these strong fields (beyond their applicability) [94–99].

Step 2: Propagation After its emission from the ion, the laser's electric field accelerates the electron. Let us assume a cosine-field, $E(t) = E_0 \cos(\omega t)$. Due to the temporal periodicity of the laser field, it is helpful to write the time t as a phase θ, with $\theta = \omega t$. If the electron was emitted in a phase θ_e of the cycle where the electric field is increasing, $\left(n - \frac{1}{2}\right)\pi < \theta_e < n\pi$, $n \in \mathbb{Z}$, the electron flies away from the ion and never returns. The electron generates no harmonics.

For emission during decreasing field strength, $n\pi < \theta_e < \left(n + \frac{1}{2}\right)\pi$, the electron is first accelerated away from the ion by the electric field of the laser. Then, the electric field reverses, and the electron is accelerated back towards its parent ion. The electron arrives at the ion with non-zero kinetic energy. The energy depends on the time of emission. The maximum energy is $E_{\mathrm{kin,max}} = 3.17U_p$ [87, 100] and is achieved by electrons emitted at $\theta_e = 17°$, which return at $\theta_r = 255°$.

Step 3: Recombination The last step is recombination: the electron falls back into a bound state with the ion. It emits its surplus energy as a photon with photon energy equal to the sum of the ionization potential I_p (of the atom) and the kinetic energy E_kin of the electron. The maximum kinetic energy determines the maximum photon energy (called the cutoff of the harmonic plateau).

In high-harmonic spectra, the number of emitted photons is plotted as a function of their frequency Ω. The emitted frequency $\Omega = n\omega$ is usually denoted as multiples of the incoming laser frequency ω. We call n the harmonic order of the emission.

Brunel harmonic generation

After an electron has been removed from an atom by ionization, it cannot only generate harmonics by recombination, as described in the three-step model. So-called Brunel harmonics [83] are caused by the time-dependent population of free electrons.

Perturbative harmonic generation

Harmonics can even be generated without ionization. If an atom absorbs two or more photons from the external driving field, it can emit their combined energy as a single high-energy photon. The strength of these perturbative harmonics decreases rapidly with increasing harmonic order, because the probability of absorbing multiple photons decreases with the number of photons.

2.4.2. High-order harmonic generation in solids

Stepping up in complexity from single atoms, researchers observed harmonic emission from larger systems in the 2000s [101]. These atomic clusters and nanoparticles bridge the gap between atoms and solids. First observations of HHG in solids were made in bulk crystals [102]. Later, they were also observed in amorphous solids [103]. Since then, the field has grown tremendously. These recent reviews [104–107] provide an overview.

A complete theoretical understanding of HHG in solids is still subject to research. An overview may be gained from this tutorial [108] or this review [109]. An overview of numerical methods can be found in [110].

As necessary background knowledge for understanding our paper [2], we now have a look at the distinction between interband and intraband harmonics.

Interband harmonics

The generation of interband harmonics in solids unfolds analogously to the three-step model in atoms [111]. However, electronic bands replace both bound states and free space.

Step 1: Separation of charges An electron moves from a lower (valence) to a higher (conduction) band. This jump likely happens at a position in k-space where the bandgap is small. The electron is now in the conduction band and leaves behind a hole in the valence band.

Step 2: Evolution The electron and hole move in their respective bands according to the band curvatures and the external field. Both may gain energy from the field or lose energy to it. Therefore, the energy difference between bands might differ from the energy difference when the electron-hole pair formed.

Step 3: Recombination The electron and hole recombine and emit a photon with photon energy corresponding to their bandgap at this instance. Therefore, interband harmonics can only have frequencies larger than the minimum bandgap on the solid.

Intraband harmonics

In addition to the interband harmonics, solids can also emit intraband harmonics. As the name suggests, the electrons do not move from one band to another. Instead, the movement of electrons within a band causes the intraband harmonics. The external laser field moves the electrons in all occupied bands. In non-parabolic bands, the anharmonicity of the band curvature leads to higher-frequency components in the electron motion. This anharmonicity causes the emission of harmonics of the original laser frequency. In contrast to interband harmonics, intraband harmonics have no minimum energy and are usually strongest at low harmonic orders. Intraband dynamics also influence interband harmonics [112].

Intraband harmonics can only be emitted from partially filled bands. Completely filled bands do not emit intraband harmonics because the contributions from electrons at positive and negative band curvatures cancel each other out. This cancellation is complete because the integral over the Brillouin zone vanishes due to its periodicity.

Brunel harmonics

The time-dependent populations in the valence and conduction bands of the solid generate Brunel harmonics.

High-order harmonic generation in finite solids

In our publication [2], which is part of this thesis (see Chapter 5 and Chapter 9), we investigate HHG in a finite system, a hexagonal nanoribbon. Even though this relatively small system (of 24 or 26 atoms) is not spatially periodic and does, therefore, not have a proper band structure, the model of inter- and intraband harmonics is very suitable to describe our observations. Intraband harmonics occur up to an energy corresponding to the width of the valence band. The minimum and maximum bandgap between the valence band and the first conduction band limit the energies of the interband harmonics. The nanoribbons are a quasi-one-dimensional system, and we observe differences between harmonics emitted parallel and perpendicular to the ribbon. More detailed descriptions of these effects can be found in Chapter 5.

2.4.3. Selection rules

Selection rules govern the emission of high-order harmonics. The simplest one is the absence of even-order harmonics in inversion-symmetric systems (such as atoms) due to the destructive interference between successive half-cycles of the linearly polarized laser [113]. Different symmetries lead to different selection rules [114]. Many of their theoretical derivations use Floquet theory [115].

This concludes the theory chapter. The following three chapters summarize the findings of the three publications that constitute this cumulative thesis.

3. Interaction-induced directional transport

This chapter summarizes an article we published in *Physical Review Research* in 2024 [4].

3.1. Interacting particles on coupled chains

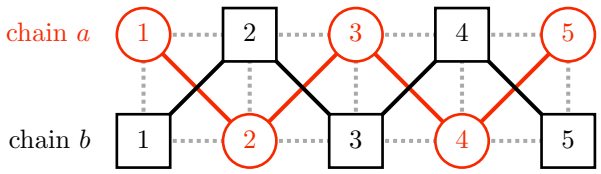

Figure 3.1.: Two one-dimensional chains a (red) and b (black) of identical length $N = 5$. The red and black lines indicate the hopping J of particles a and b between lattice sites (red circles and black squares) on their respective chains. Dashed gray lines indicate the interaction V between nearest-neighbor sites on different chains.

The system consists of two 1D chains, a (lattice sites indicated by red circles) and b (black squares), as shown in Figure 3.1. Two particles (also called a and b), one on each chain, hop between sites. The particles remain on their respective chains; they cannot move onto the other chain. The hopping element J connects all neighbors along the chains. A Floquet drive with period T governs the temporal evolution of the system. The two particles move alternatingly, particle a during the first half of the driving period, particle b during the second half,

$$J_a(t) = \begin{cases} J & 0 \leq t < T/2 \\ 0 & T/2 \leq t < T \end{cases} \tag{3.1a}$$

$$J_b(t) = \begin{cases} 0 & 0 \leq t < T/2 \\ J & T/2 \leq t < T. \end{cases} \tag{3.1b}$$

In addition to the intra-chain hopping, there is an inter-chain interaction V. It acts between nearest neighbors, as indicated by the gray dashed lines in Figure 3.1. Site i on chain a interacts with site j on chain b if $j = i - 1, i, i + 1$.

The length N of the chains could be infinite or finite. For most of our calculations, we choose a finite length long enough so particles cannot reach the edge during the observed time.

3.2. Interaction-dependent behavior

Without interaction ($V = 0$), each particle diffuses symmetrically to the left and right along its chain.

A very strong interaction leads to an energetic separation between configurations with interaction energy (when particles are neighbors) and configurations without interaction energy (when particles are not neighbors). Strong interaction $|V|$ prohibits two particles that are not neighbors from becoming neighbors and two particles that are neighbors from separating. Interestingly, the sign of V (whether the interaction is attractive or repulsive) is irrelevant. The system behaves identically for V and $-V$.

Two different kinds of particle configurations arise at $|V| \to \infty$: If the particles start apart (not as neighbors), they can never get close to each other. Both particles diffuse along their chain, away from each other. If the two particles start as neighbors, they form a bound pair, a quasiparticle called a doublon. They remain together and do not spread.

We will now rigorously investigate the doublon behavior. During the first phase (first half of the driving cycle), particle a moves while particle b is stationary on site j. The two particles form a doublon if particle a starts in one of the three sites $i = j - 1, j, j + 1$, next to particle b on site j. Due to the interaction, particle a cannot move to any lattice site except those three. Its movement is governed by the 3 Hamiltonian

$$H = \begin{pmatrix} V & J & 0 \\ J & V & J \\ 0 & J & V \end{pmatrix} \tag{3.2}$$

with the eigenenergies

$$E_0 = V, \quad E_{1,2} = V \pm \sqrt{2}J \tag{3.3}$$

and eigenstates

$$\varphi_0 = \begin{pmatrix} 1 \\ 0 \\ -1 \end{pmatrix}, \quad \varphi_{1,2} = \begin{pmatrix} 1 \\ \pm\sqrt{2} \\ 1 \end{pmatrix}. \tag{3.4}$$

We can now write any time-dependent state as

$$\psi_a(t) = \sum_{h=0}^{2} c_h \exp(-\mathrm{i}E_h t)\, \varphi_h. \tag{3.5}$$

Stationary doublon If particle a starts at $i = j$, with the right timing, the doublon (bound pair of particles a and b) remains stationary. The initial state of the particle is $\psi_a(0) = (0, 1, 0)^\mathsf{T}$, and the time-dependent probability becomes

$$p_a(t) = |\psi_a(t)|^2 = \frac{1}{2} \begin{pmatrix} \sin^2\left(\sqrt{2}Jt\right) \\ 2\cos^2\left(\sqrt{2}Jt\right) \\ \sin^2\left(\sqrt{2}Jt\right) \end{pmatrix} . \tag{3.6}$$

The particle moves symmetrically from the starting site j to the left and right neighbors $j \pm 1$ and then completely returns to site j at $t = \pi/\left(\sqrt{2}J\right)$. We choose $T = \sqrt{2}\pi/J$, and particle a returns to its initial site within its phase, $p_a(T/2) = (0, 1, 0)^\mathsf{T}$. Particle b behaves analogously during its phase, and the doublon remains stationary.

Leapfrogging doublon Moving doublons occur for $i = j \pm 1$. Without loss of generality, we initialize particle a at $i = j - 1$, $\psi_a(0) = (1, 0, 0)^\mathsf{T}$. The probability becomes

$$p_a(t) = \begin{pmatrix} \cos^4\left(Jt/\sqrt{2}\right) \\ \frac{1}{2}\sin^2\left(\sqrt{2}Jt\right) \\ \sin^4\left(Jt/\sqrt{2}\right) \end{pmatrix} . \tag{3.7}$$

Choosing the same $T = \sqrt{2}\pi/J$, we obtain $p_a(T/2) = (0, 0, 1)^\mathsf{T}$. Particle a leapfrogs over particle b from its left neighbor ($i = j - 1$) to its right neighbor ($i = j = 1$). During its phase, particle b leapfrogs over particle a, leading to directional transport. Effectively, both particles move two sites to the right without spreading. Figure 3.2 shows a sketch of the particles' movement. If the starting configuration is $i = j + 1$ (instead of $i = j - 1$), the particles move two sites to the left (instead of the right).

3.3. Mapping to two dimensions

We map our system from two one-dimensional chains to a two-dimensional grid by taking the coordinates of the two particles as x- and y-coordinates of a single particle in two dimensions. This mapping allows us to calculate a bandstructure, as we also do in the modified Rudner-Lindner-Berg-Levin model (Chapter 4, Chapter 8, [3]). We also calculated band energies in hexagonal nanoribbons (Chapter 5, Chapter 9, [2]).

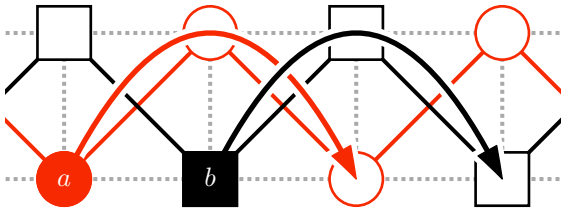

Figure 3.2.: Sketch of the leapfrogging movement of particles a and b during a complete driving cycle. During the first phase ($0 \leq t < T/2$), particle a jumps over particle b and two sites to the right. Then, during the second phase ($T/2 \leq t < T$), particle b jumps over particle a and two sites to the right.

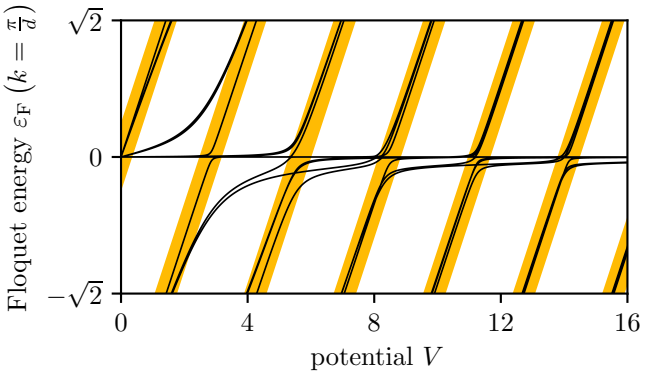

Figure 3.3.: Floquet energies ε_F at $k = \frac{\pi}{d}$ as a function of potential V for a 20-site wide strip. The orange shadow at $\varepsilon_F = V$ marks the energies of the doublons.

Figure 3.3 shows the Floquet energies $\varepsilon_F\left(k = \frac{\pi}{d}\right)$ as a function of potential V. The Floquet energies are periodic with period $2\sqrt{2}$. Looking at these energies, we can clearly distinguish between the different types of states.

The bulk states are at constant $\varepsilon_F\left(k = \frac{\pi}{d}\right) = 0$. They are configurations with the two particles far apart, not interacting. Therefore, their energy is independent of V.

The energies of the doublons increase linearly with V, as indicated by the orange shadow around $\varepsilon_F = V$. The two particles are interacting; therefore, the state's energy equals the interaction energy V.

The energies of the two edge states have a tilted pole at $V \approx 3$, where they approach the doublon energies. At higher potentials, they approach the energy of the bulk states, $\lim_{V\to\infty} \varepsilon_F\left(k = \frac{\pi}{d}\right) = 0$. In these states, the two particles are two sites apart ($i = j \pm 2$). They are not interacting, but the interaction blocks them from moving closer together.

3.4. Significance

Our work introduces a minimal model of a two-particle system demonstrating directional transport. The transport only arises due to interaction, which itself is not directional.

Many other systems have a predetermined direction of movement. Examples include (semi)classical [116, 117] and quantum ratchets [118–120], and Thouless pumping [121, 122]. These systems employ periodic driving in conjunction with asymmetric potentials.

4. Steering edge currents through a Floquet topological insulator

This chapter summarizes an article we published in *Physical Review Research* in 2023 [3].

4.1. Modified Rudner-Lindner-Berg-Levin model

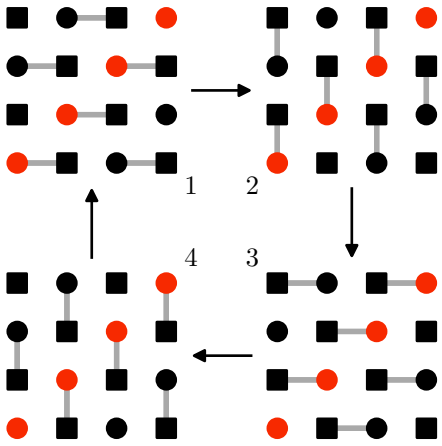

Figure 4.1.: Sketch of the four driving phases of the modified Rudner–Lindner–Berg–Levin model. The red circles mark the diagonal sites, which have a different potential than the other sites.

This work extends the Rudner-Lindner-Berg-Levin model [50] (see Subsection 2.3.1). We use the same periodic driving on a square lattice but without the fifth phase (the one in which all hopping amplitudes were equal to zero). Additionally, we replace the alternating (sublattice) potential with a diagonal potential, as shown by the red circles in Figure 4.1. This diagonal potential is inspired by mapping two interacting particles in one dimension onto a single particle in two dimensions. The x-position of our 2D particle corresponds to the position of the first 1D particle, while its y-position corresponds to the position of the second 1D particle. If the particles interact locally (only when they are at identical positions), this results in a diagonal

potential in 2D. A longer-range 1D interaction would affect the secondary, tertiary, etc. diagonal. The mapping makes the 1D particles distinguishable.

In the standard RLBL model, the drive results in an insulating two-dimensional bulk. A particle in the bulk takes four steps to circle around a plaquette (a smallest square in the lattice), one in each phase of the driving cycle. It returns to its origin at the end of the driving cycle. At the edge, a particle can only take two steps in each cycle because its site has no connection to another site in the other two phases, and the particle cannot move. This leads to edge currents running around the whole border of the system (see Figure 4.2 (a)). The helicity of these long edge paths is opposite to that of the small orbits in the bulk.

4.2. Influence of the diagonal potential

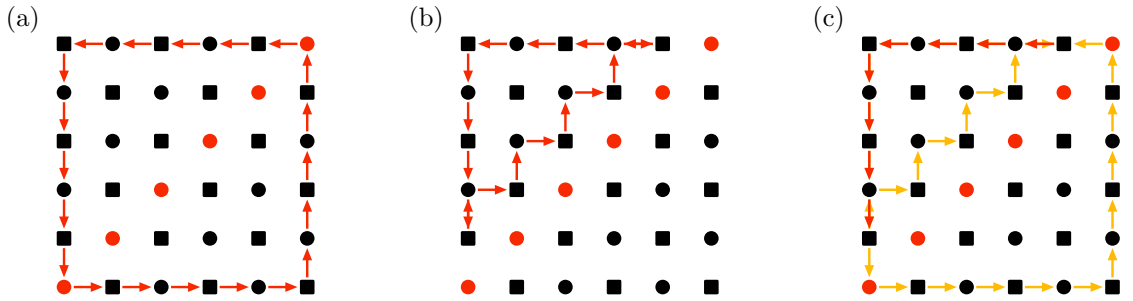

Figure 4.2.: Edge currents in the modified Rudner–Lindner–Berg–Levin model with diagonal potential. (a) Edge current around the whole square system, as it occurs for a vanishing diagonal potential, $V_{\mathrm{dia}} = 0$. (b) Edge current around the upper triangular half of the system, as it occurs for an infinite diagonal potential, $|V_{\mathrm{dia}}| \to \infty$. (c) Split edge current, as it occurs for most finite diagonal potentials.

What new effects does our diagonal potential V_{dia} bring to this system? The limiting cases are straightforward: When we have no diagonal potential, $V_{\mathrm{dia}} = 0$, we reproduce the results of Rudner et al. [50]. The edge current propagates along the outer edge of the system, as shown in Figure 4.2 (a). A very large potential, $|V_{\mathrm{dia}}| \to \infty$, effectively cuts the system in half. Particles cannot overcome the energetic separation between diagonal and off-diagonal sites. The edge currents run around each (triangular-shaped) half of the system. The edge current along the upper traingle is shown in Figure 4.2 (b). A particle initialized on the diagonal cannot move.

Interesting behavior arises for finite potential V_{dia}. A finite potential can split the edge current as shown in Figure 4.2 (c). One might expect that,for increasing V_{dia},

the system merely continuously transitions from one limiting case to the other. However, that is not the case due to resonances between the hopping amplitude (between connected sites) and the timing of the phases.

We define the hopping probability between two connected sites as the probability of finding a particle on one site at some time t after it had started perfectly localized on the other site. The hopping amplitude between the sites is J, and their potential difference is V. The hopping probability is

$$p(t, V) = \frac{4J^2}{V^2 + 4J^2} \sin^2\left(\frac{\sqrt{V^2 + 4J^2}}{2} t\right) . \tag{4.1}$$

The derivation of this equation can be found in Appendix A of our publication [3].

We choose the period $T = 2\pi/J$ such that perfect transfer happens between connected sites at identical potential,

$$p\left(\frac{T}{4}, 0\right) = p\left(\frac{\pi}{2J}, 0\right) = \sin^2\left(\pm\frac{\pi}{2}\right) = 1 . \tag{4.2}$$

With this period $T = 2\pi/J$ and setting $J = 1$, let us look at the transfer between connected diagonal and off-diagonal sites during a phase of the driving cycle. The hopping probability $p(V_{\text{dia}}) = p(T/4, V_{\text{dia}})$ at the end of the phase ($t = T/4$) is

$$p(V_{\text{dia}}) = \frac{4}{V_{\text{dia}}^2 + 4} \sin^2\left(\frac{\pi}{4}\sqrt{V_{\text{dia}}^2 + 4}\right) , \tag{4.3}$$

shown in Figure 4.3.

At the resonances

$$V_{\text{dia},0}^{(n)} = \pm 2\sqrt{4n^2 - 1} , \tag{4.4}$$

with $n \in \mathbb{N}$, the hopping probability vanishes, $p(V_{\text{dia},0}) = 0$. These finite potentials (marked by dashed gray lines in Figure 4.3) can cut the system in half and cause edge states around the two halves, just like an infinite potential V_{dia} would. How might we interpret this? The hopping between two sites is effectively a two-level system. Their potential difference determines the period of the resulting Rabi oscillation [123]. At discrete finite potentials, an integer multiple of the Rabi period equals the duration $T/4$ of the hopping phases. The particle moves from its origin to the neighbor and back one or several times. This effectively prohibits transfer between sites of different potential and cuts the system in half, even though the potential is not very strong.

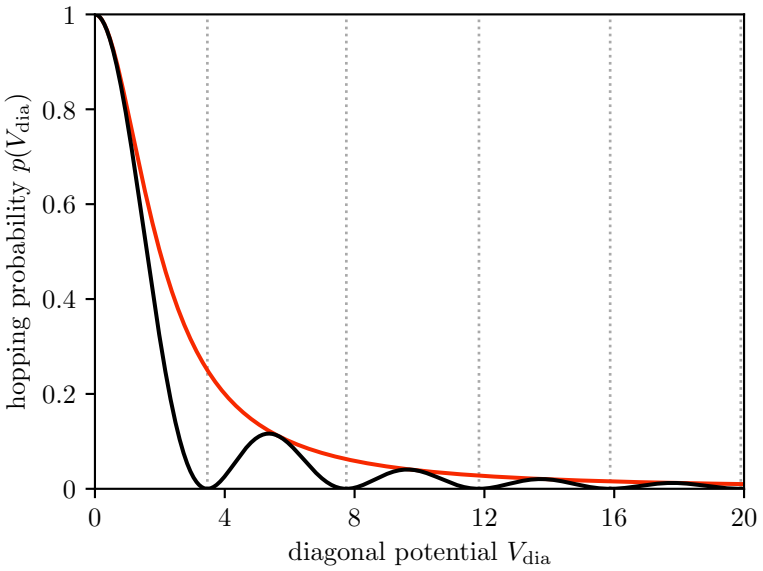

Figure 4.3.: Hopping probability $p(V_{\mathrm{dia}})$ as a function of diagonal potential V_{dia}. The continuously decreasing prefactor is shown in red. It dampens the periodic oscillations. This results in the full hopping probability, shown in black. Dashed gray lines mark the zeros $V_{\mathrm{dia},0}^{(n)}$ of the hopping probability.

4.3. Mapping back to one dimension

The diagonal potential was inspired by the mapping of two interacting, one-dimensional particles onto a single, two-dimensional particle. As described above, we interpret the two coordinates of our 2D particle as the coordinates of two 1D particles. The horizontal position of our 2D particle represents the position of the first 1D particle a. Its vertical position represents the position of the second 1D particle b. However, taking our whole system back from two dimensions to one dimension is more challenging. In the hopping scheme, hoppings are either vertical or horizontal, meaning that only one of the one-dimensional particles moves at a time. Whatever drive enables the hopping would need to distinguish between the two particles.

The possible hoppings for each particle during its phase depend on the position of the other particle. If the interaction strength is such that the 1D particles cannot be on the same site of the linear chain, the 2D particle cannot be on the system's diagonal. The triangular movement in 2D, which occurs at $|V| \to \infty$ and at $V_{\mathrm{dia},0}^{(n)} = \pm 2\sqrt{4n^2 - 1}$ corresponds to a complicated coupled movement of the 1D particles. Let us follow an edge state around the upper left triangle of the 2D system. The 1D particle a always stays left of particle b. They can never be on the same site and never jump over each other. The edge motion consists of three types of motion, each shown in a column of Figure 4.4.

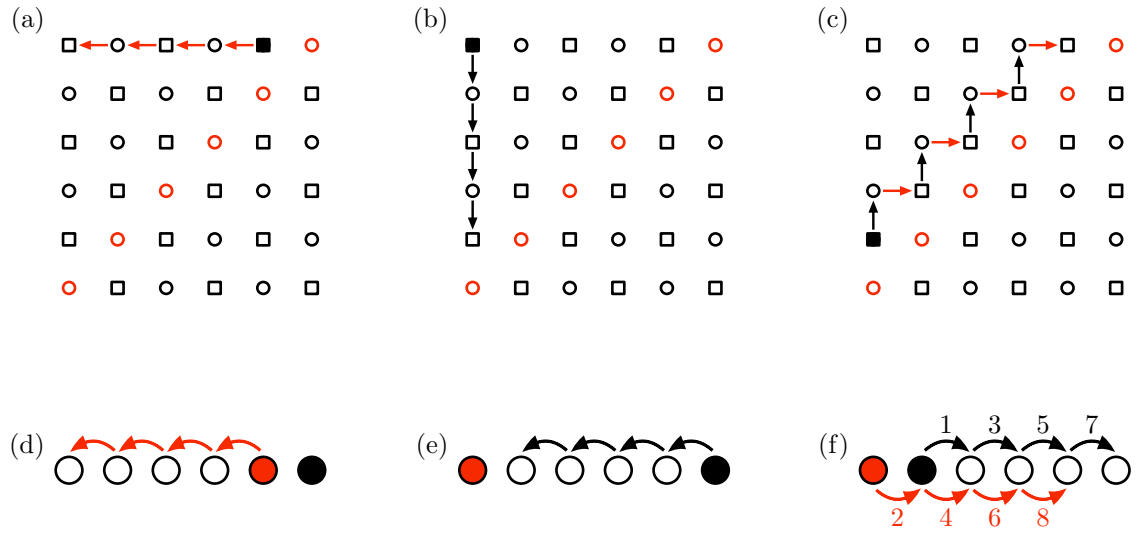

Figure 4.4.: Correspondence between the 2D edge state on a square grid and the 1D doublon on a linear chain. The empty circles and squares represent the lattice sites. The horizontal position of the 2D particle (marked by a black filled square) in the top row represents the position of the first 1D particle a (red filled circle in the bottom row). Its vertical position represents the position of the second 1D particle b (black filled circle). (a) The 2D edge state moves along the system's upper edge from right to left. (b) The edge state moves along the left edge from top to bottom. (c) The edge state moves along the diagonal from bottom left to top right. (d) The 1D particle a moves from right to left. Particle b remains stationary at the right end of the chain. (e) Particle b moves from right to left. Particle a remains stationary at the left end of the chain. (f) The particles move alternatingly to the right, particle a always trailing particle b.

The 2D particle starts one site to the left of the top right corner and moves to the left along the system's top edge (see Figure 4.4 (a)). In the 1D picture, this corresponds to the two 1D particles starting on the right side of the chain. Particle b starts on the rightmost site, and particle a starts on the second site from the right (Figure 4.4 (d)). They form a local doublon. Particle a moves to the left. Each step of particle a switches the connections of the rightmost site, where particle b is. However, because the phases of the driving scheme also switch (there are four phases, not just two), particle b's site is never connected to any other site. Particle b could only move further to the right, but no neighbor exists beyond the rightmost site. The movement of the two particles is determined by each other's position. They form an increasingly extended doublon.

When particle a reaches the leftmost lattice site, particle b follows (Figure 4.4 (e)).

Its motion keeps particle a locked at the leftmost site like particle a had previously kept particle b locked at the rightmost site. The distance between the particles making up the extended doublon decreases again. When particle b reaches particle a, the extended doublon becomes a local doublon. In the 2D picture, this corresponds to a motion along the system's left edge (Figure 4.4 (b)).

The edge state then moves along the 2D diagonal (Figure 4.4 (c)). Particle a is on the leftmost site, and particle b is on the second site from the left (Figure 4.4 (f)). Particle a cannot go anywhere because its site has no neighbor to the left and the neighboring site on the right is occupied by particle b. Therefore, particle a stays on the leftmost site. Particle b goes to the right. Then particle a follows it and also goes to the right. Particle a always lags behind particle b. In this bound motion of the local doublon, the distance between particles a and b alternates between one and two lattice constants. The two particles hobble along until they reach the right edge, and particle b cannot go forward anymore.

Then, the cycle repeats; particle a moves to the left, leaving particle b behind.

This behavior of the doublon (bound pair) is remarkable: during the cycle, the local doublon turns into an extended doublon and back to a local doublon. The periodic drive enables this extended doublon, even though the interaction between particles a and b is local.

4.4. Significance and experimental results

Experiments Beck et al. implemented this model system in photonic waveguides [124]. The temporal evolution of the model corresponds to the propagation of light along the waveguides. A different refractive index on the diagonal sites, compared to the other sites, implements the diagonal potential.

The experiments confirm the predicted behavior for various strengths of diagonal potential. A joint publication [5], combining (an extension of) our theory with their experimental results, is currently under review.

Significance The experiments confirm that it is possible to steer topologically protected light currents along the edge or through the bulk of the waveguide array, depending on the diagonal potential (refractive index). This steering could have applications for photonic computing.

The effect becomes even more interesting when we consider nonlinear phenomena. Intense laser light can modify the refractive index, allowing it to switch the topologically protected currents. This would enable a programmable photonic platform.

5. High-harmonic emission from hexagonal nanoribbons

This chapter summarizes an article we published in *The European Physical Journal Special Topics* special issue on *Intense Laser Matter Interaction in Atoms, Finite Systems and Condensed Media* in 2021 [2], with additional program code and data in a public repository at the *Open Science Framework* [125].

5.1. Hexagonal nanoribbons

The harmonic emission of one-dimensional [1, 126–129] and two-dimensional [130–134] systems are an active field of research. We investigate the emission of high-order harmonics from hexagonal nanoribbons using time-dependent Schrödinger calculations. The nanoribbons are a single hexagon wide and can occur in two different configurations, armchair and zig-zag, as shown in Figure 5.1. The names of the ribbons refer to the shapes of their long edges.

As the other systems investigated in this thesis, this is also a temporally periodically driven system. The external drive is a laser field. In contrast to atomic systems, our nanoribbons are not isotropic. Therefore, the direction of the laser relative to the system becomes significant. In our quasi-1D linear chains, an electric field oriented along the longest dimension of the system leads to the strongest interaction between laser and matter. For this reason, we investigate a laser that is polarized along the ribbons, as shown in Figure 5.1.

One famous material with a hexagonal structure is graphene. In graphene, all atoms are identical carbon atoms. We model this by identical potentials at all lattice sites. When introducing an alternating on-site potential, we increase the potential depth at some sites and decrease it at others. Two different kinds of lattice sites correspond to two different kinds of atoms. In hexagonal boron nitride, for example, the two kinds of atoms are boron and nitrogen.

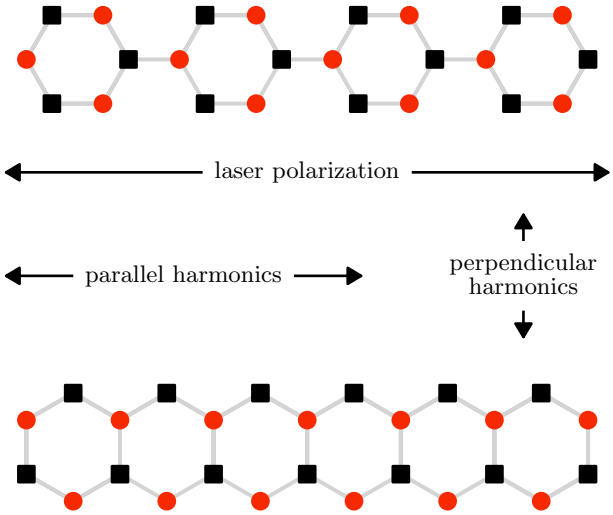

Figure 5.1.: Armchair (top) and zig-zag ribbon (bottom): At the black (square) lattice sites, the potential depth is increased by the on-site potential, $V_{\text{black}} = V_{\text{avg}} + V_{\text{os}}$. The red (circle) sites correspond to the shallower potentials of depth $V_{\text{red}} = V_{\text{avg}} - V_{\text{os}}$. The arrows indicate the polarization directions of the external laser field (along the ribbons) and the directions of the harmonics, which we refer to as parallel and perpendicular.

5.2. Harmonic generation

The general process for generating high-order harmonics is described in Subsection 2.4.2. To calculate them for our hexagonal nanoribbons, we first calculate their electronic eigenstates by imaginary-time propagation of the time-dependent Schrödinger equation. Next, we perform real-time simulations of the interaction of all occupied electronic orbitals with a short 4-cycle $\sin^2$-shaped laser pulse. We record the electronic dipoles and add them up. Fainally, the harmonic spectra are calculated as the absolute square of the Fourier transform of the recorded total dipoles, multiplied by a symmetric Hann window [135, 136].

Harmonics are generated by transitions between bands and by movements within bands. Intraband harmonics occur at energies below the bandwidth of the valence band. Interband harmonics occur at energies above the bandgap between the valence and conduction band. Without an alternating on-site potential, the bandgap is smaller than the bandwidth. This leads to an overlap between intra- and interband harmonics and an increased harmonic yield, as seen in Figure 5.2 (black line, $V_{\text{os}} = 0$). With a sufficiently large on-site potential, the bandgap becomes larger than the bandwidth. A gap arises between the highest intraband and the lowest interband harmonics (red line in Figure 5.2, $V_{\text{os}} = 0.5$). In this gap region (where neither

intra- nor interband harmonics occur), the harmonic emission is several orders of magnitude weaker.

Strictly speaking, band structures only exist for periodic systems. The periodicity is necessary to convert from the position vector $\mathbf{r}$ to the wave vector $\mathbf{k}$. The nanoribbons we investigate are not periodic and too small to approximate them as such. Therefore, we cannot calculate proper band structures. We can, however, calculate the eigenstates and eigenenergies of the system. These eigenenergies correspond to the band energies and the above interpretation of the harmonic generation is valid.

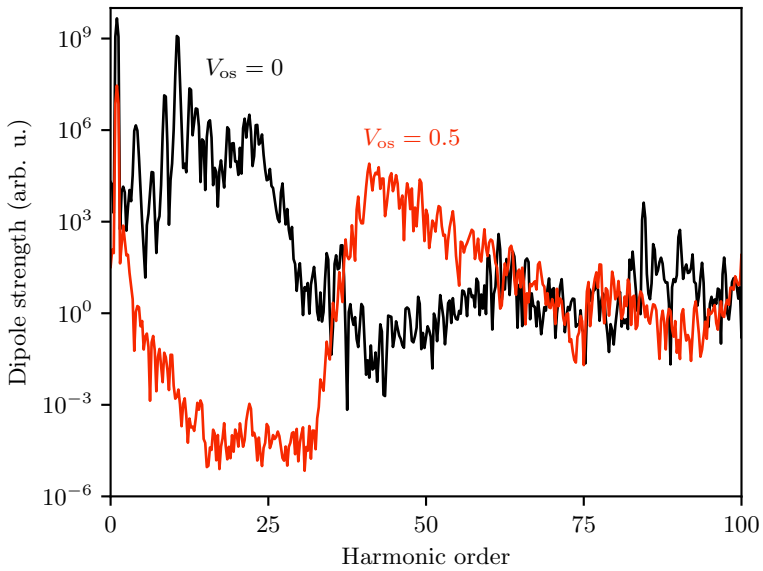

Figure 5.2.: High-order harmonic spectra from armchair nanoribbons with (red line, $V_{os} = 0.5$) and without (black line, $V_{os} = 0$) alternating on-site potential.

Another interesting feature of the emitted harmonics is their polarization. The zig-zag ribbon emits harmonics parallel to the laser polarization and, for non-zero on-site potentials, also perpendicular to it. The laser accelerates electrons along its polarization direction, which then emit parallel harmonics. A non-zero on-site potential introduces asymmetry in the perpendicular direction. Electron movement is deflected and no longer parallel to the laser polarization. The perpendicular motion component causes perpendicular harmonics. The armchair ribbon only emits harmonics parallel to the incoming laser. This is because it is symmetric in the perpendicular direction, and the electron movement is always parallel to the laser polarization.

5.3. Significance

In this publication, we used time-dependent Schrödinger calculations [137]. A parallel paper by Jürß and Bauer [138] uses a tight-binding approach to investigate the same system. The results of both approaches are consistent with each other. Our work validates the computationally much faster and simpler tight-binding approach. It can confidently be used for further investigations, for example, of larger and more complex systems for which time-dependent Schrödinger calculations are numerically unattainable.

6. Outlook

We investigated three systems in this thesis and answered many open research questions. However, every answer leads to new questions, and our results lay the foundation for additional research in many directions. This chapter provides an overview of different possible extensions of our research.

Longer-range interactions One could investigate the coupled chains and the modified Rudner-Lindner-Berg-Levin model for longer-range interactions. Then, the interaction would influence not only two particles on identical or neighboring sites but also states where they are further apart. The result could be several propagation channels, in which the particles' propagation speed depends on the distance between them. Of course, the interaction could have many different spatial shapes. It could, for example, fall off as 1/distance or 1/distance^2, or it could be constant up to a threshold distance and then go to zero. For many experimental settings, this would be more realistic than a short-range discrete interaction.

Time-dependent interactions The systems in this study are periodically time-dependent, but the interactions are all constant and static. Time-dependent interactions (both periodic or not) offer an avenue for very tailored behavior. One possible experimental realization is in cold atomic gases, where the interaction strength is tunable via magnetic Feshbach resonances [139–142]. Periodic modulations of interaction strengths have caused striking experimental results, including Faraday waves [143, 144] and Bose fireworks [145–147].

High-order harmonic generation in larger systems Many research groups also investigate high-order harmonic generation in larger or more complex systems. The nanoribbons we investigated are one hexagon wide and a few hexagons long. More extensive systems were not computationally feasible in the Schrödinger calculations. However, because our calculations verified the results of the much simpler tight-binding approach, it can be used for future calculations. Staying in two dimensions, one can investigate wider ribbons or whole sheets of hexagonal materials. Stacking these sheets into a multilayer system bridges the gaps to full three-dimensional materials.

Higher dimensions Not only the harmonic generation but also the two coupled chains could be studied in higher dimensions, and the two coupled chains could be extended to a two- or three-dimensional grid. Our quasi-one-dimensional system confined the movement of the doublon to a single dimension. Additional dimensions of the lattice would correspond to additional dimensions for the doublon's movement, leading to additional interesting phenomena. For example, impurities in the grid could deflect the doublon motion.

One could also imagine three-dimensional systems similar to the modified Rudner-Lindner-Berg-Levin model. The three dimensions can be considered as a single particle in three spatial dimensions or three particles in one spatial dimension.

Combination of internal and external drives Two systems in this thesis are Floquet due to an internal drive, and one has an external drive. A combined system with both internal and external drives would be exciting (but also challenging) to study because it would have many degrees of freedom. Combining internal and external drives could enable even more precise control of transport phenomena.

Experimental realization Beck et al. [124] implemented the modified Rudner-Lindner-Berg-Levin model in photonic waveguides. This experimental platform would also be suitable for the coupled chains. Because the direction of motion in this system depends on the initial configuration, it could be used to optically transport signals and perform computations.

Quantum simulation and sensing A slight change in the initial configuration of the two particles in the coupled chains switches the transport from left-moving to right-moving or off. This sensitivity could act as a switch in a quantum computer or enhance the accuracy of measurements for improved sensing devices.

Bibliography

[1] H. Drüeke and D. Bauer: "Robustness of topologically sensitive harmonic generation in laser-driven linear chains", *Physical Review A* 99.5 (2019), 053402, DOI: 10.1103/PhysRevA.99.053402

[2] H. Drüeke and D. Bauer: "High-harmonic spectra of hexagonal nanoribbons from real-space time-dependent Schrödinger calculations", *The European Physical Journal Special Topics* 230.23 (2021), 4065–4070, DOI: 10.1140/epjs/s11734-021-00188-9

[3] H. Drüeke, M. Meschede, and D. Bauer: "Steering edge currents through a Floquet topological insulator", *Physical Review Research* 5.2 (2023), 023056, DOI: 10.1103/PhysRevResearch.5.023056

[4] H. Drüeke and D. Bauer: "Interaction-induced directional transport on periodically driven chains", *Physical Review Research* 6.2 (2024), 023032, DOI: 10.1103/PhysRevResearch.6.023032

[5] J. Beck, M. Heinrich, M. Meschede, H. Drüeke, F. Piccioli, S. Weidemann, J. Feis, D. Bauer, and A. Szameit: "Drive-induced Non-local Interactions and Topological Bulk Transport of Extended Doublons", *submitted for publication* (2024)

[6] G. Floquet: "Sur les équations différentielles linéaires à coefficients périodiques", *Annales scientifiques de l'École Normale Supérieure* 12 (1883), 47–88, DOI: 10.24033/asens.220

[7] F. Bloch: "Über die Quantenmechanik der Elektronen in Kristallgittern", *Zeitschrift für Physik* 52.7 (1929), 555–600, DOI: 10.1007/BF01339455

[8] M. Bukov, L. D'Alessio, and A. Polkovnikov: "Universal high-frequency behavior of periodically driven systems: from dynamical stabilization to Floquet engineering", *Advances in Physics* 64.2 (2015), 139–226, DOI: 10.1080/00018732.2015.1055918

[9] R. Moessner and S. L. Sondhi: "Equilibration and order in quantum Floquet matter", *Nature Physics* 13.5 (2017), 424–428, DOI: 10.1038/nphys4106

[10] F. Harper, R. Roy, M. S. Rudner, and S. L. Sondhi: "Topology and Broken Symmetry in Floquet Systems", *Annual Review of Condensed Matter Physics* 11.1 (2020), 345–368, DOI: 10.1146/annurev-conmatphys-031218-013721

[11] M. S. Rudner and N. H. Lindner: "Band structure engineering and non-equilibrium dynamics in Floquet topological insulators", *Nature Reviews Physics* 2.5 (2020), 229–244, DOI: 10.1038/s42254-020-0170-z

[12] M. S. Rudner and N. H. Lindner: *The Floquet Engineer's Handbook*, 2020, DOI: 10.48550/arXiv.2003.08252

[13] C. Cohen-Tannoudji, B. Diu, and F. Laloë: "Quantenmechanik - Band 3 Fermionen, Bosonen, Photonen, Korrelationen und Verschränkung", *Quantenmechanik - Band 3 Fermionen, Bosonen, Photonen, Korrelationen und Verschränkung*, De Gruyter, 2020

[14] E. H. Hall: "On a New Action of the Magnet on Electric Currents", *American Journal of Mathematics* 2.3 (1879), 287–292, DOI: 10.2307/2369245

[15] H. A. Lorentz: *Versuch einer Theorie der electrischen und optischen Erscheinungen in bewegten Körpern*, Cambridge Library Collection - Physical Sciences, Cambridge: Cambridge University Press, 2013, DOI: 10.1017/CBO9781139381406

[16] L. Landau: "Diamagnetismus der Metalle", *Zeitschrift für Physik* 64.9 (1930), 629–637, DOI: 10.1007/BF01397213

[17] K. von Klitzing, T. Chakraborty, P. Kim, V. Madhavan, X. Dai, J. McIver, Y. Tokura, L. Savary, D. Smirnova, A. M. Rey, C. Felser, J. Gooth, and X. Qi: "40 years of the quantum Hall effect", *Nature Reviews Physics* 2.8 (2020), 397–401, DOI: 10.1038/s42254-020-0209-1

[18] T. Ando, Y. Matsumoto, and Y. Uemura: "Theory of Hall Effect in a Two-Dimensional Electron System", *Journal of the Physical Society of Japan* 39.2 (1975), 279–288, DOI: 10.1143/JPSJ.39.279

[19] K. von Klitzing, G. Dorda, and M. Pepper: "New Method for High-Accuracy Determination of the Fine-Structure Constant Based on Quantized Hall Resistance", *Physical Review Letters* 45.6 (1980), 494–497, DOI: 10.1103/PhysRevLett.45.494

[20] *The Nobel Prize in Physics 1985*, NobelPrize.org, 1985, URL: https://www.nobelprize.org/prizes/physics/1985/summary/

[21] D. C. Tsui, H. L. Stormer, and A. C. Gossard: "Two-Dimensional Magnetotransport in the Extreme Quantum Limit", *Physical Review Letters* 48.22 (1982), 1559–1562, DOI: 10.1103/PhysRevLett.48.1559

[22] R. B. Laughlin: "Anomalous Quantum Hall Effect: An Incompressible Quantum Fluid with Fractionally Charged Excitations", *Physical Review Letters* 50.18 (1983), 1395–1398, DOI: 10.1103/PhysRevLett.50.1395

[23] *The Nobel Prize in Physics 1998*, NobelPrize.org, 1998, URL: https://www.nobelprize.org/prizes/physics/1998/summary/

[24] S.-Q. Shen: *Topological Insulators: Dirac Equation in Condensed Matters*, vol. 174, Springer Series in Solid-State Sciences, Berlin, Heidelberg: Springer, 2012, DOI: 10.1007/978-3-642-32858-9

[25] M. Fruchart and D. Carpentier: "An introduction to topological insulators", *Comptes Rendus Physique* 14.9 (2013), 779–815, DOI: 10.1016/j.crhy.2013.09.013

[26] J. K. Asbóth, L. Oroszlány, and A. Pályi: *A Short Course on Topological Insulators*, vol. 919, Lecture Notes in Physics, Cham: Springer International Publishing, 2016, DOI: 10.1007/978-3-319-25607-8

[27] F. D. M. Haldane: "Model for a Quantum Hall Effect without Landau Levels: Condensed-Matter Realization of the "Parity Anomaly"", *Physical Review Letters* 61.18 (1988), 2015–2018, DOI: 10.1103/PhysRevLett.61.2015

[28] *The Nobel Prize in Physics 2016*, NobelPrize.org, 2016, URL: https://www.nobelprize.org/prizes/physics/2016/summary/

[29] A. Kitaev: "Periodic table for topological insulators and superconductors", *AIP Conference Proceedings* 1134.1 (2009), 22–30, DOI: 10.1063/1.3149495

[30] M. He, H. Sun, and Q. L. He: "Topological insulator: Spintronics and quantum computations", *Frontiers of Physics* 14.4 (2019), 43401, DOI: 10.1007/s11467-019-0893-4

[31] G. Ma, M. Xiao, and C. T. Chan: "Topological phases in acoustic and mechanical systems", *Nature Reviews Physics* 1.4 (2019), 281–294, DOI: 10.1038/s42254-019-0030-x

[32] F. Zangeneh-Nejad, A. Alù, and R. Fleury: "Topological wave insulators: a review", *Comptes Rendus Physique* 21.4 (2020), 467–499, DOI: 10.5802/crphys.3

[33] H. Xue, Y. Yang, and B. Zhang: "Topological acoustics", *Nature Reviews Materials* 7.12 (2022), 974–990, DOI: 10.1038/s41578-022-00465-6

[34] X. Ni, S. Yves, A. Krasnok, and A. Alù: "Topological Metamaterials", *Chemical Reviews* 123.12 (2023), 7585–7654, DOI: 10.1021/acs.chemrev.2c00800

[35] W. Zhu, W. Deng, Y. Liu, J. Lu, H.-X. Wang, Z.-K. Lin, X. Huang, J.-H. Jiang, and Z. Liu: "Topological phononic metamaterials", *Reports on Progress in Physics* 86.10 (2023), 106501, DOI: 10.1088/1361-6633/aceeee

[36] T. Ozawa, H. M. Price, A. Amo, N. Goldman, M. Hafezi, L. Lu, M. C. Rechtsman, D. Schuster, J. Simon, O. Zilberberg, and I. Carusotto: "Topological photonics", *Reviews of Modern Physics* 91.1 (2019), 015006, DOI: 10.1103/RevModPhys.91.015006

[37] D. Smirnova, D. Leykam, Y. Chong, and Y. Kivshar: "Nonlinear topological photonics", *Applied Physics Reviews* 7.2 (2020), 021306, DOI: 10.1063/1.5142397

[38] M. Kim, Z. Jacob, and J. Rho: "Recent advances in 2D, 3D and higher-order topological photonics", *Light: Science & Applications* 9.1 (2020), 130, DOI: 10.1038/s41377-020-0331-y

[39] D. T. H. Tan: "Topological Silicon Photonics", *Advanced Photonics Research* 2.9 (2021), 2100010, DOI: 10.1002/adpr.202100010

[40] H. Price, Y. Chong, A. Khanikaev, H. Schomerus, L. J. Maczewsky, M. Kremer, M. Heinrich, A. Szameit, O. Zilberberg, Y. Yang, B. Zhang, A. Alù, R. Thomale, I. Carusotto, P. St-Jean, A. Amo, A. Dutt, L. Yuan, S. Fan, X. Yin, C. Peng, T. Ozawa, and A. Blanco-Redondo: "Roadmap on topological photonics", *Journal of Physics: Photonics* 4.3 (2022), 032501, DOI: 10.1088/2515-7647/ac4ee4

[41] H.-X. Wang and J.-H. Jiang: "A Short Review of All-Dielectric Topological Photonic Crystals", *Frontiers in Physics* 10 (2022), DOI: 10.3389/fphy.2022.866552

[42] J. Cayssol, B. Dóra, F. Simon, and R. Moessner: "Floquet topological insulators", *physica status solidi (RRL) – Rapid Research Letters* 7.1 (2013), 101–108, DOI: 10.1002/pssr.201206451

[43] H. N. S. Krishnamoorthy, A. M. Dubrovkin, G. Adamo, and C. Soci: "Topological Insulator Metamaterials", *Chemical Reviews* 123.8 (2023), 4416–4442, DOI: 10.1021/acs.chemrev.2c00594

[44] T. Oka and S. Kitamura: "Floquet Engineering of Quantum Materials", *Annual Review of Condensed Matter Physics* 10.1 (2019), 387–408, DOI: 10.1146/annurev-conmatphys-031218-013423

[45] I. Žutić, J. Fabian, and S. Das Sarma: "Spintronics: Fundamentals and applications", *Reviews of Modern Physics* 76.2 (2004), 323–410, DOI: 10.1103/RevModPhys.76.323

[46] A. V. Kimel, A. Kirilyuk, P. A. Usachev, R. V. Pisarev, A. M. Balbashov, and T. Rasing: "Ultrafast non-thermal control of magnetization by instantaneous photomagnetic pulses", *Nature* 435.7042 (2005), 655–657, DOI: 10.1038/nature03564

[47] C. D. Stanciu, F. Hansteen, A. V. Kimel, A. Kirilyuk, A. Tsukamoto, A. Itoh, and T. Rasing: "All-Optical Magnetic Recording with Circularly Polarized Light", *Physical Review Letters* 99.4 (2007), 047601, DOI: 10.1103/PhysRevLett.99.047601

[48] R. Roy and F. Harper: "Periodic table for Floquet topological insulators", *Physical Review B* 96.15 (2017), 155118, DOI: 10.1103/PhysRevB.96.155118

[49] B. Huang: "Topological invariants for anomalous Floquet higher-order topological insulators", *Frontiers of Physics* 18.1 (2022), 13601, DOI: 10.1007/s11467-022-1209-7

[50] M. S. Rudner, N. H. Lindner, E. Berg, and M. Levin: "Anomalous Edge States and the Bulk-Edge Correspondence for Periodically Driven Two-Dimensional Systems", *Physical Review X* 3.3 (2013), 031005, DOI: 10.1103/PhysRevX.3.031005

[51] R. Grimm, M. Weidemüller, and Y. B. Ovchinnikov: "Optical Dipole Traps for Neutral Atoms", *Advances In Atomic, Molecular, and Optical Physics*, ed. by B. Bederson and H. Walther, vol. 42, Academic Press, 2000, 95–170, DOI: 10.1016/S1049-250X(08)60186-X

[52] I. Bloch: "Ultracold quantum gases in optical lattices", *Nature Physics* 1.1 (2005), 23–30, DOI: 10.1038/nphys138

[53] C. Weitenberg and J. Simonet: "Tailoring quantum gases by Floquet engineering", *Nature Physics* 17.12 (2021), 1342–1348, DOI: 10.1038/s41567-021-01316-x

[54] I.-D. Potirniche, A. C. Potter, M. Schleier-Smith, A. Vishwanath, and N. Y. Yao: "Floquet Symmetry-Protected Topological Phases in Cold-Atom Systems", *Physical Review Letters* 119.12 (2017), 123601, DOI: 10.1103/PhysRevLett.119.123601

[55] J. H. Kang and Y.-i. Shin: "Topological Floquet engineering of a one-dimensional optical lattice via resonant shaking with two harmonic frequencies", *Physical Review A* 102.6 (2020), 063315, DOI: 10.1103/PhysRevA.102.063315

[56] K. Sandholzer, A.-S. Walter, J. Minguzzi, Z. Zhu, K. Viebahn, and T. Esslinger: "Floquet engineering of individual band gaps in an optical lattice using a two-tone drive", *Physical Review Research* 4.1 (2022), 013056, DOI: 10.1103/PhysRevResearch.4.013056

[57] F. N. Ünal, B. Seradjeh, and A. Eckardt: "How to Directly Measure Floquet Topological Invariants in Optical Lattices", *Physical Review Letters* 122.25 (2019), 253601, DOI: 10.1103/PhysRevLett.122.253601

[58] D.-H. Cai and W. Yi: "Synthetic topology and Floquet dynamic quantum phase transition in a periodically driven Raman lattice", *Physical Review A* 105.4 (2022), 042812, DOI: 10.1103/PhysRevA.105.042812

[59] J.-Y. Zhang, C.-R. Yi, L. Zhang, R.-H. Jiao, K.-Y. Shi, H. Yuan, W. Zhang, X.-J. Liu, S. Chen, and J.-W. Pan: "Tuning Anomalous Floquet Topological Bands with Ultracold Atoms", *Physical Review Letters* 130.4 (2023), 043201, DOI: 10.1103/PhysRevLett.130.043201

[60] Y. Lei, X.-W. Luo, and S. Zhang: "Second-order topological insulator in periodically driven optical lattices", *Optics Express* 30.13 (2022), 24048–24061, DOI: 10.1364/OE.457757

[61] H. Liu, T.-S. Xiong, W. Zhang, and J.-H. An: "Floquet engineering of exotic topological phases in systems of cold atoms", *Physical Review A* 100.2 (2019), 023622, DOI: 10.1103/PhysRevA.100.023622

[62] K. Itoh, W. Watanabe, S. Nolte, and C. B. Schaffer: "Ultrafast Processes for Bulk Modification of Transparent Materials", *MRS Bulletin* 31.8 (2006), 620–625, DOI: 10.1557/mrs2006.159

[63] A. Szameit and S. Nolte: "Discrete optics in femtosecond-laser-written photonic structures", *Journal of Physics B: Atomic, Molecular and Optical Physics* 43.16 (2010), 163001, DOI: 10.1088/0953-4075/43/16/163001

[64] M. C. Rechtsman, J. M. Zeuner, Y. Plotnik, Y. Lumer, D. Podolsky, F. Dreisow, S. Nolte, M. Segev, and A. Szameit: "Photonic Floquet topological insulators", *Nature* 496 (2013), 196–200

[65] S. Stützer, Y. Plotnik, Y. Lumer, P. Titum, N. H. Lindner, M. Segev, M. C. Rechtsman, and A. Szameit: "Photonic topological Anderson insulators", *Nature* 560.7719 (2018), 461–465, DOI: 10.1038/s41586-018-0418-2

[66] S. Wu, W. Song, S. Gao, Y. Chen, S. Zhu, and T. Li: "Floquet π mode engineering in non-Hermitian waveguide lattices", *Physical Review Research* 3.2 (2021), 023211, DOI: 10.1103/PhysRevResearch.3.023211

[67] J. Park, H. Cho, S. Lee, K. Lee, K. Lee, H. C. Park, J.-W. Ryu, N. Park, S. Jeon, and B. Min: "Revealing non-Hermitian band structure of photonic Floquet media", *Science Advances* 8.40 (2022), eabo6220, DOI: 10.1126/sciadv.abo6220

[68] L. J. Maczewsky, M. Heinrich, M. Kremer, S. K. Ivanov, M. Ehrhardt, F. Martinez, Y. V. Kartashov, V. V. Konotop, L. Torner, D. Bauer, and A. Szameit: "Nonlinearity-induced photonic topological insulator", *Science* 370.6517 (2020), 701–704, DOI: 10.1126/science.abd2033

[69] G. Scappucci, P. J. Taylor, J. R. Williams, T. Ginley, and S. Law: "Crystalline materials for quantum computing: Semiconductor heterostructures and topological insulators exemplars", *MRS Bulletin* 46.7 (2021), 596–606, DOI: 10.1557/s43577-021-00147-8

[70] K. Amini, J. Biegert, F. Calegari, A. Chacón, M. F. Ciappina, A. Dauphin, D. K. Efimov, C. F. d. M. Faria, K. Giergiel, P. Gniewek, A. S. Landsman, M. Lesiuk, M. Mandrysz, A. S. Maxwell, R. Moszyński, L. Ortmann, J. A. Pérez-Hernández, A. Picón, E. Pisanty, J. Prauzner-Bechcicki, K. Sacha, N. Suárez, A. Zaïr, J. Zakrzewski, and M. Lewenstein: "Symphony on strong field approximation", *Reports on Progress in Physics* 82.11 (2019), 116001, DOI: 10.1088/1361-6633/ab2bb1

[71] P. Agostini, F. Fabre, G. Mainfray, G. Petite, and N. K. Rahman: "Free-Free Transitions Following Six-Photon Ionization of Xenon Atoms", *Physical Review Letters* 42.17 (1979), 1127–1130, DOI: 10.1103/PhysRevLett.42.1127

[72] J. H. Eberly, J. Javanainen, and K. Rzążewski: "Above-threshold ionization", *Physics Reports* 204.5 (1991), 331–383, DOI: 10.1016/0370-1573(91)90131-5

[73] A. L'Huillier, L. A. Lompre, G. Mainfray, and C. Manus: "Multiply Charged Ions Formed by Multiphoton Absorption Processes in the Continuum", *Physical Review Letters* 48.26 (1982), 1814–1817, DOI: 10.1103/PhysRevLett.48.1814

[74] A. l'Huillier, L. A. Lompre, G. Mainfray, and C. Manus: "Multiply charged ions induced by multiphoton absorption in rare gases at 0.53 µm", *Physical Review A* 27.5 (1983), 2503–2512, DOI: 10.1103/PhysRevA.27.2503

[75] A. McPherson, G. Gibson, H. Jara, U. Johann, T. S. Luk, I. A. McIntyre, K. Boyer, and C. K. Rhodes: "Studies of multiphoton production of vacuum-ultraviolet radiation in the rare gases", *Journal of the Optical Society of America B* 4.4 (1987), 595–601, DOI: 10.1364/JOSAB.4.000595

[76] M. Ferray, A. L'Huillier, X. F. Li, L. A. Lompre, G. Mainfray, and C. Manus: "Multiple-harmonic conversion of 1064 nm radiation in rare gases", *Journal of Physics B: Atomic, Molecular and Optical Physics* 21.3 (1988), L31, DOI: 10.1088/0953-4075/21/3/001

[77] K. Midorikawa: "High-Order Harmonic Generation and Attosecond Science", *Japanese Journal of Applied Physics* 50.9 (2011), 090001, DOI: 10.1143/JJAP.50.090001

[78] M. C. Kohler, T. Pfeifer, K. Z. Hatsagortsyan, and C. H. Keitel: "Chapter 4 - Frontiers of Atomic High-Harmonic Generation", *Advances In Atomic, Molecular, and Optical Physics*, ed. by P. Berman, E. Arimondo, and C. Lin, vol. 61, Academic Press, 2012, 159–208, DOI: 10.1016/B978-0-12-396482-3.00004-1

[79] R. Weissenbilder, S. Carlström, L. Rego, C. Guo, C. M. Heyl, P. Smorenburg, E. Constant, C. L. Arnold, and A. L'Huillier: "How to optimize high-order harmonic generation in gases", *Nature Reviews Physics* 4.11 (2022), 713–722, DOI: 10.1038/s42254-022-00522-7

[80] M. Y. Kuchiev: "Atomic antenna", *Journal of Experimental and Theoretical Physics Letters* 45 (1987), 404

[81] F. Brunel: "Not-so-resonant, resonant absorption", *Physical Review Letters* 59.1 (1987), 52–55, DOI: 10.1103/PhysRevLett.59.52

[82] P. B. Corkum, N. H. Burnett, and F. Brunel: "Above-threshold ionization in the long-wavelength limit", *Physical Review Letters* 62.11 (1989), 1259–1262, DOI: 10.1103/PhysRevLett.62.1259

[83] F. Brunel: "Harmonic generation due to plasma effects in a gas undergoing multiphoton ionization in the high-intensity limit", *JOSA B* 7.4 (1990), 521–526, DOI: 10.1364/JOSAB.7.000521

[84] F. Ehlotzky: "Harmonic generation in keldysh-type models", *Il Nuovo Cimento D* 14.5 (1992), 517–525, DOI: 10.1007/BF02457041

[85] K. C. Kulander, K. J. Schafer, and J. L. Krause: "Dynamics of Short-Pulse Excitation, Ionization and Harmonic Conversion", *Super-Intense Laser-Atom Physics*, ed. by B. Piraux, A. L'Huillier, and K. Rzążewski, NATO ASI Series, Boston, MA: Springer US, 1993, 95–110, DOI: 10.1007/978-1-4615-7963-2_10

[86] H. G. Muller and M. P. de Boer: "Population Trapping in Excited States", *Super-Intense Laser-Atom Physics*, ed. by B. Piraux, A. L'Huillier, and K. Rzążewski, NATO ASI Series, Boston, MA: Springer US, 1993, 279–286, DOI: 10.1007/978-1-4615-7963-2_24

[87] P. B. Corkum: "Plasma perspective on strong field multiphoton ionization", *Physical Review Letters* 71.13 (1993), 1994–1997, DOI: 10.1103/PhysRevLett.71.1994

[88] L. V. Keldysh: "Ionization in the Field of a Strong Electromagnetic Wave", *Soviet Journal of Experimental and Theoretical Physics* 20.5 (1965), 1307–1314

[89] S. V. Popruzhenko: "Keldysh theory of strong field ionization: history, applications, difficulties and perspectives", *Journal of Physics B: Atomic, Molecular and Optical Physics* 47.20 (2014), 204001, DOI: 10.1088/0953-4075/47/20/204001

[90] N. Boroumand, A. Thorpe, A. M. Parks, and T. Brabec: "Keldysh ionization theory of atoms: mathematical details", *Journal of Physics B: Atomic, Molecular and Optical Physics* 55.21 (2022), 213001, DOI: 10.1088/1361-6455/ac9205

[91] M. V. Ammosov, N. B. Delone, and V. P. Krainov: "Tunnel ionization of complex atoms and of atomic ions in an alternating electromagnetic field", *Soviet Journal of Experimental and Theoretical Physics* 64 (1986), 1191, DOI: 10.1117/12.938695

[92] S. Augst, D. Strickland, D. D. Meyerhofer, S. L. Chin, and J. H. Eberly: "Tunneling ionization of noble gases in a high-intensity laser field", *Physical Review Letters* 63.20 (1989), 2212–2215, DOI: 10.1103/PhysRevLett.63.2212

[93] S. Augst, D. D. Meyerhofer, D. Strickland, and S. L. Chin: "Laser ionization of noble gases by Coulomb-barrier suppression", *JOSA B* 8.4 (1991), 858–867, DOI: 10.1364/JOSAB.8.000858

[94] V. P. Krainov: "Theory of barrier-suppression ionization of atoms", *Journal of Nonlinear Optical Physics & Materials* 04.4 (1995), 775–798, DOI: 10.1142/S0218863595000343

[95] V. P. Krainov: "Ionization rates and energy and angular distributions at the barrier-suppression ionization of complex atoms and atomic ions", *JOSA B* 14.2 (1997), 425–431, DOI: 10.1364/JOSAB.14.000425

[96] D. Bauer and P. Mulser: "Exact field ionization rates in the barrier-suppression regime from numerical time-dependent Schrödinger-equation calculations", *Physical Review A* 59.1 (1999), 569–577, DOI: 10.1103/PhysRevA.59.569

[97] T. B. Miladinović and V. M. Petrović: "Laser Field Ionization Rates in the Barrier-Suppression Regime", *Journal of Russian Laser Research* 36.4 (2015), 312–319, DOI: 10.1007/s10946-015-9505-0

[98] I. Y. Kostyukov and A. A. Golovanov: "Field ionization in short and extremely intense laser pulses", *Physical Review A* 98.4 (2018), 043407, DOI: 10.1103/PhysRevA.98.043407

[99] J. Wang, Z. Guo, Y. Fang, X. Yu, and Y. Liu: "Over-barrier ionization of hydrogen atom in intense circular and elliptical laser fields", *Frontiers in Physics* 10 (2022)

[100] J. L. Krause, K. J. Schafer, and K. C. Kulander: "High-order harmonic generation from atoms and ions in the high intensity regime", *Physical Review Letters* 68.24 (1992), 3535–3538, DOI: 10.1103/PhysRevLett.68.3535

[101] R. A. Ganeev: "High-order harmonic generation in nanoparticle-containing laser-produced plasmas", *Laser Physics* 18.9 (2008), 1009–1015, DOI: 10.1134/S1054660X08090016

[102] S. Ghimire, A. D. DiChiara, E. Sistrunk, P. Agostini, L. F. DiMauro, and D. A. Reis: "Observation of high-order harmonic generation in a bulk crystal", *Nature Physics* 7.2 (2011), 138–141, DOI: 10.1038/nphys1847

[103] Y. S. You, Y. Yin, Y. Wu, A. Chew, X. Ren, F. Zhuang, S. Gholam-Mirzaei, M. Chini, Z. Chang, and S. Ghimire: "High-harmonic generation in amorphous solids", *Nature Communications* 8.1 (2017), 724, DOI: 10.1038/s41467-017-00989-4

[104] S. Ghimire and D. A. Reis: "High-harmonic generation from solids", *Nature Physics* 15.1 (2019), 10–16, DOI: 10.1038/s41567-018-0315-5

[105] L. Ortmann and A. S. Landsman: "Chapter Two - High-harmonic generation in solids", *Advances In Atomic, Molecular, and Optical Physics*, ed. by L. F. Dimauro, H. Perrin, and S. F. Yelin, vol. 70, Academic Press, 2021, 103–156, DOI: 10.1016/bs.aamop.2021.04.002

[106] E. Goulielmakis and T. Brabec: "High harmonic generation in condensed matter", *Nature Photonics* 16.6 (2022), 411–421, DOI: 10.1038/s41566-022-00988-y

[107] J. Park, A. Subramani, S. Kim, and M. F. Ciappina: "Recent trends in high-order harmonic generation in solids", *Advances in Physics: X* 7.1 (2022), 2003244, DOI: 10.1080/23746149.2021.2003244

[108] L. Yue and M. B. Gaarde: "Introduction to theory of high-harmonic generation in solids: tutorial", *Journal of the Optical Society of America B* 39.2 (2022), 535–555, DOI: 10.1364/JOSAB.448602

[109] L. Li, P. Lan, X. Zhu, and P. Lu: "High harmonic generation in solids: particle and wave perspectives", *Reports on Progress in Physics* 86.11 (2023), 116401, DOI: 10.1088/1361-6633/acf144

[110] C. Yu, S. Jiang, and R. Lu: "High order harmonic generation in solids: a review on recent numerical methods", *Advances in Physics: X* 4.1 (2019), 1562982, DOI: 10.1080/23746149.2018.1562982

[111] G. Vampa and T. Brabec: "Merge of high harmonic generation from gases and solids and its implications for attosecond science", *Journal of Physics B: Atomic, Molecular and Optical Physics* 50.8 (2017), 083001, DOI: 10.1088/1361-6455/aa528d

[112] R.-X. Zuo, X.-H. Song, X.-W. Liu, S.-D. Yang, and W.-F. Yang: "Influence of intraband motion on the interband excitation and high harmonic generation", *Chinese Physics B* 28.9 (2019), 094208, DOI: 10.1088/1674-1056/ab3446

[113] N. Ben-Tal, N. Moiseyev, and A. Beswick: "The effect of Hamiltonian symmetry on generation of odd and even harmonics", *Journal of Physics B: Atomic, Molecular and Optical Physics* 26.18 (1993), 3017, DOI: 10.1088/0953-4075/26/18/012

[114] F. Ceccherini, D. Bauer, and F. Cornolti: "Dynamical symmetries and harmonic generation", *Journal of Physics B: Atomic, Molecular and Optical Physics* 34.24 (2001), 5017, DOI: 10.1088/0953-4075/34/24/305

[115] O. Neufeld, D. Podolsky, and O. Cohen: "Floquet group theory and its application to selection rules in harmonic generation", *Nature Communications* 10.1 (2019), 405, DOI: 10.1038/s41467-018-07935-y

[116] P. Reimann: "Brownian motors: noisy transport far from equilibrium", *Physics Reports* 361.2 (2002), 57–265, DOI: 10.1016/S0370-1573(01)00081-3

[117] P. Hänggi and F. Marchesoni: "Artificial Brownian motors: Controlling transport on the nanoscale", *Reviews of Modern Physics* 81.1 (2009), 387–442, DOI: 10.1103/RevModPhys.81.387

[118] S. Yukawa, M. Kikuchi, G. Tatara, and H. Matsukawa: "Quantum Ratchets", *Journal of the Physical Society of Japan* 66.10 (1997), 2953–2956, DOI: 10.1143/JPSJ.66.2953

[119] P. Reimann, M. Grifoni, and P. Hänggi: "Quantum Ratchets", *Physical Review Letters* 79.1 (1997), 10–13, DOI: 10.1103/PhysRevLett.79.10

[120] N. Dupont, L. Gabardos, F. Arrouas, N. Ombredane, J. Billy, B. Peaudecerf, and D. Guéry-Odelin: "Hamiltonian Ratchet for Matter-Wave Transport", *Physical Review Letters* 131.13 (2023), 133401, DOI: 10.1103/PhysRevLett.131.133401

[121] D. J. Thouless: "Quantization of particle transport", *Physical Review B* 27.10 (1983), 6083–6087, DOI: 10.1103/PhysRevB.27.6083

[122] R. Citro and M. Aidelsburger: "Thouless pumping and topology", *Nature Reviews Physics* 5.2 (2023), 87–101, DOI: 10.1038/s42254-022-00545-0

[123] I. I. Rabi: "Space Quantization in a Gyrating Magnetic Field", *Physical Review* 51.8 (1937), 652–654, DOI: 10.1103/PhysRev.51.652

[124] J. Beck, H. Drüeke, M. J. Meschede, M. Heinrich, F. S. Piccioli, S. Weidemann, D. Bauer, and A. Szameit: "Observation of Interaction-Induced Topological Doublon States", *2023 Conference on Lasers and Electro-Optics Europe & European Quantum Electronics Conference*, 2023, DOI: 10.1109/CLEO/Europe-EQEC57999.2023.10231749

[125] H. Drüeke and D. Bauer: "High-harmonic spectra of hexagonal nanoribbons from real-space time-dependent Schrödinger calculations: data repository", *Open Science Framework* (2021), DOI: 10.17605/osf.io/8rtfu

[126] G. Castiglia, P. P. Corso, D. Cricchio, R. Daniele, E. Fiordilino, F. Morales, and F. Persico: "High-order-harmonic generation in dimensionally reduced systems", *Physical Review A* 88.3 (2013), 033837, DOI: 10.1103/PhysRevA.88.033837

[127] K. K. Hansen, D. Bauer, and L. B. Madsen: "Finite-system effects on high-order harmonic generation: From atoms to solids", *Physical Review A* 97.4 (2018), 043424, DOI: 10.1103/PhysRevA.97.043424

[128] D. Bauer and K. K. Hansen: "High-Harmonic Generation in Solids with and without Topological Edge States", *Physical Review Letters* 120.17 (2018), DOI: 10.1103/PhysRevLett.120.177401

[129] Y. Murakami, S. Takayoshi, A. Koga, and P. Werner: "High-harmonic generation in one-dimensional Mott insulators", *Physical Review B* 103.3 (2021), 035110, DOI: 10.1103/PhysRevB.103.035110

[130] D. Dimitrovski, L. B. Madsen, and T. G. Pedersen: "High-order harmonic generation from gapped graphene: Perturbative response and transition to nonperturbative regime", *Physical Review B* 95.3 (2017), 035405, DOI: 10.1103/PhysRevB.95.035405

[131] H. Liu, Y. Li, Y. S. You, S. Ghimire, T. F. Heinz, and D. A. Reis: "High-harmonic generation from an atomically thin semiconductor", *Nature Physics* 13.3 (2017), 262–265, DOI: 10.1038/nphys3946

[132] D. Dimitrovski, T. G. Pedersen, and L. B. Madsen: "Floquet-Bloch shifts in two-band semiconductors interacting with light", *Physical Review A* 95.6 (2017), 063420, DOI: 10.1103/PhysRevA.95.063420

[133] N. Tancogne-Dejean and A. Rubio: "Atomic-like high-harmonic generation from two-dimensional materials", *Science Advances* 4.2 (2018), eaao5207, DOI: 10.1126/sciadv.aao5207

[134] C. Orthodoxou, A. Zaïr, and G. H. Booth: "High harmonic generation in two-dimensional Mott insulators", *npj Quantum Materials* 6.1 (2021), 1–8, DOI: 10.1038/s41535-021-00377-8

[135] J. C. Baggesen and L. B. Madsen: "On the dipole, velocity and acceleration forms in high-order harmonic generation from a single atom or molecule", *Journal of Physics B: Atomic, Molecular and Optical Physics* 44.11 (2011), 115601

[136] F. J. Harris: "On the use of windows for harmonic analysis with the discrete Fourier transform", *Proceedings of the IEEE* 66.1 (1978), 51–83, DOI: 10.1109/PROC.1978.10837

[137] D. Bauer, ed.: *Computational Strong-Field Quantum Dynamics: Intense Light-Matter Interactions*, De Gruyter Textbook, De Gruyter, 2017

[138] H. Jürß and D. Bauer: "High-order harmonic generation in hexagonal nanoribbons", *The European Physical Journal Special Topics* (2021), DOI: 10.1140/epjs/s11734-021-00106-z

[139] S. Inouye, M. R. Andrews, J. Stenger, H.-J. Miesner, D. M. Stamper-Kurn, and W. Ketterle: "Observation of Feshbach resonances in a Bose–Einstein condensate", *Nature* 392.6672 (1998), 151–154, DOI: 10.1038/32354

[140] C. Chin, R. Grimm, P. Julienne, and E. Tiesinga: "Feshbach resonances in ultracold gases", *Reviews of Modern Physics* 82.2 (2010), 1225–1286, DOI: 10.1103/RevModPhys.82.1225

[141] P. Courteille, R. S. Freeland, D. J. Heinzen, F. A. van Abeelen, and B. J. Verhaar: "Observation of a Feshbach Resonance in Cold Atom Scattering", *Physical Review Letters* 81.1 (1998), 69–72, DOI: 10.1103/PhysRevLett.81.69

[142] Y. Cheng and Z.-Y. Shi: "Many-body dynamics with time-dependent interaction", *Physical Review A* 104.2 (2021), 023307, DOI: 10.1103/PhysRevA.104.023307

[143] P. Engels, C. Atherton, and M. A. Hoefer: "Observation of Faraday Waves in a Bose-Einstein Condensate", *Physical Review Letters* 98.9 (2007), 095301, DOI: 10.1103/PhysRevLett.98.095301

[144] J. H. V. Nguyen, M. C. Tsatsos, D. Luo, A. U. J. Lode, G. D. Telles, V. S. Bagnato, and R. G. Hulet: "Parametric Excitation of a Bose-Einstein Condensate: From Faraday Waves to Granulation", *Physical Review X* 9.1 (2019), 011052, DOI: 10.1103/PhysRevX.9.011052

[145] L. W. Clark, A. Gaj, L. Feng, and C. Chin: "Collective emission of matter-wave jets from driven Bose–Einstein condensates", *Nature* 551.7680 (2017), 356–359, DOI: 10.1038/nature24272

[146] H. Fu, L. Feng, B. M. Anderson, L. W. Clark, J. Hu, J. W. Andrade, C. Chin, and K. Levin: "Density Waves and Jet Emission Asymmetry in Bose Fireworks", *Physical Review Letters* 121.24 (2018), 243001, DOI: 10.1103/PhysRevLett.121.243001

[147] Z. Wu and H. Zhai: "Dynamics and density correlations in matter-wave jet emission of a driven condensate", *Physical Review A* 99.6 (2019), 063624, DOI: 10.1103/PhysRevA.99.063624

Part II.

Publications

7. Interaction-induced directional transport on periodically driven chains

H. Drüeke and D. Bauer: "Interaction-induced directional transport on periodically driven chains" *Physical Review Research* 6.2 (2024), 023032 DOI: 10.1103/PhysRevResearch.6.023032

Interaction-induced directional transport on periodically driven chains

Helena Drüeke [*] and Dieter Bauer [†]
Institute of Physics, University of Rostock, 18051 Rostock, Germany

(Received 16 October 2023; revised 16 January 2024; accepted 21 February 2024; published 8 April 2024)

We study a driven system in which interaction between particles causes their directional, coupled movement. In that model system, two particles move alternatingly in time on two coupled chains. Without interaction, both particles diffuse along their respective chains, independent from one another. Interaction between them, whether attractive or repellent, leads to an energetic separation of configurations where the particles are close to each other and those where they are farther separated. The energy difference causes close-by particles to remain bound together, forming a doublon. Their relative position in the starting configuration determines whether the doublon moves to the left or right or remains stationary due to the periodic driving.

DOI: 10.1103/PhysRevResearch.6.023032

I. INTRODUCTION

Directional transport in physical systems can be realized in various ways. The most obvious one is applying an external field, e.g., an electric field that accelerates a charged particle in a particular direction or an inhomogeneous magnetic field that deflects atoms in different directions according to their spin. An alternating electric field can also lead to directional transport. A simple example is an electron emitted at, say, $t = 0$ into a linearly polarized laser field, e.g., by ionization. Depending on the emission time, the electron may drift in opposite directions, parallel to the polarization of the incident laser field. Other ways to achieve directional transport are by topologically protected edge currents through the breaking of time-reversal symmetry, e.g., by a magnetic field or spin-orbit coupling [Hall effect(s) [1–4]], or by periodic driving and asymmetric potentials [(semi)classical [5,6] and quantum ratchets [7–9], and Thouless pumping [10,11]]. All these systems prescribe the direction of movement of particles within them. Interactions between the particles will affect the particle dynamics, but as long as the particle interaction is symmetric under particle exchange, one would not expect directional transport to arise. In fact, one might expect that interaction, in general, would broaden momentum distributions, including peaks in such distributions that correspond to directional motion without interaction. The directional motion would then gradually disappear with increasing interaction strength. However, it has been shown recently that topologically protected motion survives to a certain extent in a Hubbard-Thouless pump [12]. Interaction might even be required to achieve directional transport in a topological many-body system [13].

In this work, we present a minimal model of a driven two-particle system that shows directional transport due to interaction, even though this interaction is symmetric under particle exchange. Moreover, the drive is spatially symmetric (unlike the laser example above) and no asymmetric potentials are involved (in contrast to the ratchet systems). Therefore, the direction of movement is not predetermined by the system parameters and depends on the initial condition.

The key to directional transport in our system is the alternating driving of the two particles. While the interaction in our model system is always active, the hopping of each particle is only allowed for half of the driving period. In this case, the initial configuration determines the direction in which the bound pair of particles (i.e., doublon) moves. Without interaction, the doublon does not exist and the two particles simply diffuse independently without preferred directionality. The alternating drive where only one of the two particles is allowed to move per half period implies that the two particles are distinguishable and should be independently addressable by external fields. Lin, Ke, and Lee [14] investigated a system similar to the one described in this work, as well as its implementation in ultracold atoms in optical lattices (see Sec. IV). Their two spin-1/2 particles experience different one-dimensional trapping lattices because one is spin-up and the other spin-down. In contrast to our work presented in this publication, the interaction between neighboring particles is not isotropic. By tuning hopping and interaction strengths, the two particles form topological bound states. Periodic modulation of these two parameters leads to topological Thouless pumping of the bound states. Without interaction, however, the system in [14] is topologically trivial and no transport occurs.

A related phenomenon is Coulomb drag [15], where a current in one conductor induces a current in a second, adjacent, but electrically isolated conductor. In our system, the two particles behave similarly but drag each other reciprocally without an external bias (voltage) on either conductor.

This publication consists of the following parts. We introduce the model in Sec. II and explore the behavior of one particle during half its driving period in Sec. III. The doublon dynamics can be conveniently analyzed by mapping

[*] helena.drueeke@uni-rostock.de
[†] dieter.bauer@uni-rostock.de

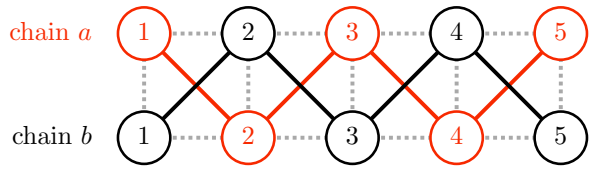

FIG. 1. Chains a and b of identical length $N = 5$ (we chose this small N for illustration purposes but performed all calculations with much longer chains). The red and black lines indicate the hopping J of particles a and b on their respective chains. Dashed gray lines indicate the interaction V between nearest-neighbor sites on different chains.

onto a 2D system, as discussed in Sec. IV. Section V describes possible experimental implementations. Finally, we conclude and discuss the significance of our work in Sec. VI.

We use units in which $\hbar = 1$.

II. SYSTEM

We consider the lattice shown in Fig. 1, consisting of two chains a and b of length N with one particle on each chain (also labeled a and b). Each particle may hop along its respective chain; hoppings to the other chain are prohibited. The particles move alternatingly, starting with particle a. The interaction between particles is between nearest neighbors, i.e., across the chains.

The Hamiltonian reads

$$\hat{H}(t) = \sum_{\langle i,j\rangle} (J_a(t)\hat{a}_i^\dagger \hat{a}_j + J_b(t)\hat{b}_i^\dagger \hat{b}_j) + V \sum_{\langle\langle i,j\rangle\rangle} \hat{n}_i^{(a)} \hat{n}_j^{(b)}, \quad (1)$$

where $\hat{a}_i$ and $\hat{b}_i$ are annihilation operators on site i of chains a and b, respectively, $\hat{a}_i^\dagger$ and $\hat{b}_i^\dagger$ are the corresponding creation operators, and $\hat{n}_i^{(a)} = \hat{a}_i^\dagger \hat{a}_i$ and $\hat{n}_j^{(b)} = \hat{b}_j^\dagger \hat{b}_j$ are the occupation number operators. $\langle i, j\rangle$ indicates nearest neighbors within a chain and $\langle\langle i, j\rangle\rangle$ nearest neighbors across the chains.

The hoppings $J_{a,b}(t)$ are assumed to be periodic with a period T and piecewise constant,

$$J_a(t) = \begin{cases} J, & 0 \leqslant t < T/2, \\ 0, & T/2 \leqslant t < T, \end{cases} \quad (2a)$$

$$J_b(t) = \begin{cases} 0, & 0 \leqslant t < T/2, \\ J, & T/2 \leqslant t < T. \end{cases} \quad (2b)$$

We choose $J = 1$ in all numerical calculations throughout this publication. With the labeling in Fig. 1, we can write

$$\hat{H}(t) = \sum_{i=1}^{N-1} \left((J_a(t)\hat{a}_i^\dagger \hat{a}_{i+1} + J_b(t)\hat{b}_i^\dagger \hat{b}_{i+1}) + \text{H.c.} \right.$$
$$\left. + V\left(\hat{n}_i^{(a)}\hat{n}_{i+1}^{(b)} + \hat{n}_{i+1}^{(a)}\hat{n}_i^{(b)}\right)\right) + V \sum_{i=1}^{N} \hat{n}_i^{(a)}\hat{n}_i^{(b)}. \quad (3)$$

III. MOVEMENT OF ONE PARTICLE DURING A HALF PERIOD

We investigate particle a's movement on its chain a during the first half period ($0 \leqslant t < T/2$). Particle a starts in site i and propagates. Particle b is located in site j and remains stationary during this time.

The Hamiltonian during this phase can be written as an $N \times N$ matrix

$$H = H_J + H_V. \quad (4)$$

It consists of two parts, one describing the hopping

$$H_J = \text{tridiag}(J, 0, J) = \begin{pmatrix} 0 & J & & 0 \\ J & 0 & \ddots & \\ & \ddots & \ddots & J \\ 0 & & J & 0 \end{pmatrix} \quad (5)$$

and one describing the interaction

$$H_V = (v_{k,l}), \quad (6)$$

with

$$v_{k,l} = \begin{cases} V, & k = l = j-1, j, j+1, \\ 0, & \text{else} \end{cases} \quad (7)$$

on sites neighboring the position j of particle b.

A. $|V| \gg J$

The interaction between particles is between neighboring sites, i.e., for states with $|i - j| \leqslant 1$. Therefore, a strong potential $|V| \gg J$ leads to a large energetic separation of the states $i = j - 1, j, j + 1$ from the others. If particle a starts its movement in a site i with $i < j - 1$ ($i > j + 1$), it cannot bridge this energy gap and will remain on the left side of particle b, $i < j - 1$ (right side, $i > j + 1$). Interestingly, it does not matter if the potential is repulsive ($V > 0$) or attractive ($V < 0$).

Assuming $|i - j| \leqslant 1$ with a strong potential $|V| \gg J$ confines particle a to the three sites $j - 1$, j, and $j+1$. The $N\times N$ Hamiltonian (4) becomes limited to these three states (3×3),

$$H = \begin{pmatrix} V & J & 0 \\ J & V & J \\ 0 & J & V \end{pmatrix}, \quad (8)$$

with eigenenergies

$$E_0 = V, \quad E_{1,2} = V \pm \sqrt{2}J \quad (9)$$

and eigenstates

$$\varphi_0 = \begin{pmatrix} 1 \\ 0 \\ -1 \end{pmatrix}, \quad \varphi_{1,2} = \begin{pmatrix} 1 \\ \pm\sqrt{2} \\ 1 \end{pmatrix}. \quad (10)$$

We can now write any time-dependent state as

$$\psi(t) = \sum_{h=0}^{2} c_h \exp(-\mathrm{i}E_h t)\varphi_h. \quad (11)$$

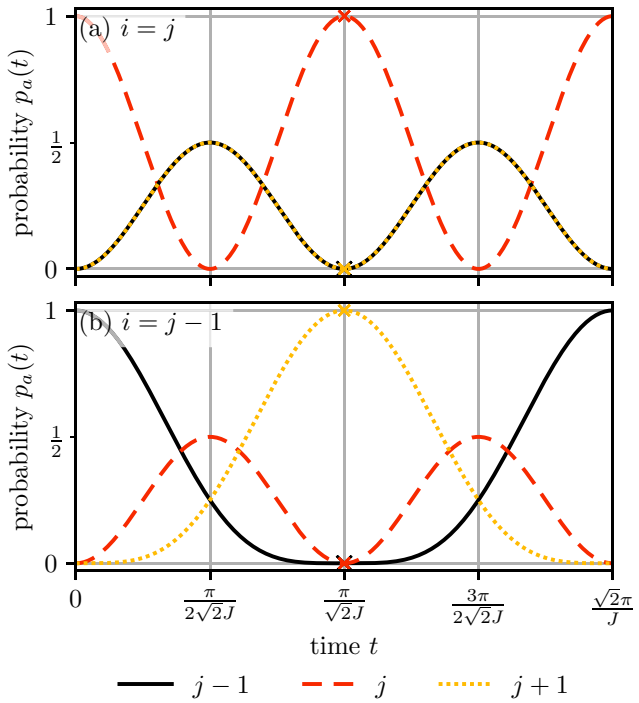

FIG. 2. Probabilities of particle a on different sites as a function of time with $|V| \gg J$ (a) for starting position $i = j$ and (b) for starting position $i = j - 1$. The crosses mark the probabilities at the end of the driving phase $t_a = \frac{\pi}{\sqrt{2}J}$.

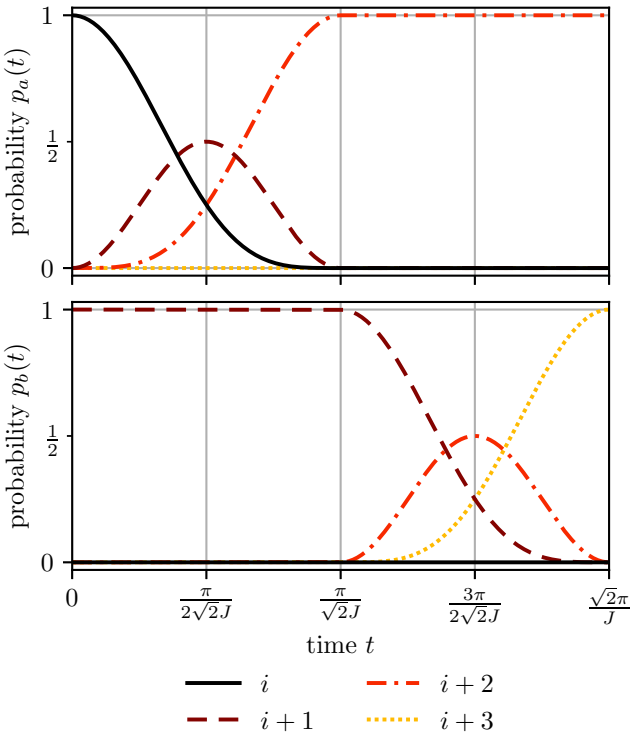

FIG. 3. Probabilities of particles a and b on different sites as a function of time. Particle a moves from site i via site $i+1$ to site $i+2$ during the first phase; then particle b moves from site $i+1$ via site $i+2$ to site $i+3$ during the second phase.

1. $i = j$

If particle a starts at $i = j$, $\psi_a(0) = (0, 1, 0)^\mathsf{T}$, the coefficients are $c_0 = 0$ and $c_{1,2} = \pm\frac{1}{2\sqrt{2}}$, resulting in

$$\psi_a(t) = \frac{\exp(-\mathrm{i}Vt)}{\sqrt{2}\mathrm{i}} \begin{pmatrix} \sin(\sqrt{2}Jt) \\ \sqrt{2}\mathrm{i}\,\cos(\sqrt{2}Jt) \\ \sin(\sqrt{2}Jt) \end{pmatrix}. \tag{12}$$

The probability at the three sites $i = j - 1, j, j + 1$ is

$$p_a(t) = |\psi_a(t)|^2 = \frac{1}{2} \begin{pmatrix} \sin^2(\sqrt{2}Jt) \\ 2\,\cos^2(\sqrt{2}Jt) \\ \sin^2(\sqrt{2}Jt) \end{pmatrix}, \tag{13}$$

shown in Fig. 2(a). The particle moves symmetrically from the starting site j to the left and right neighbors $j \pm 1$, where it reaches a maximum probability of 0.5 at time $t = \frac{\pi}{2\sqrt{2}J}$ before completely returning to site j at $t = \frac{\pi}{\sqrt{2}J}$.

2. $i = j - 1$

If particle a starts at $i = j - 1$, $\psi_a(0) = (1, 0, 0)^\mathsf{T}$, the coefficients are $c_0 = \frac{1}{2}$ and $c_{1,2} = \frac{1}{4}$, resulting in

$$\psi_a(t) = \frac{\exp(-\mathrm{i}Vt)}{2} \begin{pmatrix} 1 + \cos(\sqrt{2}Jt) \\ -\sqrt{2}\mathrm{i}\,\sin(\sqrt{2}Jt) \\ -1 + \cos(\sqrt{2}Jt) \end{pmatrix}. \tag{14}$$

The probability is

$$p_a(t) = \begin{pmatrix} \cos^4(Jt/\sqrt{2}) \\ \sin^2(\sqrt{2}Jt)/2 \\ \sin^4(Jt/\sqrt{2}) \end{pmatrix}, \tag{15}$$

shown in Fig. 2(b).

We choose $t_a = \frac{\pi}{\sqrt{2}J}$ to achieve a complete transfer of particle a from site $j - 1$ to site $j + 1$. Particle a leapfrogs over particle b from its left to right neighbor. If we choose the timing of the second phase of the driving cycle as $t_b = \frac{\pi}{\sqrt{2}J}$, particle b will leapfrog over particle a, leading to directional transport. Effectively, both particles move two sites to the right without spreading. Figure 3 shows the probabilities $p_a(t)$ and $p_b(t)$ for the complete cycle. Figure 4 shows a sketch of the particles' movement.

3. $i = j + 1$

If particle a starts at $i = j + 1$, $\psi_{i=j+1}(0) = (0, 0, 1)^\mathsf{T}$, it will analogously leapfrog over particle b to site $j - 1$, resulting in directional transport to the left.

B. $V = 0$

For potential $V = 0$, the position j of particle b does not influence particle a's movement. The Hamiltonian (4) simplifies

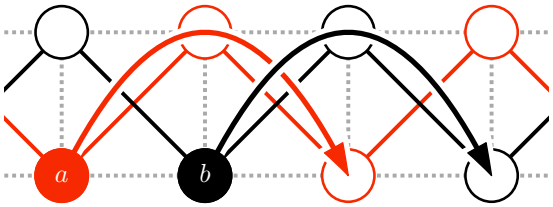

FIG. 4. Sketch of the leapfrogging movement of particles a and b during a complete driving cycle. During the first phase ($0 \leqslant t < T/2$), particle a jumps over particle b and two sites to the right. Then, during the second phase ($T/2 \leqslant t < T$), particle b jumps over particle a and two sites to the right.

to

$$H = H_J = \text{tridiag}(J, 0, J) = \begin{pmatrix} 0 & J & & 0 \\ J & 0 & \ddots & \\ & \ddots & \ddots & J \\ 0 & & J & 0 \end{pmatrix}. \quad (16)$$

The time-dependent Schrödinger equation

$$\mathrm{i}\partial_t \psi_a(t) = \hat{H}\psi_a(t) \quad (17)$$

leads to a diffusion-type equation for the time-dependent wave function $\psi(n,t)$ in site n,

$$\partial_t \psi_a(n,t) = -\mathrm{i}J(\psi_a(n-1,t) + \psi_a(n+1,t)). \quad (18)$$

For a particle starting in site i on an infinitely long chain, it follows [16] that

$$\psi_a(i+l,t) = \mathrm{i}^{-l}\mathcal{J}_l(2Jt) \quad (19)$$

and

$$p_a(i+l,t) = |\psi_a(i+l,t)|^2 = \mathcal{J}_l^2(2Jt), \quad (20)$$

where $\mathcal{J}_l$ is the Bessel function of the first kind.

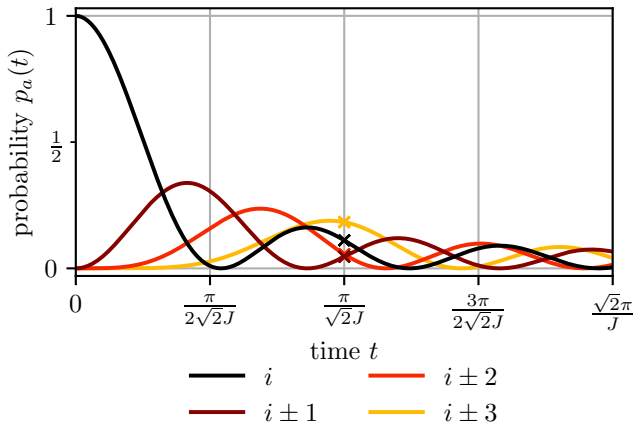

FIG. 5. Probabilities of particle a on different sites as a function of time with $V = 0$. The crosses mark the probabilities at the end of the driving phase $t_a = \frac{\pi}{\sqrt{2}J}$.

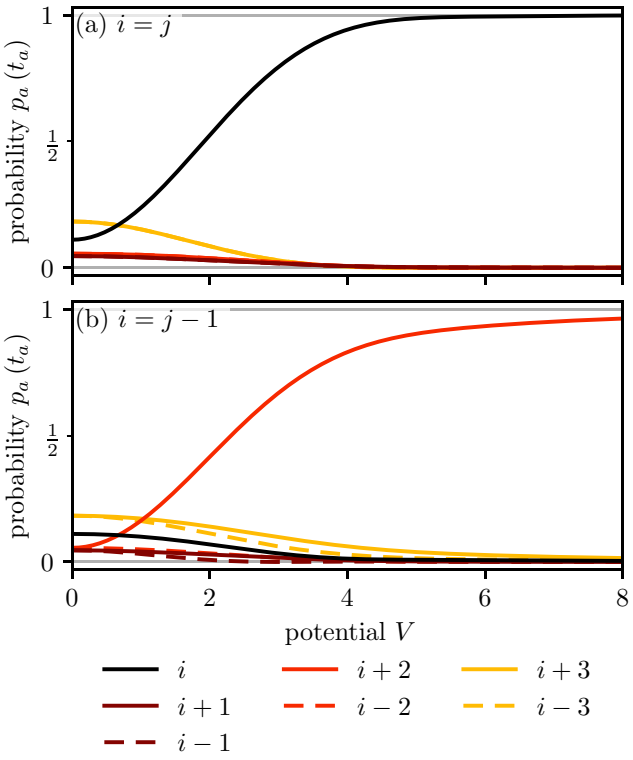

FIG. 6. Probabilities of particle a on different sites at time $t_a = \frac{\pi}{\sqrt{2}J}$ as a function of interaction V (a) for starting position $i = j$ and (b) for starting position $i = j - 1$.

The probabilities $p_a(t)$ are shown in Fig. 5. Particle a spreads symmetrically to the left and the right. This proves that, without interaction between the particles ($V = 0$), no doublons can exist and neither the stationary nor leapfrogging state occurs.

C. $V \neq 0$

For potential $V \neq 0$ but not $V \gg J$, we have to use the whole Hamiltonian (4) to describe the system.

A video in the Supplemental Material [17] shows the evolution of the probabilities for increasing interaction V going from the spreading at $V = 0$ shown in Fig. 5 to the periodic returns at $V \gg J$ shown in Fig. 2. We are mainly interested in the probabilities at the end of phase a, $t_a = \frac{\pi}{\sqrt{2}J}$. These are marked by crosses in Figs. 2 and 5. Figure 6 shows the probabilities $p(t_a)$ as a function of the interaction V. Even at relatively small interactions $V \gtrapprox 6$, the initial configuration $i = j$ remains stationary, $p_{i=j}(t_a) \approx 1$. The leapfrogging state (starting at $i = j \pm 1$) needs higher interaction strengths $V \gtrapprox 20$ to remain localized [$p_{j\mp1}(t_a) \approx 1$] while jumping from site $j \pm 1$ to site $j \mp 1$.

IV. MAPPING TO 2D

We map the two chains to a square grid, as shown in Fig. 7. The positions i and j of particles a and b are plotted along the horizontal and vertical directions, respectively.

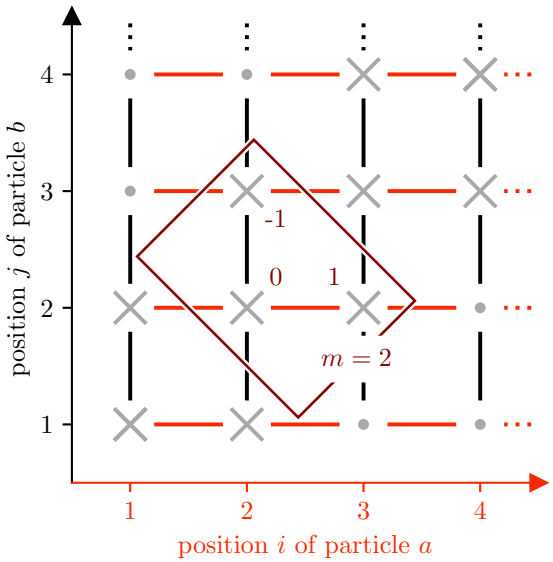

FIG. 7. Mapping of the Hamiltonian to a 2D lattice with the two particles' indices along the two axes (a-chain index s at the x axis; b-chain index t at the y axis). Red and black lines connecting sites indicate the time-dependent hoppings $J_a(t)$ and $J_b(t)$. Gray crosses indicate the combinations of lattice sites for which the interaction potential is nonvanishing. These form the reduced lattice on which the doublon dynamics take place if $V \gg J_{a,b}$. The unit cell of this three-site-wide ribbon and the new labeling $i - j = 1, 0, -1$ are indicated in brown.

A. Interacting subsystem for $V \gg J$

For strong interactions $V \gg J$, interacting states (located on sites marked by crosses in Fig. 7) are energetically separated from noninteracting states (located on sites marked by dots). If the initial state is interacting, it will remain an interacting state. Hence, for $V \gg J$, we only need to consider a subset of the 2D system, as indicated by the brown unit cell. This reduced system is quasi-1D, effectively a three-site wide ribbon. The unit cell m contains three sites, labeled by the difference of positions a and b, $i - j = 1, 0$, and -1.

1. Stationary states

A state initially located at site $(m, 0)$ will split towards sites $(m-1, -1)$ and $(m, 1)$ during the first phase, returning to $(m, 0)$ at the end of the phase, $t_a = \frac{\pi}{\sqrt{2}J}$. During the second phase, it will equivalently split towards sites $(m, -1)$ and $(m-1, 1)$ before returning to $(m, 0)$ at the end of the driving cycle $T = t_a + t_b = \frac{\sqrt{2}\pi}{J}$. The state appears to be stationary when looking stroboscopically after complete driving cycles.

2. Leapfrogging states

A state starting in site $(m, \pm 1)$ moves to site $(m \mp 1, \mp 1)$ during the first phase and then to site $(m \mp 2, \pm 1)$ during the second phase. The states move two unit cells in each cycle.

3. Reflection at the corner

The two preceding paragraphs described the evolution of states in an infinite system or the bulk of finite chains. Now, we will investigate the effects of borders. The bottom left corner comprises the complete unit cell $m = 1$. The upper right corner is a partial unit cell $m = N$, containing only the site $(N, 0)$ with sites $(N, \pm 1)$ absent.

For the Hamiltonian at the edge, one needs to consider only two sites during each driving phase (instead of three for the bulk),

$$H = \begin{pmatrix} V & J \\ J & V \end{pmatrix}. \tag{21}$$

The eigenenergies are

$$E_{1,2} = V \pm J \tag{22}$$

and the eigenstates are

$$\varphi_{1,2} = \begin{pmatrix} 1 \\ \pm 1 \end{pmatrix}. \tag{23}$$

We can now write any time-dependent state during that driving phase as

$$\psi(t) = \sum_{h=1}^{2} c_h \exp(-\mathrm{i}E_h t)\varphi_h. \tag{24}$$

Without loss of generality, we initialize the state as $\psi(0) = (1, 0)^{\mathsf{T}}$. The coefficients become $c_1 = c_2 = 1/2$, resulting in

$$\psi(t) = \exp(-\mathrm{i}Vt)\begin{pmatrix} \cos(Jt) \\ -\mathrm{i}\sin(Jt) \end{pmatrix} \tag{25}$$

and the probability

$$p(t) = |\psi(t)|^2 = \begin{pmatrix} \cos^2(Jt) \\ \sin^2(Jt) \end{pmatrix}. \tag{26}$$

Compared to the three-site Hamiltonian in Sec. III, the oscillation frequency of the two-site Hamiltonian is decreased from $\sqrt{2}J$ to J. Therefore, at the end of the phase $t_a = \frac{\pi}{\sqrt{2}J}$, the state is incompletely transferred from one site to the next,

$$p(t_a) = \begin{pmatrix} \cos^2(\pi/\sqrt{2}) \\ \sin^2(\pi/\sqrt{2}) \end{pmatrix} \approx \begin{pmatrix} 0.3669 \\ 0.6331 \end{pmatrix}. \tag{27}$$

The corner influences the stationary state starting at site $(1, 0)$. It leaks into $(1, 1)$ in the first phase, from where it continues to $(2, -1)$ in the second phase. It also leaks into $(1, -1)$ in the second phase. The stationary state sends out leapfrogging states until it vanishes. Here, we described the edge at $m = 1$, but the behavior at the other edge is equivalent.

The leapfrogging states split up when they run into an edge, similar to the stationary states.

4. Interpretation as a spin-1 system

Labeling sites in the unit cell as -1, 0, and 1 already suggests an analogy to a spin-1 system. The leapfrogging states undergo a spin-flip operation from ± 1 to ∓ 1 in each phase, accompanied by a spatial movement. The spin 0 states are unaffected by the spin-flip and remain in the same location. Experimentally, this could be achieved by moving particles with a time- and space-dependent magnetic field.

Although there is a similarity to the quantum spin Hall effect in that the transport direction depends on the spin, there

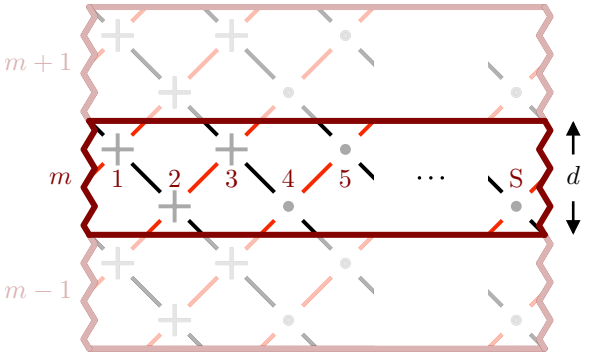

FIG. 8. Unit cell of the 45°-rotated system. The sites within it are numbered by $\alpha = 1, 2, 3, \ldots, S$ with even S. The crosses mark the diagonal sites and the dots mark the nondiagonal sites. The unit cell is infinitely repeated in the vertical direction and numbered by the index m. The height of the unit cell, d, is marked. Periodic boundaries are employed horizontally, connecting sites S and 1 within the same unit cell.

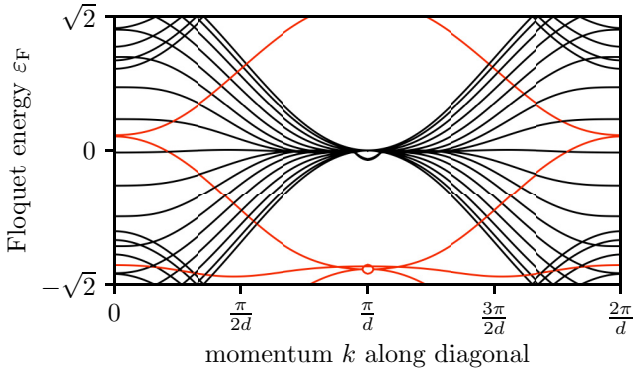

FIG. 9. Band structure of a 20-site wide strip with $V = 10$. The red bands reside on the three sites with the modified potential and the black bands on other sites.

are essential differences. While the spin remains unchanged in the spin Hall effect, it flips during transport in our model.

B. Band structure

Calculating a band structure in the one-dimensional system described in Sec. II is impossible due to the particles' interaction. After the mapping to 2D, we can calculate a band structure. To do so, we use a unit cell (shown in Fig. 8), which contains nondiagonal sites in addition to the three diagonal sites. The sites are numbered $\alpha = 1, 2, 3, \ldots, S$ with even S. The unit cell is repeated infinitely in one direction and numbered by an index m. We employ periodic boundary conditions in the other, finite direction, connecting the left and right edges of the unit cell. While this periodicity does not exist in the complete 2D system, the alternative would create diagonal edges, which do not exist in the 2D square system since there are only horizontal and vertical edges. The edge states at these diagonal edges would obfuscate the bands we are interested in.

We can write the Hamiltonians for the two phases of the driving cycle in real space as

$$\hat{H}_i = \sum_m \left(J \sum_{\alpha \text{ odd}} (\hat{h}_i(m,\alpha) + \text{H.c.}) + V \sum_{\alpha=1}^{3} |m,\alpha\rangle\langle m,\alpha| \right), \tag{28}$$

with

$$\begin{aligned} \hat{h}_a(m,\alpha) &= |m,\alpha\rangle\langle m,(\alpha-1) \mod S| \\ &\quad + |m,\alpha\rangle\langle m+1,(\alpha+1) \mod S|, \\ \hat{h}_b(m,\alpha) &= |m,\alpha\rangle\langle m,(\alpha+1) \mod S| \\ &\quad + |m,\alpha\rangle\langle m+1,(\alpha-1) \mod S|. \end{aligned} \tag{29}$$

We transform the Hamiltonians to k space by making the Bloch ansatz [18]

$$|m,\alpha\rangle = \frac{d}{2\pi} \int_{\text{BZ}} \mathrm{d}k \, \exp(-\mathrm{i}kmd) \, |k,\alpha\rangle, \tag{30}$$

where d is the lattice constant in the vertical direction in Fig. 8. We obtain

$$\hat{H}_i = \frac{d}{2\pi} \int_{\text{BZ}} \mathrm{d}k \, |k\rangle\langle k| \left(J \sum_{\alpha \text{ odd}} (\hat{h}_i(k,\alpha) + \text{H.c.}) + V \sum_{\alpha=1}^{3} |\alpha\rangle\langle\alpha| \right), \tag{31}$$

with

$$\begin{aligned} \hat{h}_a(k) &= |\alpha\rangle\langle\alpha-1| + \exp(\mathrm{i}ka)|\alpha\rangle\langle\alpha+1|, \\ \hat{h}_b(k) &= |\alpha\rangle\langle\alpha+1| + \exp(\mathrm{i}ka)|\alpha\rangle\langle\alpha-1|. \end{aligned} \tag{32}$$

The time evolution operator is

$$\hat{U}(T) = \exp\left(\frac{T}{2\mathrm{i}}\hat{H}_b\right) \exp\left(\frac{T}{2\mathrm{i}}\hat{H}_a\right). \tag{33}$$

Solving the equation

$$\hat{U}(T)\psi_F = \lambda_F \psi_F \tag{34}$$

gives the Floquet [19] eigenstates ψ_F and the Floquet energies ε_F are calculated from the eigenvalues $\lambda_F = \exp(-\mathrm{i}\varepsilon_F T)$.

The resulting band structure in Fig. 9 confirms our previous observations on the behavior of the doublons. They are located on the three sites $\alpha = 1, 2, 3$, and Floquet eigenstates where this is the case are drawn red in Fig. 9. One of these doublon bands is quite flat, corresponding to the stationary doublons. The two sloped bands correspond to doublons moving in opposite directions along the diagonal. The other bands are shown in black and form a continuum for $N \to \infty$. These bands are the diffusing states.

Depending on the potential V, some diffusing bands have nonzero energy at the center of the Brillouin zone, $\varepsilon_F(k = \frac{\pi}{d}) \neq 0$. These are edge states localized at the boundary between $\alpha = 3$ and 4 and between $\alpha = S$ and 1.

Figure 10 shows the Floquet energies $\varepsilon_F(k = \frac{\pi}{d})$ as a function of potential V. The bulk states are at constant $\varepsilon_F(k = \frac{\pi}{d}) = 0$. The energies of the doublons increase linearly with V, as indicated by the orange shadow around $\varepsilon_F = V$. The energies of the edge states show an interesting behavior: they have a tilted pole at $V \approx 3$, where they approach

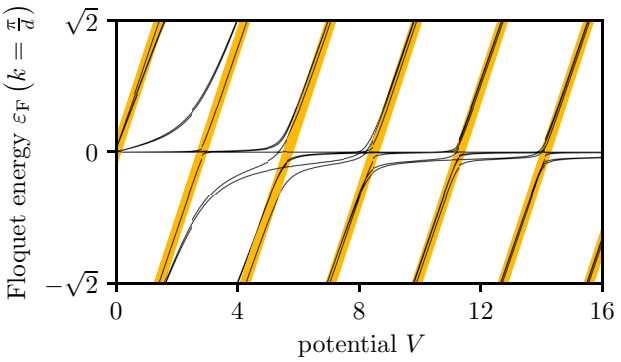

FIG. 10. Floquet energies ε_F at $k = \frac{\pi}{d}$ as a function of potential V for a 20-site wide strip. The energies of the doublons are marked by an orange shadow at $\varepsilon_F = V$.

the doublon energies. At higher potentials, they approach the energy of the bulk states, $\lim_{V\to\infty} \varepsilon_F(k = \frac{\pi}{d}) = 0$. There are crossings between the doublon and edge state energies. We have checked that they are avoided crossings by following the Floquet eigenstates.

V. POSSIBLE EXPERIMENTS AND APPLICATIONS

Ultracold atoms in optical lattices [20,21] suggest themselves for an experimental realization of our model system. The correspondence between our Floquet model and its realization in an optical lattice is readily apparent. The moving particles are the cold atoms. The sites of the lattice in the model are the sites of the optical lattice, which traps the ultracold atoms. The interaction between the two atoms can be finely tuned using Feshbach resonances [22]. Bound atom pairs have been demonstrated in periodically driven lattices [23] and for repulsive interaction in static optical lattices [24]. Modulation of the lasers achieves a change of the lattice, which enables the temporal modulation of the hoppings. Many Floquet systems have been implemented in optical lattices [25]. The use of Floquet engineering to modify the band structures of temporally periodic systems of ultracold atoms has been studied in both theory [26] and experiment [27]. Thouless pumping is one of the transport regimes that have been implemented in optical lattices [28,29]. A recent report [13] shows the implementation of interaction-induced Thouless pumping of fermionic ^{40}K atoms in an optical lattice. In their experiments, the interacting particles may be located on the same lattice sites (in contrast to our model). The periodic driving also differs. Nevertheless, the experiments suggest that our model could be implemented in optical lattices.

Another implementation would be possible in photonic waveguides [30–34]. The photonic waveguides are written into a glass block; they constitute the lattice sites. The propagation dimension of the light pulses (which are the particles) corresponds to the temporal dimension. Hopping amplitudes can be modified by changing the distance between waveguides or turned on and off by writing "blockers" between them. Directly implementing the two one-dimensional chains would be challenging to realize experimentally because of the necessary interaction between particles (light pulses) on neighboring sites. The two-dimensional square lattice (after mapping to two dimensions as described in Sec. IV) is more suitable for experimental realization. The different potentials of its lattice sites are implemented as different refractive indices of the respective waveguides. Solitons and edge states have been achieved experimentally [35–39] and also Thouless pumping [40].

VI. CONCLUSION AND SIGNIFICANCE

We investigated two particles on two linear chains in a periodic driving scheme and showed how their interaction influences their temporal evolution. Without interaction, both particles diffuse. With sufficiently strong interaction, they can form a stationary bound state that remains localized without diffusing. They can also form nonstationary, nondiffusing states, which propagate in a leapfrogging manner. These states are energetically separated from all others, as seen in the Floquet band structure. The relative position of the two particles in the starting configuration determines their behavior.

A possible extension of the system would be going from linear chains to two-dimensional grids on which the particles move. The added dimension would enable vertical and diagonal movement of the particles in addition to the horizontal one on the chains.

Our relatively simple model system harbors spatially localized states, which are only stable due to interaction. We think of it as a building block, a part of a toolbox for synthetic quantum systems. We envision its potential use for transporting two particles together for some distance and then splitting them up again at the target location. This could be useful for information transfer in quantum computing. Entangling particles (e.g., their spins) before their transport would also be possible.

Observing the evolution of the two particles and the lifetime of their bound state could allow us to measure the strength of the interaction between them. Since the direction of transport depends on the exact initial locations of the two particles, the system could be used as a switch in quantum computing, relaying signals to the left or to the right depending on the input.

ACKNOWLEDGMENTS

This research and publication were supported by the Studienstiftung des deutschen Volkes (German Academic Scholarship Foundation) and the Deutsche Forschungsgemeinschaft (DFG, German Research Foundation), SFB 1477 "Light-Matter Interactions at Interfaces," Project No. 441234705.

[1] E. H. Hall, On a new action of the magnet on electric currents, Am. J. Math. **2**, 287 (1879).

[2] M. I. Dyakonov and V. I. Perel, Current-induced spin orientation of electrons in semiconductors, Phys. Lett. A **35**, 459 (1971).

[3] D. R. Hofstadter, Energy levels and wave functions of Bloch electrons in rational and irrational magnetic fields, Phys. Rev. B **14**, 2239 (1976).

[4] K. von Klitzing, T. Chakraborty, P. Kim, V. Madhavan, X. Dai, J. McIver, Y. Tokura, L. Savary, D. Smirnova, A. M. Rey, C. Felser, J. Gooth, and X. Qi, 40 years of the quantum Hall effect, Nat. Rev. Phys. **2**, 397 (2020).

[5] P. Reimann, Brownian motors: noisy transport far from equilibrium, Phys. Rep. **361**, 57 (2002).

[6] P. Hänggi and F. Marchesoni, Artificial Brownian motors: Controlling transport on the nanoscale, Rev. Mod. Phys. **81**, 387 (2009).

[7] S. Yukawa, M. Kikuchi, G. Tatara, and H. Matsukawa, Quantum Ratchets, J. Phys. Soc. Jpn. **66**, 2953 (1997).

[8] P. Reimann, M. Grifoni, and P. Hänggi, Quantum ratchets, Phys. Rev. Lett. **79**, 10 (1997).

[9] N. Dupont, L. Gabardos, F. Arrouas, N. Ombredane, J. Billy, B. Peaudecerf, and D. Guéry-Odelin, Hamiltonian ratchet for matter-wave transport, Phys. Rev. Lett. **131**, 133401 (2023).

[10] D. J. Thouless, Quantization of particle transport, Phys. Rev. B **27**, 6083 (1983).

[11] R. Citro and M. Aidelsburger, Thouless pumping and topology, Nat. Rev. Phys. **5**, 87 (2023).

[12] A.-S. Walter, Z. Zhu, M. Gächter, J. Minguzzi, S. Roschinski, K. Sandholzer, K. Viebahn, and T. Esslinger, Quantization and its breakdown in a Hubbard-Thouless pump, Nat. Phys. **19**, 1471 (2023).

[13] K. Viebahn, A.-S. Walter, E. Bertok, Z. Zhu, M. Gächter, A. A. Aligia, F. Heidrich-Meisner, and T. Esslinger (unpublished).

[14] L. Lin, Y. Ke, and C. Lee, Interaction-induced topological bound states and Thouless pumping in a one-dimensional optical lattice, Phys. Rev. A **101**, 023620 (2020).

[15] B. N. Narozhny and A. Levchenko, Coulomb drag, Rev. Mod. Phys. **88**, 025003 (2016).

[16] A. Slavík and P. Stehlík, Explicit solutions to dynamic diffusion-type equations and their time integrals, Appl. Math. Comput. **234**, 486 (2014).

[17] See Supplemental Material at http://link.aps.org/supplemental/10.1103/PhysRevResearch.6.023032 for a video of the evolution of the probabilities for increasing interaction V going from the spreading at $V = 0$ (Fig. 5) to the periodic returns at $V \gg J$ (Fig. 2).

[18] F. Bloch, Über die Quantenmechanik der Elektronen in Kristallgittern, Z. Phys. **52**, 555 (1929).

[19] G. Floquet, Sur les équations différentielles linéaires à coefficients périodiques, Ann. Sci. École Norm. Sup. **12**, 47 (1883).

[20] R. Grimm, M. Weidemüller, and Y. B. Ovchinnikov, in *Optical Dipole Traps for Neutral Atoms*, edited by B. Bederson and H. Walther, Advances In Atomic, Molecular, and Optical Physics Vol. 42 (Academic Press, New York, 2000), pp. 95–170.

[21] I. Bloch, Ultracold quantum gases in optical lattices, Nat. Phys. **1**, 23 (2005).

[22] C. Chin, R. Grimm, P. Julienne, and E. Tiesinga, Feshbach resonances in ultracold gases, Rev. Mod. Phys. **82**, 1225 (2010).

[23] H.-H. Zhong, Z. Zhou, B. Zhu, Y.-G. Ke, and C.-H. Lee, Floquet bound states in a driven two-particle bose-hubbard model with an impurity, Chin. Phys. Lett. **34**, 070304 (2017).

[24] K. Winkler, G. Thalhammer, F. Lang, R. Grimm, J. Hecker Denschlag, A. J. Daley, A. Kantian, H. P. Büchler, and P. Zoller, Repulsively bound atom pairs in an optical lattice, Nature (London) **441**, 853 (2006).

[25] C. Weitenberg and J. Simonet, Tailoring quantum gases by Floquet engineering, Nat. Phys. **17**, 1342 (2021).

[26] M. Holthaus, Floquet engineering with quasienergy bands of periodically driven optical lattices, J. Phys. B: At. Mol., Opt. Phys. **49**, 013001 (2016).

[27] C. J. Fujiwara, K. Singh, Z. A. Geiger, R. Senaratne, S. V. Rajagopal, M. Lipatov, and D. M. Weld, Transport in floquet-bloch bands, Phys. Rev. Lett. **122**, 010402 (2019).

[28] S. Nakajima, T. Tomita, S. Taie, T. Ichinose, H. Ozawa, L. Wang, M. Troyer, and Y. Takahashi, Topological Thouless pumping of ultracold fermions, Nat. Phys. **12**, 296 (2016).

[29] M. Lohse, C. Schweizer, O. Zilberberg, M. Aidelsburger, and I. Bloch, A Thouless quantum pump with ultracold bosonic atoms in an optical superlattice, Nat. Phys. **12**, 350 (2016).

[30] K. Itoh, W. Watanabe, S. Nolte, and C. B. Schaffer, Ultrafast processes for bulk modification of transparent materials, MRS Bull. **31**, 620 (2006).

[31] A. Szameit and S. Nolte, Discrete optics in femtosecond-laser-written photonic structures, J. Phys. B: At. Mol. Opt. Phys. **43**, 163001 (2010).

[32] M. C. Rechtsman, J. M. Zeuner, Y. Plotnik, Y. Lumer, D. Podolsky, F. Dreisow, S. Nolte, M. Segev, and A. Szameit, Photonic Floquet topological insulators, Nature (London) **496**, 196 (2013).

[33] T. Ozawa, H. M. Price, A. Amo, N. Goldman, M. Hafezi, L. Lu, M. C. Rechtsman, D. Schuster, J. Simon, O. Zilberberg, and I. Carusotto, Topological photonics, Rev. Mod. Phys. **91**, 015006 (2019).

[34] H. Price, Y. Chong, A. Khanikaev, H. Schomerus, L. J. Maczewsky, M. Kremer, M. Heinrich, A. Szameit, O. Zilberberg, Y. Yang, B. Zhang, A. Alù, R. Thomale, I. Carusotto, P. St-Jean, A. Amo, A. Dutt, L. Yuan, S. Fan, X. Yin, C. Peng, T. Ozawa, and A. Blanco-Redondo, Roadmap on topological photonics, J. Phys. Photon. **4**, 032501 (2022).

[35] Y. Lumer, Y. Plotnik, M. C. Rechtsman, and M. Segev, Self-localized states in photonic topological insulators, Phys. Rev. Lett. **111**, 243905 (2013).

[36] M. J. Ablowitz, C. W. Curtis, and Y.-P. Ma, Linear and nonlinear traveling edge waves in optical honeycomb lattices, Phys. Rev. A **90**, 023813 (2014).

[37] D. Leykam and Y. D. Chong, Edge solitons in nonlinear-photonic topological insulators, Phys. Rev. Lett. **117**, 143901 (2016).

[38] S. Mukherjee and M. C. Rechtsman, Observation of Floquet solitons in a topological bandgap, Science **368**, 856 (2020).

[39] S. Mukherjee and M. C. Rechtsman, Observation of unidirectional solitonlike edge states in nonlinear floquet topological insulators, Phys. Rev. X **11**, 041057 (2021).

[40] M. Jürgensen, S. Mukherjee, C. Jörg, and M. C. Rechtsman, Quantized fractional Thouless pumping of solitons, Nat. Phys. **19**, 420 (2023).

8. Steering edge currents through a Floquet topological insulator

H. Drüeke, M. Meschede, and D. Bauer: "Steering edge currents through a Floquet topological insulator" *Physical Review Research* 5.2 (2023), 023056 DOI: 10.1103/PhysRevResearch.5.023056

Steering edge currents through a Floquet topological insulator

Helena Drüeke,* Marcus Meschede,† and Dieter Bauer‡
Institute of Physics, University of Rostock, 18051 Rostock, Germany

(Received 19 April 2022; revised 5 January 2023; accepted 9 February 2023; published 25 April 2023)

Periodic driving may cause topologically protected, chiral transport along edges of a two-dimensional (2D) lattice that, without driving, would be topologically trivial. We study what happens if one adds a different on-site potential along the diagonal of such a 2D grid. In addition to the usual bulk and edge states, the system then also exhibits doublon states, analogous to two interacting particles in one dimension. A particle initially located at an edge propagates along the system's boundary. Its wave function splits when it hits the diagonal and continues propagating simultaneously along the edge and the diagonal. The strength of the diagonal potential determines the ratio between both parts. We show that for specific values of the diagonal potential, hopping onto the diagonal is prohibited so that the system effectively separates into two triangular lattices. For other values of the diagonal potential, we find a temporal delay between the two contributions traveling around and through the system. This behavior could enable the steering of topologically protected transport of light along the edges and through the bulk of laser-inscribed photonic waveguide arrays.

DOI: 10.1103/PhysRevResearch.5.023056

I. INTRODUCTION

Topological insulators [1,2] exhibit an insulating bulk and conducting edges. Floquet topological insulators [3–5] are synthetic systems. Periodic driving causes their behavior as topological insulators. Therefore, time becomes an additional system dimension, and modifications of the driving scheme are a practical parameter for tuning Floquet topological insulators. They are realized experimentally with cold atoms in optical lattices [6–8], with photonic platforms [9–14], or even for acoustic waves [15,16]. Theoretically, they are studied in one dimension (1D) [17,18], two dimensions (2D) [19,20], and systematized in a periodic table [21]. For a recent theoretical review, see [22].

Rudner *et al.* [23] proposed a Floquet topological insulator on a bipartite square lattice. They also derived a topological invariant for that system. In our paper, we investigate a modified version of Rudner's system. Instead of global, alternating on-site potentials on the two sublattices, we introduce an on-site potential along the diagonal of the lattice. We examine how the diagonal potential can cut the system in half, fully or partially. Without it, a topologically protected edge current can flow along the system's outer edge. The addition of a diagonal potential introduces an "inner" edge. Depending on the exact choice of parameters, a portion or the whole edge state may flow along this inner edge instead of the outer edge.

The diagonal potential leads to some eigenstates located (almost) exclusively along the diagonal. We relate these eigenstates to doublon physics. There, two interacting particles on, for example, a one-dimensional [24–27] or two-dimensional [28] lattice may form a bound pair, a so-called doublon state. Doublons are stable due to their energetic separation from other states or because of topology, characterized by a differing topological invariant. They can arise from repulsively as well as from attractively interacting particle pairs.

In order to prove that our system is topologically nontrivial, we need a topological invariant. The usual Chern number is insufficient to determine the existence of chiral edge states in Floquet systems. The Chern number of an energy band gives the difference between the numbers of chiral edge modes entering it from above and below. In a static system, the energy spectrum is bound from below, i.e., no edge modes can exist below the lowest-energy band. The number of edge states in any band gap equals the sum of the Chern numbers of all bands below it. However, in Floquet systems, due to their temporal periodicity, the energy becomes a quasienergy, which is also periodic. Edge modes can loop around from below the lowest to above the highest band. This allows chiral edge states to exist in a Floquet system in which all bands have Chern number 0. Rudner *et al.* [23] derived a winding number as a topological invariant for Floquet systems. In contrast to the Chern number, which only depends on projectors onto Floquet bands, the winding number considers the whole time evolution throughout the driving cycle.

This paper is structured as follows: Sec. II contains a description of the system under study, Sec. III its Floquet eigenstates, Sec. IV its band structure, and Sec. V the temporal evolution of states. We give a conclusion in Sec. VI. The Appendices contain derivations of the hopping probability (Appendix A) and the topological invariant (Appendix B), as well as the algorithm for tracking states through (avoided) crossings (Appendix C).

*helena.drueeke@uni-rostock.de
†marcus.meschede@uni-rostock.de
‡dieter.bauer@uni-rostock.de

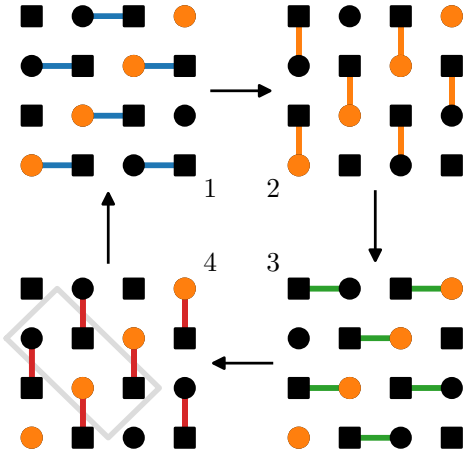

FIG. 1. Sketch of the driving scheme for a 4×4 system. The dots (squares) indicate the lattice sites on sublattice A (B). The orange dots are the lattice sites on the diagonal (with a modified on-site potential). The four panels show the different hoppings in the four phases of the driving cycle as (blue, orange, green, and red) connecting lines. The gray rectangle indicates the unit cell used for calculating the band structure in Sec. IV.

II. SYSTEM

We investigate an $N \times N$ square-lattice system. The lattice sites $s_{i,j}$ are numbered by horizontal and vertical indices $i, j \in \{1, 2, \ldots, N\}$. Index i increases from left to right, and j increases from bottom to top. Sublattice A contains all sites with even sum $i + j$, and sublattice B those with odd $i + j$. The periodic driving scheme of this Floquet system is sketched in Fig. 1. We modify the potentials of the sites $s_{i,i}$ along the diagonal (as shown in Fig. 1), which we set to V_{dia}. All other on-site potentials are 0.

A. Hamiltonians

We will now introduce a mathematical description of the system and its parameters. The hopping amplitudes and potentials are described by the stepwise constant Hamiltonian

$$\hat{H}(t) = \begin{cases} \hat{H}_1, & 0 < t \leqslant T/4 \\ \hat{H}_2, & T/4 < t \leqslant T/2 \\ \hat{H}_3, & T/2 < t \leqslant 3T/4 \\ \hat{H}_4, & 3T/4 < t \leqslant T \end{cases} \tag{1}$$

with

$$\hat{H}_k = \hat{H}_{\mathrm{dia}} + J \sum_{\substack{i,j=1 \\ i+j \text{ even}}}^{N} \hat{h}_k(i,j) + \mathrm{H.c.}, \tag{2}$$

$$\hat{H}_{\mathrm{dia}} = V_{\mathrm{dia}} \sum_{i=1}^{N} |i,i\rangle\langle i,i|, \tag{3}$$

$$\hat{h}_1(i,j) = |i,j\rangle\langle i+1,j|, \quad \hat{h}_2(i,j) = |i,j\rangle\langle i,j+1|,$$
$$\hat{h}_3(i,j) = |i,j\rangle\langle i-1,j|, \quad \hat{h}_4(i,j) = |i,j\rangle\langle i,j-1|, \tag{4}$$

period T, and hopping amplitude J.

B. Hopping probabilities

In each of the four phases of the driving scheme, each lattice site connects to (at most) one neighboring lattice site. Therefore, the Hamiltonian of the whole system breaks down into several two-state Hamiltonians, each describing the interaction between connected sites. In Appendix A, we derive the hopping probability between two connected sites

$$p(t,V) = \frac{4J^2}{V^2+4J^2} \sin^2\left(\frac{\sqrt{V^2+4J^2}}{2}t\right) \tag{5}$$

as a function of the potential difference V between the sites and the duration t of the respective driving phase. Without a potential (i.e., between the off-diagonal sites), we want the particles to hop completely during each of the four phases, $p\left(\frac{T}{4}, 0\right) = \sin^2\left(\frac{JT}{4}\right) := 1$. We set $J = 1$ and choose $T = \frac{2\pi}{J} = 2\pi$, such that in the absence of on-site potentials, the hopping probability between two connected sites during each phase is exactly 1. With on-site potential V_{dia} along the diagonal, the hopping probability between connected diagonal and off-diagonal sites (and vice versa) becomes

$$p(V_{\mathrm{dia}}) = p\left(\frac{T}{4}, V_{\mathrm{dia}}\right) = \frac{4}{V_{\mathrm{dia}}^2+4} \sin^2\left(\frac{\pi}{4}\sqrt{V_{\mathrm{dia}}^2+4}\right), \tag{6}$$

shown in Fig. 6(a). The prefactor $4/\left(V_{\mathrm{dia}}^2+4\right)$ leads to a decrease in the hopping probability at higher diagonal potentials. As expected, the particle cannot overcome the energetic separation between off-diagonal and diagonal sites at high diagonal potentials. But the probability for hopping onto the diagonal is also vanishing at finite diagonal potentials

$$V_{\mathrm{dia},0}^{(n)} = \pm 2\sqrt{4n^2-1} \tag{7}$$

for $n \in \mathbb{N}$, determined by the zeros of the $\sin^2$ term of (6). At these specific potentials, the duration of each phase corresponds to one complete Rabi period. Therefore, at $V_{\mathrm{dia},0}^{(n)}$, a particle moves from its starting site to the connected neighboring site and back n times, returning to the starting site at the end of the phase. The first zero is at a remarkably low diagonal potential $V_{\mathrm{dia},0}^{(1)} = 2\sqrt{3}$.

C. Time evolution operator

The time evolution operator (in units where $\hbar = 1$)

$$\hat{U}(t) = \mathcal{T} \exp\left(-i \int_0^t dt' \, \hat{H}(t')\right), \tag{8}$$

where $\mathcal{T}$ is the time-ordering operator, describes the system's temporal evolution. For a complete driving cycle consisting of the four discrete phases ($t = T$), the time evolution operator reads

$$\hat{U}(T) = e^{c\hat{H}_4} e^{c\hat{H}_3} e^{c\hat{H}_2} e^{c\hat{H}_1}, \tag{9}$$

with $c = \frac{T}{4i}$. Solving the equation

$$\hat{U}(T)\psi_{\mathrm{F}} = \lambda_{\mathrm{F}}\psi_{\mathrm{F}} \tag{10}$$

gives the Floquet eigenstates ψ_{F}, and the Floquet energies ε_{F} are calculated from the eigenvalues $\lambda_{\mathrm{F}} = \exp(-i\varepsilon_{\mathrm{F}}T)$. By following the states (not just their energies) as a function of

V_{dia}, we can distinguish state crossings from avoided crossings. Appendix C explains the details of the state-tracking algorithm.

III. FLOQUET STATES

Without a diagonal potential, the $N \times N$ system contains $(N-1)^2$ bulk states at Floquet energy $\varepsilon_{\mathrm{F}} = 0$ and $2N-1$ edge states at equally spaced Floquet energies $\varepsilon_{\mathrm{F}} = m/(2N-1)$, $m \in \mathbb{Z}$, $|m| < N$. At nonvanishing diagonal potential, some of the bulk states superpose to form doublon states, resulting in $(N-3)(N-2)$ remaining bulk states, $N-1$ primary doublon states, and $2(N-2)$ secondary doublon states. Particles in a primary doublon state hop on and off the modified diagonal twice during a complete driving cycle. They hop on and off the diagonal once in a secondary doublon state.

We call these diagonal states *doublons*, in analogy to doublons in one-dimensional, interacting systems [24–28]. A system of two interacting particles on a one-dimensional lattice (e.g., a Su-Schrieffer-Heeger chain [29]) can be mapped to a single particle on a two-dimensional lattice. The x and y coordinates of the 2D particle correspond to the position of the first and the second particle on the 1D chain, respectively. Movements of the first (second) particle then amount to horizontal (vertical) hoppings. Their interaction $V(|x-y|)$ is captured by an on-site potential in 2D. A local interaction in 1D, through which the particles only affect each other if they are on the same site, corresponds to the diagonal potential along $x = y$ used in this study. Longer-range interactions would require nonvanishing on-site potentials on not only the main but also the secondary, tertiary, etc., diagonal, depending on the maximum interaction distance. However, in our Floquet system, the mapping between the two-particle-1D and the one-particle-2D case is more involved and not that intuitive because the simple driving scheme in 2D corresponds to intricate, time-dependent, nonlocal interactions of two particles in 1D.

Figure 2 shows the Floquet energies ε_{F} as a function of the diagonal potential V_{dia}. The four different types of states are indicated in Fig. 2(a): The diagonal potential does not influence the bulk states' energies because the bulk states remain located on sites whose potentials are zero in each step of the driving cycle. The edge states cross the diagonal in the system's bottom-left and top-right corners. Therefore, their energies increase with increasing diagonal potential. The doublons cross the diagonal as well, which leads to increasing Floquet energies. The primary doublons' energies increase faster because they cross the diagonal twice during a driving cycle, unlike the secondary doublons, which only cross it once.

At higher diagonal potentials $V_{\mathrm{dia}} \gtrsim 2$ [shown in Fig. 2(b)], three types of states exist: The bulk states' energies remain zero, while the edge states' energies increase slightly with diagonal potential. For the Floquet states located on the diagonal of the system, we find $\varepsilon_F \approx V_{\mathrm{dia}}$. All states form pairs with similar energies. These pairs degenerate to identical energies at the zeros of the hopping probability, and we find superpositions of the states confined to either the top-left or bottom-right triangular half of the system.

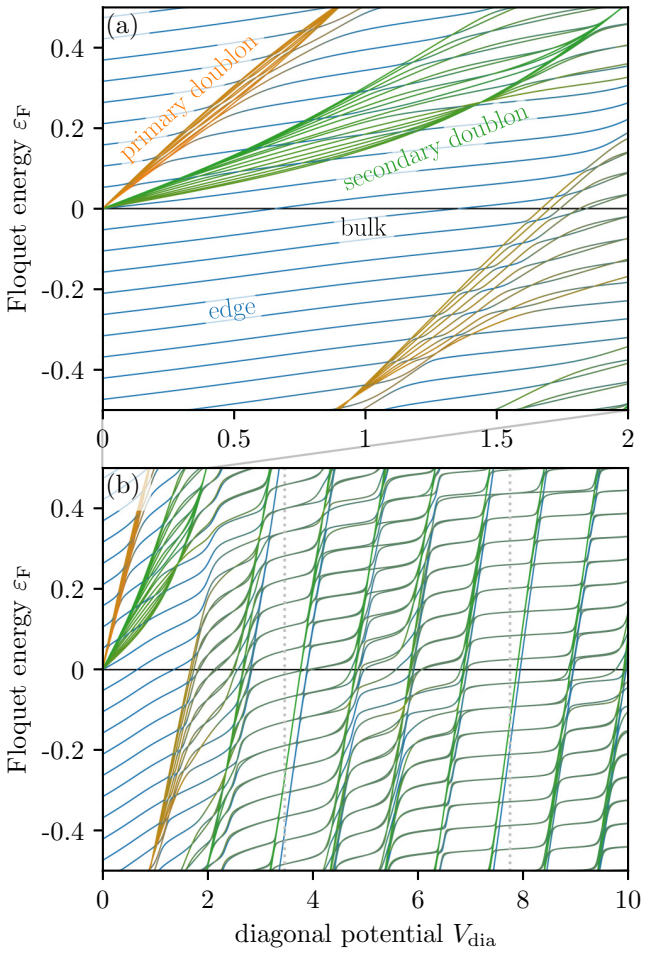

FIG. 2. Floquet energies ε_{F} for the 10×10 system as a function of the diagonal potential V_{dia}. (a) The line colors indicate the types of states: bulk states (black), edge states (blue), primary doublon states (orange), and secondary doublon states (green). (b) The dotted gray lines indicate the zeros $V^{(1)}_{\mathrm{dia},0}$ and $V^{(2)}_{\mathrm{dia},0}$ of the hopping probability $p(V_{\mathrm{dia}})$.

IV. BAND STRUCTURE

In order to calculate a band structure, we must have a system that is infinitely extended in at least one direction. We turn our system by 45° and obtain an infinite strip with the former diagonal in the middle. The narrowest viable strip is four sites wide, as shown in Fig. 3. Wider strips would only host more bulk states with identical energies. The unit cell is repeated infinitely in the vertical direction and numbered by an index m. The sites are numbered $\alpha = 1, 2, 3, 4$.

We can write the Hamiltonians for the four phases in real space as

$$\hat{H}_i = V|m,3\rangle\langle m,3| + \left(J\sum_m \hat{h}_i(m) + \mathrm{H.c.}\right) \qquad (11)$$

with

$$\hat{h}_1(m) = |m,1\rangle\langle m,2| + |m,3\rangle\langle m,4|,$$

$$\hat{h}_2(m) = |m,3\rangle\langle m,2| + |m,1\rangle\langle m,4|,$$

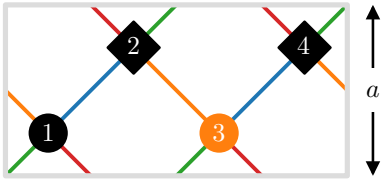

FIG. 3. Unit cell of the 45°-rotated system as outlined in light gray in panel 4 of Fig. 1. The system is infinitely extended in the vertical direction. The height of the unit cell, a, is marked. Periodic boundaries are employed horizontally. The orange circle (3) marks the diagonal. The hoppings of all four phases are shown in the same colors as in Fig. 1.

$$\hat{h}_3(m) = |m+1,3\rangle\langle m,2| + |m+1,1\rangle\langle m,4|,$$
$$\hat{h}_4(m) = |m+1,1\rangle\langle m,2| + |m+1,3\rangle\langle m,4|. \quad (12)$$

We transform the Hamiltonians to k space by making the Bloch ansatz

$$|m,\alpha\rangle = \frac{a}{2\pi}\int_{\mathrm{BZ}} dk\, \exp(-ikma)\,|k,\alpha\rangle, \quad (13)$$

where a is the height of the unit cell (i.e., the distance from site 1 in cell m to site 1 in cell $m+1$). We can identify

$$\hat{H}_i = \frac{a}{2\pi}\int_{\mathrm{BZ}} dk|k\rangle\langle k|[V|3\rangle\langle 3| + J(\hat{h}_i(k) + \mathrm{H.c.})] \quad (14)$$

with

$$\hat{h}_1(k) = |1\rangle\langle 2| + |3\rangle\langle 4|,$$
$$\hat{h}_2(k) = |3\rangle\langle 2| + |1\rangle\langle 4|,$$
$$\hat{h}_3(k) = \exp(ika)(|3\rangle\langle 2| + |1\rangle\langle 4|),$$
$$\hat{h}_4(k) = \exp(ika)(|1\rangle\langle 2| + |3\rangle\langle 4|). \quad (15)$$

We used these Hamiltonians to calculate the band structures shown in Fig. 4. At diagonal potentials $V_{\mathrm{dia}} = V^{(n)}_{\mathrm{dia},0}$ [Fig. 4(a)], the band structure consists of four separate bands: The flat band at $\varepsilon_{\mathrm{F}} = 0$ (shown in black) consists of stationary bulk states, and the other flat band (orange) consists of primary diagonal states, which are also stationary. The two diagonal bands (green and blue) consist of secondary diagonal states. Their slope indicates the movement of these states along the diagonal. The bulk band remains unchanged at other diagonal potentials [Fig. 4(b)]. The three other bands, however, connect as their crossings turn into avoided crossings.

We employed periodic boundary conditions on the left and right edges of the unit cell when calculating the band structures. The full system is not periodic in this direction. It only contains a single modified diagonal, not a periodically repeated one. For the calculation of the band structure, however, this periodicity (the connection between sites 1 and 4 in Fig. 3) is necessary. Without it, the left and right edges of the unit cell would become edges of the system, hosting edge states (two additional diagonal bands). Such edges, which would lie in diagonal direction in the nonrotated system, do not exist in the full (square) system. It only contains horizontal and vertical edges, whose edge states move with a different velocity than the diagonal ones. These edge states would also result in diagonal bands but with a different slope. The band structures

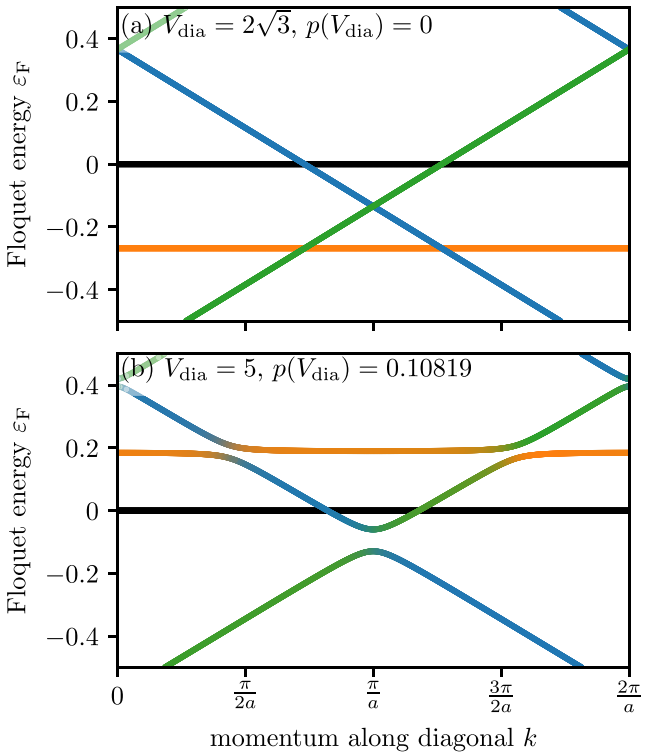

FIG. 4. Band structure of a four-site-wide diagonal strip at different diagonal potentials V_{dia}. The bulk states (shown in black) form a flat band at $\varepsilon_{\mathrm{F}} = 0$, irrespective of the diagonal potential. (a) $V_{\mathrm{dia}} = 2\sqrt{3}$, i.e., $p(V_{\mathrm{dia}}) = 0$; the primary diagonal states form a flat band (orange) and the secondary diagonal states form diagonal bands (green and blue). Transferring between bands is impossible. (b) $V_{\mathrm{dia}} = 5$, i.e., $p(V_{\mathrm{dia}}) = 0.10819$: the crossings between (primary and secondary) diagonal states become avoided crossings.

in Fig. 4 do not contain these bands. They are band structures of the bulk, showing stationary states and those moving along the diagonal. A topological invariant for the system is derived in Appendix B.

V. TEMPORAL EVOLUTION

By definition, the Floquet states ψ_{F} remain unchanged after a complete cycle's evolution, except for a phase factor. However, for an intuitive understanding of the driven quantum dynamics, it is instructive (and closer to experimental realizations on photonic platforms) to study the temporal evolution of (initially) localized states $\varphi(\mathbf{r}, t)$. We initialize these as one at a single site $\mathbf{r}_{\mathrm{initial}}$ and zero everywhere else. Specifically, in Fig. 5, we look at a state starting on the left edge of the 10×10 system.

Without a diagonal potential and therefore perfect hopping $p(0) = 1$ between diagonal and off-diagonal sites [Fig. 5(b)], the state remains localized and moves counterclockwise along the edges of the system, returning to its origin after $2N - 1$ complete driving cycles. The state cannot cross the diagonal at the zeros of the hopping probability $p(V_{\mathrm{dia}}) = 0$. Because it started above the diagonal, it will remain in the upper-left triangular half of the system, moving along the edge of that triangle and returning to its origin after $2N - 3$

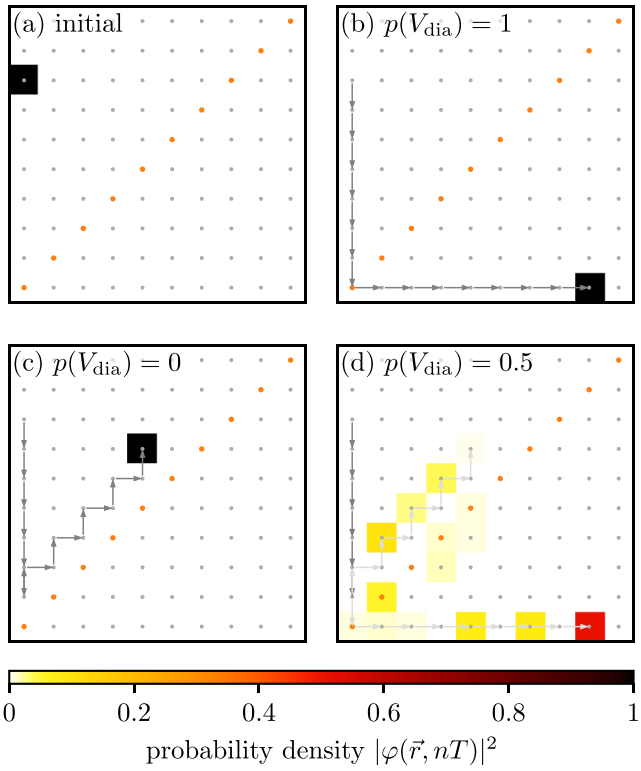

FIG. 5. Temporal evolution of a localized edge state in the 10×10 system. The dots mark the locations of the sites. The orange ones are those on the diagonal. (a) Starting configuration ($n = 0$). (b)–(d) State after evolution for $n = 8$ complete cycles. The arrows sketch the path of the state during its evolution. (b) $V_{\mathrm{dia}} = 0$, i.e., $p(V_{\mathrm{dia}}) = 1$; the state moves around the whole system and will return at its initial site after $2N - 1 = 19$ cycles. (c) $V_{\mathrm{dia}} = 2\sqrt{3}$, i.e., $p(V_{\mathrm{dia}}) = 0$; the state moves around the upper left triangle because the diagonal is insurmountable and will return after $2N - 3 = 17$ cycles. (d) $V_{\mathrm{dia}} = 1.597\,37$, i.e. $p(V_{\mathrm{dia}}) = 0.5$; the state splits. The Supplemental Material [30] contains animations of these three cases for a 20×20 system.

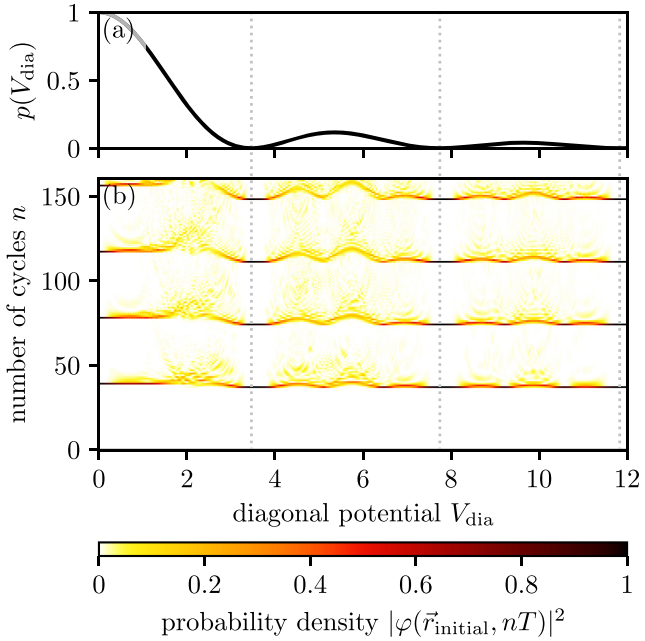

FIG. 6. (a) Hopping probability $p(V_{\mathrm{dia}})$ as a function of diagonal potential. (b) Probability density $|\varphi(\mathbf{r}_{\mathrm{initial}}, nT)|^2$ ($n \in \mathbb{N}$) at the starting location $\mathbf{r}_{\mathrm{initial}}$ for an edge state in a 20×20 system, as a function of time and diagonal potential. The dotted gray lines indicate the zeros of $p(V_{\mathrm{dia}})$ in (a), which coincide with the perfect earlier returns in (b).

cycles [Fig. 5(c)]. For all other potentials, which result in $0 < p(V_{\mathrm{dia}}) < 1$, the state splits at the bottom-left corner of the system and delocalizes [Fig. 5(d)].

Most $[(N-3)(N-2)]$ of the $(N-1)^2$ bulk states do not interact with any sites on the diagonal, and therefore their evolution is unaffected by V_{dia}. The other $3N - 5$ bulk states, however, interact with the diagonal at least once and are split up for $0 < p(V_{\mathrm{dia}}) < 1$. For $p(V_{\mathrm{dia}}) = 0$, $2N - 3$ bulk states turn into edge states on the upper-left and lower-right triangles. The $N - 2$ bulk and two edge states that start on the diagonal remain stationary for $p(V_{\mathrm{dia}}) = 0$.

While snapshots of the temporal evolution allow us to understand the general behavior, it is inconvenient to investigate them systematically for varying potentials. Therefore, we record the probability density $|\varphi(\mathbf{r}_{\mathrm{initial}}, nT)|^2$ ($n \in \mathbb{N}$) at the starting location $\mathbf{r}_{\mathrm{initial}}$ after each driving cycle. Because we initialize all states perfectly localized, $|\varphi(\mathbf{r}_{\mathrm{initial}}, 0)|^2 = 1$ for all states. The bulk states return to their starting location after each cycle, and therefore $|\varphi_{\mathrm{bulk}}(\mathbf{r}_{\mathrm{initial}}, nT)|^2 = 1\ \forall n \in \mathbb{N}$.

As shown in Fig. 6, without a diagonal potential, an edge state returns at its origin after $2N - 1$ cycles. At the zeros of $p(V_{\mathrm{dia}})$ (7), the system is equivalent to one without sites on the diagonal. The edge states remain confined to the upper-left or bottom-right triangle, which they started in, and return to their origins after $2N - 3$ cycles. Other on-site potentials V_{dia} lead to a splitting of the state. Part of the wave function travels through the diagonal and along the square's edge, arriving after $2N - 1$ cycles, while another part travels around the triangle and arrives after $2N - 3$ cycles. Due to the imperfect transfer, there are not two discrete arrival peaks. Instead, the peaks disperse and interfere.

VI. CONCLUSION AND OUTLOOK

We characterized a Floquet topological insulator on a square lattice with varying diagonal on-site potential. The addition of a diagonal potential causes the appearance of additional bands. We call these states doublons, in analogy to doublons in systems of one-dimensional, interacting particles. There are stationary doublons and those which perform directional motion along the diagonal.

We showed how fine-tuning the diagonal potential cuts the Floquet topological insulator into halves. While a small diagonal potential is sufficient to disconnect the system completely, surprisingly, increasing the diagonal potential further will partially reconnect the system. This partial cutting allows switching between the propagation along the edge and the diagonal. In a photonic setting with laser-inscribed waveguides, intense laser light and nonlinearities can modify the

diagonal potential (i.e., refractive index) [11,12,31]. In that way, one may switch topologically protected light currents by light, rendering a photonic platform programmable instead of "hardwired."

ACKNOWLEDGMENTS

This research and publication were supported by the Studienstiftung des deutschen Volkes (German Academic Scholarship Foundation) and the Deutsche Forschungsgemeinschaft (DFG, German Research Foundation), SFB 1477 "Light-Matter Interactions at Interfaces," Project No. 441234705.

APPENDIX A: DERIVATION OF HOPPING PROBABILITY

The 2×2 Hamiltonian

$$\hat{H} = \begin{pmatrix} V & J \\ J & 0 \end{pmatrix} \tag{A1}$$

describes the hopping between two sites with potential difference V and hopping element J. Its eigenstates

$$\varphi_{1,2} = \begin{pmatrix} V \pm \sqrt{V^2 + 4J^2} \\ 2J \end{pmatrix} \tag{A2}$$

and corresponding eigenenergies

$$\varepsilon_{1,2} = \tfrac{1}{2}\left(V \pm \sqrt{V^2 + 4J^2}\right) \tag{A3}$$

satisfy the time-independent Schrödinger equation

$$\hat{H}\varphi_{1,2} = \varepsilon_{1,2}\varphi_{1,2}. \tag{A4}$$

The solutions of the time-dependent Schrödinger equation

$$\hat{H}\psi(t) = i\partial_t \psi(t) \tag{A5}$$

are superpositions of the eigenstates

$$\psi(t) = a_1 \exp(-i\varepsilon_1 t)\varphi_1 + a_2 \exp(-i\varepsilon_2 t)\varphi_2. \tag{A6}$$

For a time-dependent state starting localized on the first lattice site,

$$\begin{pmatrix} 1 \\ 0 \end{pmatrix} = \psi(0) = a_1\varphi_1 + a_2\varphi_2, \tag{A7}$$

we find

$$a_1 = -a_2 = \frac{1}{2\sqrt{V^2 + 4J^2}}. \tag{A8}$$

The hopping probability is the absolute square of the time-dependent state at the second lattice site,

$$p(t, V) = |\psi_2(t)|^2 \tag{A9}$$

$$= \frac{4J^2}{V^2 + 4J^2} \sin^2\left(\frac{\sqrt{V^2 + 4J^2}}{2} t\right). \tag{A10}$$

APPENDIX B: TOPOLOGICAL INVARIANT

In the following, we discuss the topological properties of the Hamiltonian (1). Especially the state propagating along the diagonal potential for specific $V^{(n)}_{\mathrm{dia},0}$ [Eq. (7)] seems peculiar as the diagonal is not a boundary between topologically different bulks and is therefore not expected to host any edge states. However, we argue that at these $V^{(n)}_{\mathrm{dia},0}$ the diagonal potential decouples the bulk on either side of the diagonal, and the invariant of our Hamiltonian (1) without the diagonal potential can describe the edge state.

One might guess that interpreting the diagonal potential as a defect, the state along the diagonal is, in fact, a defect edge state. We explicitly start from the winding number defined on defect Hamiltonians to show that this cannot be the case.

The Altland-Zirnbauer classification [32] has been adopted to Floquet systems with defects [33]. The overall structure of the periodic table of static topological insulators/superconductors remains the same. However, the Floquet invariants are now winding numbers associated with the band gaps at quasienergy ε of the time evolution operator $U(\mathbf{k}, \mathbf{r}, t)$, where $\mathbf{r}$ describes the positional dependence of the time evolution operator. Notably, because the quasienergy spectrum is periodic, there is an additional band gap at $\varepsilon T = \pm\pi$. More specifically, because the time evolution operator is generally not periodic in time, one can calculate the Floquet invariant through a periodized time evolution operator U_ε [33]:

$$U_\varepsilon(\mathbf{k}, \mathbf{r}, t) = U(\mathbf{k}, \mathbf{r}, t) \exp\left(itH_{\mathrm{eff},\varepsilon}(\mathbf{k}, \mathbf{r})\right) \tag{B1}$$

with

$$H_{\mathrm{eff},\varepsilon}(\mathbf{k}, \mathbf{r}) = \frac{i}{T} \ln_{-\varepsilon}\left(U(\mathbf{k}, \mathbf{r}, T)\right). \tag{B2}$$

The subscript epsilon denotes the branch cut of the complex logarithm so that $\ln_{-\varepsilon}(e^{i\phi}) = i\phi$ for $-\varepsilon T - 2\pi < \phi < -\varepsilon T$. Setting it to a quasienergy value inside the band gap ensures U_ε is a continuous function.

The topological classification in each symmetry class is then only dependent on the difference between the spatial dimension d_s and the defect dimension d_d. The dimension of the defect is the dimension of the circle S^{d_d} enclosing the defect. For example, a point defect in three dimensions (3D) can be enclosed by a 3D sphere S^3. A line defect in 2D (such as the modified diagonal in our system) is enclosed by S^0, which are only two points (± 1) in the plane on either side of the defect.

Our Hamiltonian and its corresponding time evolution operator U_ε do not possess time reversal, charge conjugation, or chiral symmetry, nor do we enforce any other symmetries (e.g., crystal symmetries). Therefore, the system belongs to the complex symmetry class A, for which topologically nontrivial phases exist if $d_s - d_d$ is even. The 2D winding number with our $d_d = 0$ defect, given by the diagonal potential, is then the difference of the winding numbers of the bulk on the two sides (± 1) of the defect:

$$W(U_\varepsilon) = W(U_\varepsilon(\mathbf{k}, +1, t)) - W(U_\varepsilon(\mathbf{k}, -1, t)), \tag{B3}$$

where

$$W(U_\varepsilon(\mathbf{k}, \pm 1, t)) = \frac{1}{8\pi^2} \int_{\mathrm{BZ}\times S^1} dk_x dk_y dt \times \mathrm{Tr}\left\{(U_\varepsilon^{-1}\partial_t U_\varepsilon)\left[U_\varepsilon^{-1}\partial_{k_x} U_\varepsilon, U_\varepsilon^{-1}\partial_{k_y} U_\varepsilon\right]\right\}. \tag{B4}$$

Here, the square bracket inside the trace denotes the commutator. In our system, there is only a band gap at $\varepsilon T = \pi$, as (in contrast to [23]) we do not have any bipartite on-site potential

in the bulk. We find the winding number

$$W(U_{\pi/T}(\mathbf{k}, \pm 1, t)) = \begin{cases} 1, & \pi < JT < 6.9\pi \\ 0, & \text{else} \end{cases} \tag{B5}$$

identical to the one found by Rudner *et al.* [23] even without the bipartite on-site potential. Because we chose $JT = 2\pi$ in Sec. II, $W(U_{\pi/T}(\mathbf{k}, \pm 1, t)) = 1$.

As the bulk Hamiltonian on both sides of the diagonal potential is equal, we see from (B3) that the observed edge state cannot be a defect edge state. Still, each bulk on its own is topologically nontrivial with our driving parameters. As we have shown in Sec. II B, at $V_{\text{dia},0}^{(n)}$ the probability of the state to hop onto, and hence over the diagonal, is zero after a full period T. Therefore, we interpret a quantum state's inaccessibility to the other side as an isolation of each bulk to an effective system with open boundary conditions. For this system the edge states at the boundary between the bulk to the vacuum is then clearly protected by the winding number $W = 1$.

APPENDIX C: TRACKING STATES

We follow states through changing parameters, e.g., in the closed interval $[V_{\text{dia,min}}, V_{\text{dia,max}}]$. As a starting point, we calculate the Floquet energies $\varepsilon_{0,j}$ and states $\psi_{0,j}$ ($j = 1, 2, \ldots, N^2$) at $V_0 = V_{\text{dia,min}}$. Then we loop through the following procedure: We increase the diagonal potential to $V_i = V_{i-1} + \delta$, with $0 < \delta \leqslant V_{\text{dia,max}} - V_{\text{dia,min}}$, and calculate the new Floquet energies $\varepsilon_{i,k}$ and states $\psi_{i,k}$ ($k = 1, 2, \ldots, N^2$). We compare each of the states $\psi_{i,k}$ to all states $\psi_{i-1,j}$ from the previous step by calculating their overlap (scalar product). The index l of the most similar previous state $\psi_{i-1,l}$ (with $|\psi_{i,k}\psi_{i-1,l}| \geqslant |\psi_{i,k}\psi_{i-1,j}|\ \forall j$) is stored in a similarity variable $s_{i,k} = l$.

If the mapping of states from the previous parameter V_{i-1} to the current parameter V_i is not bijective, i.e., $s_{i,k} = s_{i,k'}$ for $k \neq k'$ [as shown in Fig. 7(a)], we cannot follow the states because they have changed too much. In this case, δ must be decreased (in our calculations to $\delta' = \delta/10$), and the step repeated for $V_i = V_{i-1} + \delta'$.

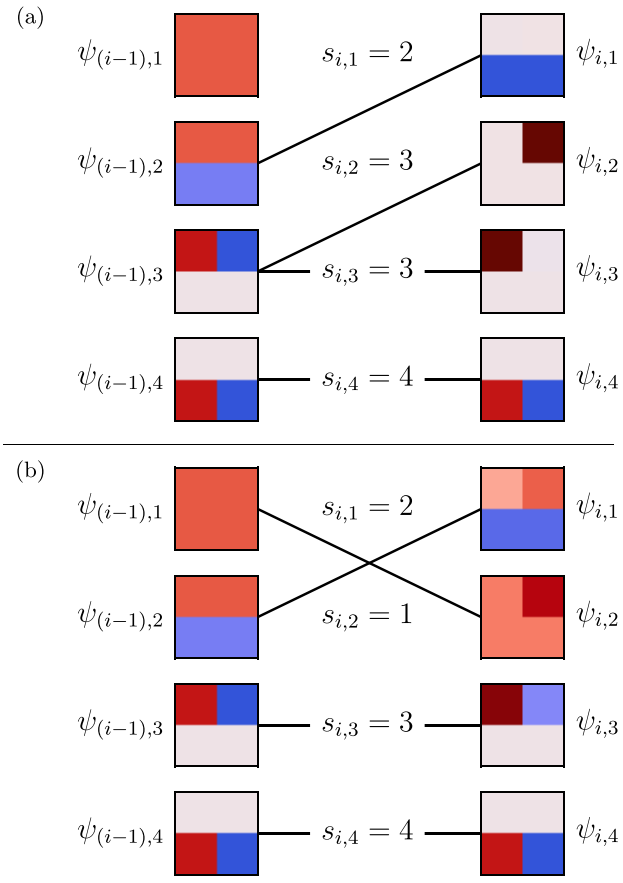

FIG. 7. (a) Example of tracking algorithm failure. Both $\psi_{i,2}$ and $\psi_{i,3}$ are most similar to (i.e., have the largest overlap with) the same state $\psi_{(i-1),3}$ from the previous step ($s_{i,2} = s_{i,3} = 3$). We need to unambiguously track the evolution of $\psi_{(i-1),3}$. Therefore, we must repeat the step from $i-1$ to i using a smaller step size. (b) Example of tracking algorithm success. The states $\psi_{(i-1),j}$ map biuniquely to the states $\psi_{i,k}$ ($j, k = 1, 2, 3, 4$).

If the mapping was successful [Fig. 7(b)], δ may be kept constant or increased before the next step to V_{i+1}. We repeat these steps until we reach $V_{\text{dia,max}}$.

This adaptive-stepsize tracking works for nonzero diagonal potentials but breaks down at $V_{\text{dia}} = 0$, where the doublon states all collapse to localized bulk states at $\varepsilon_{\text{F}} = 0$ and cannot be followed.

[1] M. Z. Hasan and C. L. Kane, *Colloquium*: Topological insulators, Rev. Mod. Phys. **82**, 3045 (2010).
[2] X.-L. Qi and S.-C. Zhang, Topological insulators and superconductors, Rev. Mod. Phys. **83**, 1057 (2011).
[3] T. Oka and H. Aoki, Photovoltaic Hall effect in graphene, Phys. Rev. B **79**, 081406(R) (2009).
[4] T. Kitagawa, E. Berg, M. Rudner, and E. Demler, Topological characterization of periodically driven quantum systems, Phys. Rev. B **82**, 235114 (2010).
[5] N. H. Lindner, G. Refael, and V. Galitski, Floquet topological insulator in semiconductor quantum wells, Nat. Phys. **7**, 490 (2011).
[6] G. Jotzu, M. Messer, R. Desbuquois, M. Lebrat, T. Uehlinger, D. Greif, and T. Esslinger, Experimental realization of the topological Haldane model with ultracold fermions, Nature (London) **515**, 237 (2014).
[7] K. Wintersperger, C. Braun, F. N. Ünal, A. Eckardt, M. D. Liberto, N. Goldman, I. Bloch, and M. Aidelsburger,

Realization of an anomalous Floquet topological system with ultracold atoms, Nat. Phys. **16**, 1058 (2020).
[8] N. R. Cooper, J. Dalibard, and I. B. Spielman, Topological bands for ultracold atoms, Rev. Mod. Phys. **91**, 015005 (2019).
[9] M. Segev and M. A. Bandres, Topological photonics: Where do we go from here?, Nanophotonics **10**, 425 (2021).
[10] T. Ozawa, H. M. Price, A. Amo, N. Goldman, M. Hafezi, L. Lu, M. C. Rechtsman, D. Schuster, J. Simon, O. Zilberberg, and I. Carusotto, Topological photonics, Rev. Mod. Phys. **91**, 015006 (2019).
[11] M. S. Kirsch, Y. Zhang, M. Kremer, L. J. Maczewsky, S. K. Ivanov, Y. V. Kartashov, L. Torner, D. Bauer, A. Szameit, and M. Heinrich, Nonlinear second-order photonic topological insulators, Nat. Phys. **17**, 995 (2021).
[12] S. K. Ivanov, Y. V. Kartashov, M. Heinrich, A. Szameit, L. Torner, and V. V. Konotop, Topological dipole Floquet solitons, Phys. Rev. A **103**, 053507 (2021).
[13] M. C. Rechtsman, J. M. Zeuner, Y. Plotnik, Y. Lumer, D. Podolsky, F. Dreisow, S. Nolte, M. Segev, and A. Szameit, Photonic Floquet topological insulators, Nature (London) **496**, 196 (2013).
[14] M. Hafezi, S. Mittal, J. Fan, A. Migdall, and J. M. Taylor, Imaging topological edge states in silicon photonics, Nat. Photonics **7**, 1001 (2013).
[15] Y.-G. Peng, C.-Z. Qin, D.-G. Zhao, Y.-X. Shen, X.-Y. Xu, M. Bao, H. Jia, and X.-F. Zhu, Experimental demonstration of anomalous Floquet topological insulator for sound, Nat. Commun. **7**, 13368 (2016).
[16] R. Fleury, A. B. Khanikaev, and A. Alù, Floquet topological insulators for sound, Nat. Commun. **7**, 11744 (2016).
[17] J. K. Asbóth, B. Tarasinski, and P. Delplace, Chiral symmetry and bulk-boundary correspondence in periodically driven one-dimensional systems, Phys. Rev. B **90**, 125143 (2014).
[18] V. Dal Lago, M. Atala, and L. E. F. Foa Torres, Floquet topological transitions in a driven one-dimensional topological insulator, Phys. Rev. A **92**, 023624 (2015).
[19] G. M. Graf and C. Tauber, Bulk–edge correspondence for two-dimensional Floquet topological insulators, Ann. Henri Poincaré **19**, 709 (2018).
[20] F. N. Ünal, A. Eckardt, and R.-J. Slager, Hopf characterization of two-dimensional Floquet topological insulators, Phys. Rev. Res. **1**, 022003(R) (2019).
[21] R. Roy and F. Harper, Periodic table for Floquet topological insulators, Phys. Rev. B **96**, 155118 (2017).
[22] M. S. Rudner and N. H. Lindner, Band structure engineering and non-equilibrium dynamics in Floquet topological insulators, Nat. Rev. Phys. **2**, 229 (2020).
[23] M. S. Rudner, N. H. Lindner, E. Berg, and M. Levin, Anomalous Edge States and the Bulk-Edge Correspondence for Periodically Driven Two-Dimensional Systems, Phys. Rev. X **3**, 031005 (2013).
[24] M. Valiente, Lattice two-body problem with arbitrary finite-range interactions, Phys. Rev. A **81**, 042102 (2010).
[25] M. Di Liberto, A. Recati, I. Carusotto, and C. Menotti, Two-body physics in the Su-Schrieffer-Heeger model, Phys. Rev. A **94**, 062704 (2016).
[26] A. M. Marques and R. G. Dias, Topological bound states in interacting Su–Schrieffer–Heeger rings, J. Phys.: Condens. Matter **30**, 305601 (2018).
[27] P. M. Azcona and C. A. Downing, Doublons, topology and interactions in a one-dimensional lattice, Sci. Rep. **11**, 12540 (2021).
[28] G. Salerno, G. Palumbo, N. Goldman, and M. Di Liberto, Interaction-induced lattices for bound states: Designing flat bands, quantized pumps, and higher-order topological insulators for doublons, Phys. Rev. Res. **2**, 013348 (2020).
[29] W. P. Su, J. R. Schrieffer, and A. J. Heeger, Solitons in Polyacetylene, Phys. Rev. Lett. **42**, 1698 (1979).
[30] See Supplemental Material at http://link.aps.org/supplemental/10.1103/PhysRevResearch.5.023056 for animations of a 20 × 20 system at $p(V_{\mathrm{dia}}) = 0, 0.5$, and 1.
[31] L. J. Maczewsky, M. Heinrich, M. Kremer, S. K. Ivanov, M. Ehrhardt, F. Martinez, Y. V. Kartashov, V. V. Konotop, L. Torner, D. Bauer, and A. Szameit, Nonlinearity-induced photonic topological insulator, Science **370**, 701 (2020).
[32] A. Altland and M. R. Zirnbauer, Nonstandard symmetry classes in mesoscopic normal-superconducting hybrid structures, Phys. Rev. B **55**, 1142 (1997).
[33] S. Yao, Z. Yan, and Z. Wang, Topological invariants of Floquet systems: General formulation, special properties, and Floquet topological defects, Phys. Rev. B **96**, 195303 (2017).

9. High-harmonic spectra of hexagonal nanoribbons from real-space time-dependent Schrödinger calculations

H. Drüeke and D. Bauer: "High-harmonic spectra of hexagonal nanoribbons from real-space time-dependent Schrödinger calculations" *The European Physical Journal Special Topics* 230.23 (2021), 4065–4070 DOI: 10.1140/epjs/s11734-021-00188-9

with additional material at

H. Drüeke and D. Bauer: "High-harmonic spectra of hexagonal nanoribbons from real-space time-dependent Schrödinger calculations: data repository" *Open Science Framework* (2021) DOI: 10.17605/osf.io/8rtfu

Eur. Phys. J. Spec. Top. (2021) 230:4065–4070
https://doi.org/10.1140/epjs/s11734-021-00188-9

THE EUROPEAN PHYSICAL JOURNAL SPECIAL TOPICS

Regular Article

High-harmonic spectra of hexagonal nanoribbons from real-space time-dependent Schrödinger calculations

Helena Drüeke[a] and Dieter Bauer[b]

University of Rostock, Rostock, Germany

Received 18 January 2021 / Accepted 31 May 2021 / Published online 21 June 2021

Abstract High-harmonic spectroscopy is a promising candidate for imaging electronic structures and dynamics in condensed matter by all-optical means and with unprecedented temporal resolution. We investigate harmonic spectra from finite, hexagonal nanoribbons, such as graphene and hexagonal boron nitride, in armchair and zig-zag configuration. The symmetry of the system explains the existence and intensity of the emitted harmonics.

1 Introduction

High-harmonic generation (HHG) has been first observed in gases [1,2]. Its non-perturbative nature, featuring a plateau of almost constant high-harmonic yield, was subsequently explained by the three-step model [3,4]: An electron is removed from the atom, propagates under the external field's influence, and recombines with the atom. The orbital energies of electrons in atoms do not depend on momentum, and the electron's dispersion relation in the continuum is shaped parabolically. Therefore, electrons in the ground state or free electrons emit no harmonics. Only transitions between bound states or recombination from continuum states back to bound states lead to harmonic emission.

To describe HHG in the bulk of solids, electronic bands replace the orbital energies and the continuum [5]. This opens a whole new field of research [6–13]. Analogous to the HHG process in gases, the transition of electrons between valence and conduction bands causes high harmonics, called interband harmonics. Intraband harmonics, on the other hand, are produced by the movement of electrons in partially filled, non-parabolic bands. Band structures are usually defined for periodic or infinite solid bulk systems. However, every realistic system has boundaries, which may cause completely different HHG spectra compared to the bulk [14–18]. Graphene and hexagonal boron nitride (hBN) are two-dimensional materials that possess fascinating features with promising potential applications [19,20]. Their hexagonal structure allows for two different edges: zig-zag and armchair. While graphene contains only carbon atoms (all identical), hBN consists of boron and nitrogen atoms. Recently, the interaction of intense-laser light with graphene got into the focus of interest for its prospects to steer electrons at will on ultrafast time scales [21–24].

In this article, we investigate the harmonic spectra emitted by hexagonal nanoribbons in two different edge configurations, armchair (Sect. 3) and zig-zag (Sect. 4). We performed our calculations using a real-space time-dependent Schrödinger solver (as described in Sect. 2). The results of this publication validate the tight-binding approach in [25].

2 Methods

The nanoribbons' N_{ions} atomic nuclei were positioned in a hexagonal lattice, as described for the armchair and zig-zag configuration in Sects. 3 and 4. Atomic units are used throughout this paper unless stated otherwise. The distance between neighboring lattice sites was 2.683, the bond length in graphene (1.42Å). An effective Pöschl–Teller potential

$$V(\mathbf{r}) = -\sum_i \frac{V_i}{\cosh^2(\varepsilon|\mathbf{r}-\mathbf{r}_i|)} \tag{1}$$

with ion potentials $V_i = 3.2 \pm V_{\text{os}}$ and screening parameter $\varepsilon = 2$ describe the attractive potentials of the nuclei. For graphene ribbons, all atoms are carbon, therefore the additional on-site potential $V_{\text{os}} = 0$. A non-zero on-site potential represents two alternating, different kind of atoms, such as boron and nitrogen in hBN. Figures 1 and 4 show at which lattice sites the ion potentials are increased or decreased by V_{os}.

In this work, we did not employ the usual tight-binding approximation commonly made in condensed-matter theory. Instead, we have developed a 2D, real-

[a] e-mail: helena.drueeke@uni-rostock.de (corresponding author)
[b] e-mail: dieter.bauer@uni-rostock.de

space, time-dependent Schrödinger solver for the *ab initio* simulation of the intense-laser interaction with 2D matter. In that way, we can reveal differences and similarities in HHG spectra as compared to corresponding tight-binding studies, e.g., in Ref. [25]. The non-interacting electronic orbitals in our Schrödinger solver are defined on a two-dimensional grid of spacing $\Delta x = \Delta y = 0.2$, which encompasses all lattice sites plus a border of 8 on each side. In contrast to the usual tight-binding description, this allows us to have electron orbitals φ_i (with energies E_i) that are not only localized at lattice sites but also between them, or free electrons.

The electronic eigenstates of the system were found by imaginary-time propagation of the time-dependent Schrödinger equation

$$\mathrm{i}\partial_t \varphi_i(\mathbf{r},t) = \left[-\frac{1}{2}\nabla^2 + V(\mathbf{r})\right]\varphi_i(\mathbf{r},t) \tag{2}$$

employing the Crank–Nicolson method [26]. Starting from a random initialization, imaginary timesteps $-0.05\mathrm{i}$ are taken (each step followed by renormalization of the wavefunction) until the ground state is reached and the relative change of the state is smaller than the threshold of 10^{-18} for two consecutive iterations. To find the higher-lying states, the workflow is identical but with an additional (Gram-Schmidt) orthogonalization to all previously found states in each iteration. This procedure gives us all states of interest in the unperturbed system.

Real-time simulations of the interaction of all occupied electronic orbitals with a short laser pulse were performed with a timestep 0.05 using, again, Crank–Nicolson propagation. The pulse was a $n_{\mathrm{cyc}} = 4$ cycle $\sin^2$-shaped laser pulse of frequency $\omega = 0.0075$ ($\lambda \simeq 6.1\mathrm{mm}$) with vector potential

$$A(t) = A_0 \sin^2\left(\frac{\omega t}{2n_{\mathrm{cyc}}}\right)\sin\omega t \tag{3}$$

for $0 < t < 2\pi n_{\mathrm{cyc}}/\omega$ and zero otherwise. The electronic dipoles were recorded at each time step during the laser pulse and added up according to

$$\mathbf{P}(t) = 2\sum_{i=1}^{N_{\mathrm{occupied}}}\int \mathbf{r}|\varphi_i(\mathbf{r},t)|^2\,\mathrm{d}\mathbf{r}, \tag{4}$$

where $N_{\mathrm{occupied}} = N_{\mathrm{ions}}/2$ is the number of occupied orbitals, each occupied by a spin-up and a spin-down electron. Harmonic spectra were calculated as the absolute square of the Fourier transform of the recorded dipoles, multiplied by a symmetric Hann window [27,28].

3 Armchair ribbon

First, we investigate a hexagonal nanoribbon in the armchair configuration. A total of 24 lattice sites are arranged in the shape of four hexagons, as shown in Fig. 1. For $V_{\mathrm{os}} = 0$, the armchair ribbon is symmetric about the horizontal as well as the vertical axis through the center. The introduction of an on-site potential deepens the blue (square) sites' potentials while making the orange (circle) ones shallower. This causes a left-right asymmetry, while the top–bottom symmetry is conserved. These (a)symmetries of the system are present for ribbons consisting of both even and odd numbers of hexagons. Calculations for a ribbon of 30 sites arranged in five hexagons are consistent with the results shown here.

Note that the lines drawn in Fig. 1 connect nearest neighbors. In tight-binding calculations (such as in Ref. [25]), hopping takes place along these lines. However, in our simulation based on the time-dependent Schrödinger equation, electronic wavefunctions are not restricted to move along these lines but may propagate in the entire plane.

The asymmetry in the potential leads to an asymmetry in the orbitals. Figure 2a shows the highest occupied (1 and 3) and lowest unoccupied (2 and 4) orbitals without (1 and 2) and with (3 and 4) on-site potential. The orbitals without on-site potential are horizontally and vertically symmetric (as is the potential), and there is only a small bandgap between the occupied and unoccupied states. With an on-site potential, the occupied orbitals are localized on the sites with deeper potentials and therefore have a decreased energy. The unoccupied orbitals are localized on the sites with shallower potentials and therefore have increased energy. This leads to a bandgap ΔE_{min} between the occupied and unoccupied orbitals, which, for $V_{\mathrm{os}} \gtrsim 0.2$, grows linearly with the on-site potential (Fig. 3b). In contrast to tight-binding methods, our approach allows us to calculate an arbi-

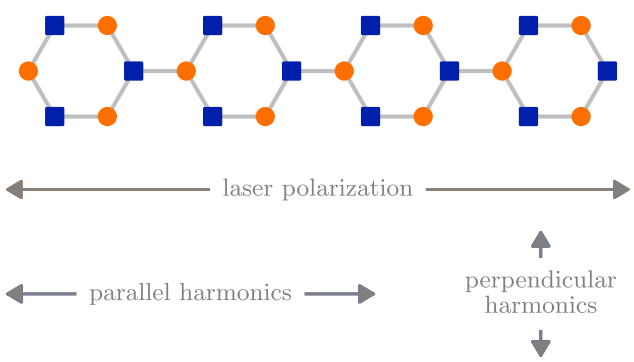

Fig. 1 Armchair ribbon: At the blue (square) lattice sites, the potential depth is increased by the on-site potential, $V_{\mathrm{blue}} = V_{\mathrm{avg}} + V_{\mathrm{os}}$. The orange (circle) sites correspond to the shallower potentials of depth $V_{\mathrm{orange}} = V_{\mathrm{avg}} - V_{\mathrm{os}}$. The arrows indicate the polarization directions of the external laser field (along the ribbon) and the harmonics referred to as parallel and perpendicular

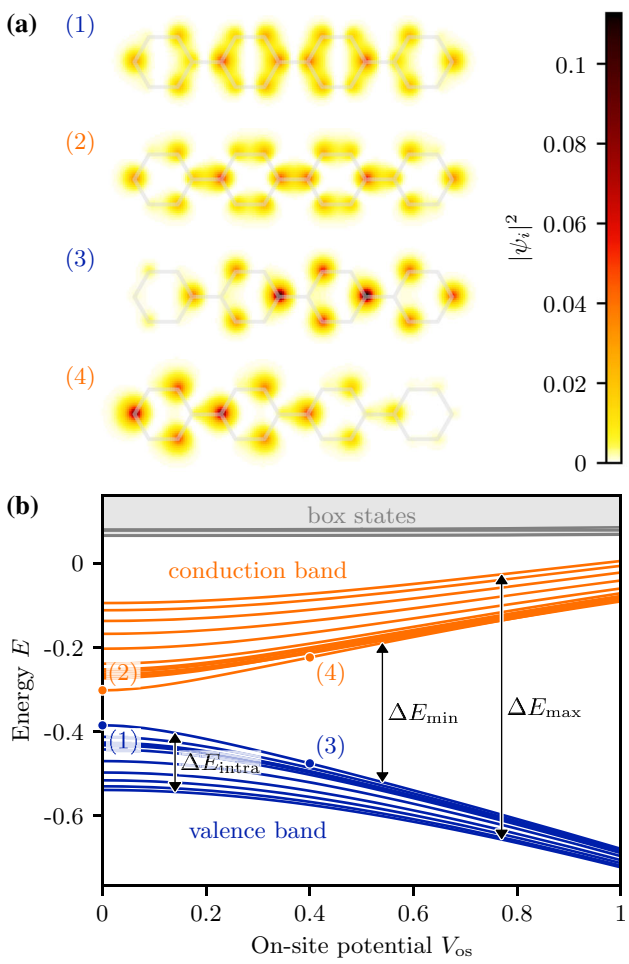

Fig. 2 Orbitals and orbital energies of the armchair ribbon. **a** Orbitals of the armchair ribbon. (1) Highest occupied orbital without on-site potential ($V_{\text{os}} = 0$). (2) Lowest unoccupied orbital without on-site potential ($V_{\text{os}} = 0$). (3) Highest occupied orbital with on-site potential $V_{\text{os}} = 0.4$. (4) Lowest unoccupied orbital with on-site potential $V_{\text{os}} = 0.4$. **b** Orbital energies of the armchair ribbon as a function of on-site potential V_{os}. Circles mark the orbital energies of the orbitals shown in (**a**). The orbitals form three bands: occupied valence band (blue), unoccupied conduction band (orange), and box states (gray). The gray shaded area indicates additional box states lying above those shown explicitly. The arrows mark the bandwidth of the valence band (ΔE_{intra}) and the minimum and maximum bandgap between the valence and (first) conduction band (ΔE_{min} and ΔE_{max})

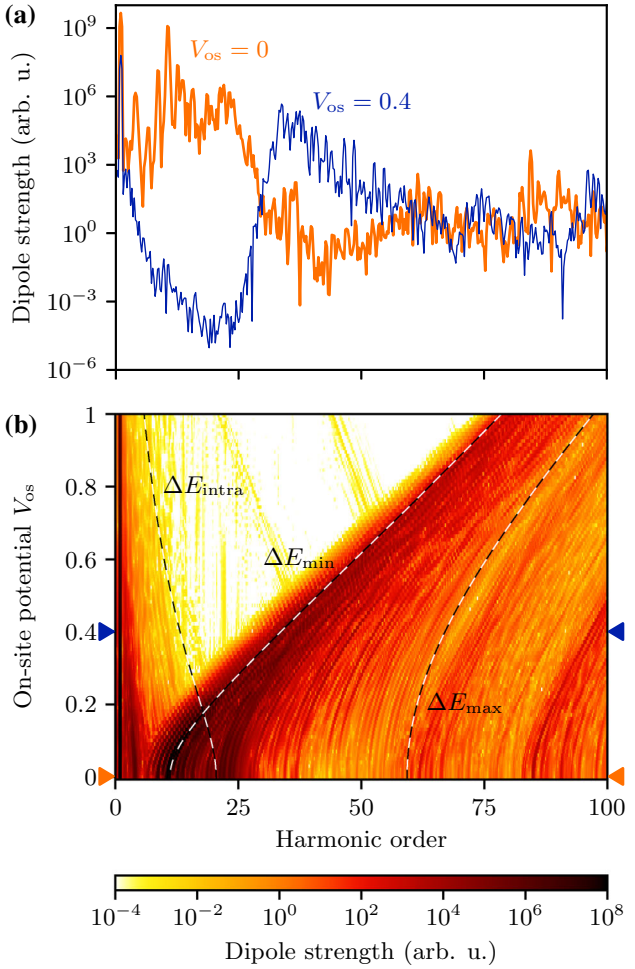

Fig. 3 Harmonic spectra of the armchair ribbon in parallel direction. **a** Harmonic spectra without (bold orange line, $V_{\text{os}} = 0$) and with (blue line, $V_{\text{os}} = 0.4$) on-site potential. **b** Harmonic spectra as a function of harmonic order and on-site potential. The bandwidth ΔE_{intra} of the valence band is the upper bound of the intraband harmonics. The minimum (ΔE_{min}) and maximum (ΔE_{max}) bandgaps limit the energies of the interband harmonics. Transitions to the box states generate harmonics above ΔE_{max}. Triangles of the corresponding colors indicate the energies of the two spectra shown in (**a**)

trary number of orbitals of increasing energy. The states above the conduction band describe "free" electrons, which are not localized on the ribbon but still inside the simulation box with reflecting boundary conditions.

The incoming laser field is linearly polarized along the armchair ribbon. All emitted harmonics are linearly polarized in the same direction (parallel harmonics, as indicated in Fig. 1). The armchair ribbon is top–bottom symmetric, regardless of on-site potential. Without a top–bottom asymmetry in the system, the horizontally polarized laser leads to a perfectly horizontal movement of the electrons, which generates only horizontally polarized harmonics. Therefore, the armchair ribbon can not generate perpendicular harmonics. The bandwidths and bandgaps (ΔE_{intra}, ΔE_{min}, and ΔE_{max}) from Fig. 2b explain the most important features of the harmonic spectra shown in Fig. 3. Intraband harmonics are only present at harmonic energies below the width of the valence band ΔE_{intra}. Interband harmonics appear between the minimum ΔE_{min} and maximum ΔE_{max} bandgap between the valence and (first) conduction band. Above the two bands are the box states (marked as gray lines in Fig. 2b), which are not localized on the ribbon, and whose energies are determined

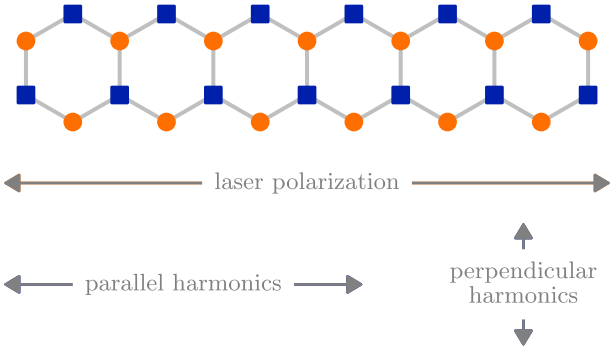

Fig. 4 Zig-zag ribbon: At the blue (square) lattice sites, the potential depth is increased by the on-site potential, $V_{\text{blue}} = V_{\text{avg}} + V_{\text{os}}$. The orange (circle) sites correspond to the shallower potentials of depth $V_{\text{orange}} = V_{\text{avg}} - V_{\text{os}}$. The arrows indicate the polarization directions of the external laser field (along the ribbon) and the harmonics referred to as parallel and perpendicular

by the size of the simulation box. The figure only shows the energies of the four lowest box states (which are pairwise almost degenerate), but many more lie above them, indicated by the gray shaded area. Transitions to these box states cause harmonics above ΔE_{max}. In an experiment, transitions to higher bands or the continuum would cause harmonics beyond the maximum bandgap. These can not be described in tight-binding approximation with one atomic orbital per site, because then the energy difference between states is bound from above by ΔE_{max} (see Ref. [25]).

4 Zig-zag ribbon

In the zig-zag configuration, a total of 26 lattice sites are arranged in six hexagons, as shown in Fig. 4. On the orange (circle) sites, the on-site potential decreases the potential depth, while on the blue (square) sites, it deepens the potential. The on-site potential causes a top–bottom asymmetry but no left-right asymmetry. Reference [25] investigates the influence of the ribbon's length using a computationally less demanding tight-binding approach. Full time-dependent Schrödinger calculation results for a ribbon of 30 sites (seven hexagons) agree with those for 26 sites (six hexagons).

As for the armchair ribbon, the asymmetry of the potential leads to decreased energies of states in the valence band, localized at the deeper sites, and increased energies of states in the conduction bands, localized at the shallower sites (see Fig. 5). The minimum bandgap increases almost linearly with the on-site potential; the bandwidths of both bands decrease.

The parallelly polarized harmonics (Fig. 6a) are present with and without on-site potential. The bandwidth and bandgaps can explain the cutoffs of both intra- and interband harmonics. Perpendicular harmonics (Fig. 6b) with on-site potential agree with these cutoffs, as well. Without an on-site potential, there is no

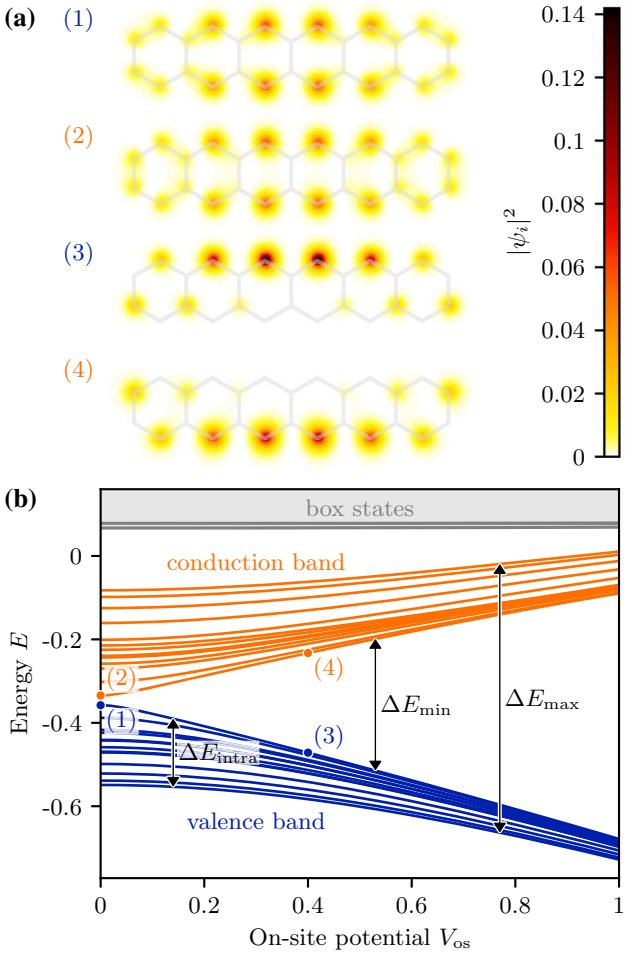

Fig. 5 Orbitals and orbital energies of the zig-zag ribbon. **a** Orbitals of the zig-zag ribbon. (1) Highest occupied orbital without on-site potential ($V_{\text{os}} = 0$). (2) Lowest unoccupied orbital without on-site potential ($V_{\text{os}} = 0$). (3) Highest occupied orbital with on-site potential $V_{\text{os}} = 0.4$. (4) Lowest unoccupied orbital with on-site potential $V_{\text{os}} = 0.4$. **b** Orbital energies of the zig-zag ribbon as a function of on-site potential V_{os}. Circles mark the orbital energies of the orbitals shown in (**a**). The orbitals form three bands: occupied valence band (blue), unoccupied conduction band (orange), and box states (gray). The gray shaded area indicates additional box states lying above those shown explicitly. The arrows mark the bandwidth of the valence band (ΔE_{intra}) and the minimum and maximum bandgap between the valence and (first) conduction band (ΔE_{min} and ΔE_{max})

top–bottom asymmetry, and therefore, almost no harmonics perpendicular to the laser are observed. Transitions to the box states lead to weak harmonic emission above ΔE_{max}.

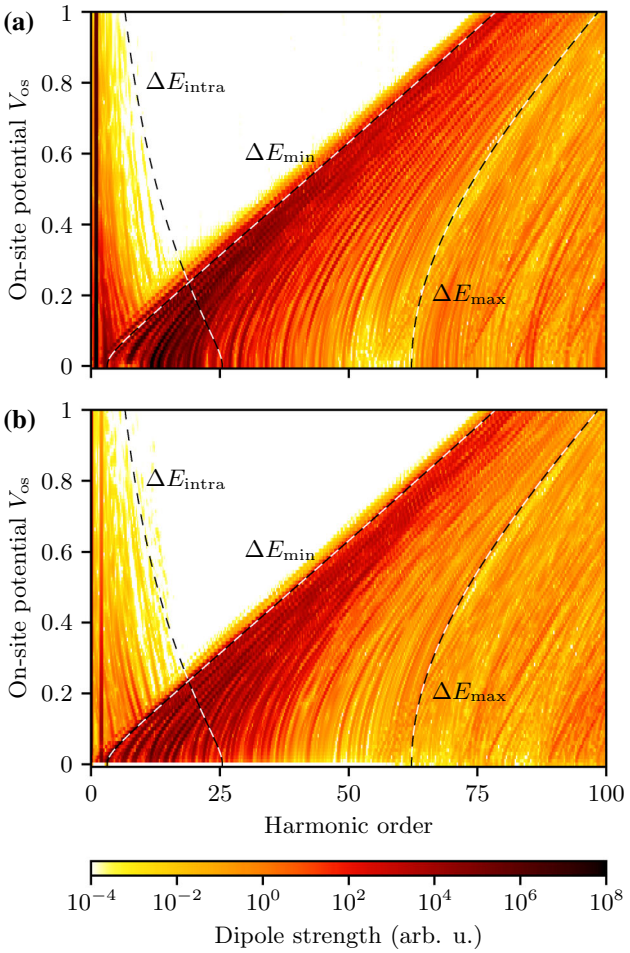

Fig. 6 Harmonic spectra of the zig-zag ribbon as a function of on-site potential in **a** parallel and **b** perpendicular polarization. The bandwidth ΔE_{intra} of the valence band is the upper bound of the intraband harmonics. The minimum (ΔE_{min}) and maximum (ΔE_{max}) bandgaps limit the energies of the interband harmonics. Transitions to the box states generate harmonics above ΔE_{max}

5 Conclusion

The introduction of an on-site potential in hexagonal nanoribbons causes lower energies for occupied states and higher energies for unoccupied states. The valence band's bandwidth decreases, and the minimum and maximum bandgaps between the valence and conduction bands increase. These three energies explain the overall features in harmonic spectra for different on-site potentials. Intraband harmonics are only present at energies below the valence bandwidth. Interband harmonics are present at energies between the minimum and maximum bandgaps. For a laser polarized along the ribbon, the resulting harmonics are polarized in the same direction unless a non-zero on-site potential causes a top–bottom asymmetry, which is only possible in the zig-zag ribbon.

The results of this paper provide valuable verification of simpler tight-binding models [25]. Our approach is not limited to a fixed number of states (grouped in bands), and our results account for transitions to even higher bands or the continuum. However, these transitions are expected to play an important role only in the generation of higher harmonics beyond the cutoff ΔE_{max}, leading to higher order plateaus with decreasing yield (see, e.g., [29]). On the other hand, tight-binding approaches capture the essential mechanisms underlying high-harmonic generation up to ΔE_{max}, are computationally much less demanding, and thus can be used to investigate much larger systems.

The datasets generated and analyzed during this study are available at Ref. [30].

Funding Open Access funding enabled and organized by Projekt DEAL.

Author contribution statement

HD performed the numerical calculations, analyzed and discussed the results, and wrote the manuscript. DB supervised the project, discussed the results, and provided feedback on the manuscript.

References

1. A. McPherson, G. Gibson, H. Jara, U. Johann, T.S. Luk, I.A. McIntyre, K. Boyer, C.K. Rhodes, Studies of multiphoton production of vacuum-ultraviolet radiation in the rare gases. JOSA B **4**, 595–601 (1987). https://doi.org/10.1364/JOSAB.4.000595
2. M. Ferray, A. L'Huillier, X.F. Li, L.A. Lompre, G. Mainfray, C. Manus, Multiple-harmonic conversion of 1064 nm radiation in rare gases. J. Phys. B Atom. Mol. Opt. Phys. **21**, L31–L35 (1988). https://doi.org/10.1088/0953-4075/21/3/001
3. P.B. Corkum, Plasma perspective on strong field multiphoton ionization. Phys. Rev. Lett. **71**, 1994–1997 (1993). https://doi.org/10.1103/PhysRevLett.71.1994
4. M. Lewenstein, P. Balcou, M.Y. Ivanov, A. L'Huillier, P.B. Corkum, Theory of high-harmonic generation by low-frequency laser fields. Phys. Rev. A **49**, 2117–2132 (1994). https://doi.org/10.1103/PhysRevA.95.043416

5. G. Vampa, T. Brabec, Merge of high harmonic generation from gases and solids and its implications for attosecond science. J. Phys. B Atom. Mol. Opt. Phys. **50**, 083001 (2017). https://doi.org/10.1088/1361-6455/aa528d
6. S. Ghimire, A.D. DiChiara, E. Sistrunk, P. Agostini, L.F. DiMauro, D.A. Reis, Observation of high-order harmonic generation in a bulk crystal. Nat. Phys. **7**, 138–141 (2011). https://doi.org/10.1038/nphys1847
7. S. Ghimire, A.D. DiChiara, E. Sistrunk, G. Ndabashimiye, U.B. Szafruga, A. Mohammad, P. Agostini, L.F. DiMauro, D.A. Reis, Generation and propagation of high-order harmonics in crystals. Phys. Rev. A **85**, 043836 (2012). https://doi.org/10.1103/PhysRevA.85.043836
8. S. Ghimire, G. Ndabashimiye, A.D. DiChiara, E. Sistrunk, M.I. Stockman, P. Agostini, L.F. DiMauro, D.A. Reis, Strong-field and attosecond physics in solids. J. Phys. B Atom. Mol. Opt. Phys. **47**(20), 204030 (2014). http://stacks.iop.org/09534075/47/i=20/a=204030
9. M. Hohenleutner, F. Langer, O. Schubert, M. Knorr, U. Huttner, S.W. Koch, M. Kira, R. Huber, Real-time observation of interfering crystal electrons in high-harmonic generation. Nature **523**, 572–575 (2015). https://doi.org/10.1038/nature14652
10. G. Ndabashimiye, S. Ghimire, M. Wu, D.A. Browne, K.J. Schafer, M.B. Gaarde, D.A. Reis, Solid-state harmonics beyond the atomic limit. Nature **534**, 520–523 (2016). https://doi.org/10.1038/nature17660
11. T. Ikemachi, Y. Shinohara, T. Sato, J. Yumoto, M. Kuwata-Gonokami, K.L. Ishikawa, Trajectory analysis of high-order-harmonic generation from periodic crystals. Phys. Rev. A **95**, 043416 (2017). https://doi.org/10.1103/PhysRevA.95.043416
12. Y.S. You, Y. Yin, Y. Wu, A. Chew, X. Ren, F. Zhuang, S. Gholam-Mirzaei, M. Chini, Z. Chang, S. Ghimire, High-harmonic generation in amorphous solids. Nat. Commun. **8**, 724 (2017). https://doi.org/10.1038/s41467-017-00989-4
13. C. Yu, K.K. Hansen, L.B. Madsen, High-order harmonic generation in imperfect crystals. Phys. Rev. A **99**, 063408 (2019). https://doi.org/10.1103/PhysRevA.99.063408
14. D. Bauer, K.K. Hansen, High-harmonic generation in solids with and without topological edge states. Phys. Rev. Lett. **120**, 177401 (2018). https://doi.org/10.1103/PhysRevLett.120.177401
15. H. Drüeke, D. Bauer, Robustness of topologically sensitive harmonic generation in laser-driven linear chains. Phys. Rev. A **99**, 053402 (2019). https://doi.org/10.1103/PhysRevA.99.053402
16. C. Jürß, D. Bauer, High-harmonic generation in Su-Schrieffer-Heeger chains. Phys. Rev. B **99**, 195428 (2019). https://doi.org/10.1103/PhysRevB.99.195428
17. K.K. Hansen, D. Bauer, L.B. Madsen, Finite-system effects on high-order harmonic generation: From atoms to solids. Phys. Rev. A **97**, 043424 (2018). https://doi.org/10.1103/PhysRevA.97.043424
18. A. Chacón, W. Zhu, S.P. Kelly, A. Dauphin, E. Pisanty, D. Kim, D.E. Kim, A. Picón, C. Ticknor, M.F. Ciappina, A. Saxena, M. Lewenstein, Observing topological phase transitions with high harmonic generation. arXiv:1807.01616 (2020)
19. A.H. Castro Neto, F. Guinea, N.M.R. Peres, K.S. Novoselov, A.K. Geim, The electronic properties of graphene. Rev. Mod. Phys. **81**, 109–162 (2009). https://doi.org/10.1103/RevModPhys.81.109
20. J. Wang, F. Ma, M. Sun, Graphene, hexagonal boron nitride, and their heterostructures: properties and applications. RSC Adv. **7**(27), 16801–16822 (2017). https://doi.org/10.1039/C7RA00260B
21. H. Koochaki Kelardeh, V. Apalkov, M.I. Stockman, Graphene superlattices in strong circularly polarized fields: chirality, Berry phase, and attosecond dynamics. Phys. Rev. B **96**, 075409 (2017). https://doi.org/10.1103/PhysRevB.96.075409
22. T. Higuchi, C. Heide, K. Ullmann, H.B. Weber, P. Hommelhoff, Light-field-driven currents in graphene. Nature **550**, 224–228 (2017). https://doi.org/10.1038/nature23900
23. C. Heide, T. Higuchi, H.B. Weber, P. Hommelhoff, Coherent electron trajectory control in graphene. Phys. Rev. Lett. **121**, 207401 (2018). https://doi.org/10.1103/PhysRevLett.121.207401
24. M. Baudisch, A. Marini, J.D. Cox, T. Zhu, F. Silva, S. Teichmann, M. Massicotte, F. Koppens, L.S. Levitov, F.J. García de Abajo, J. Biegert, Ultrafast nonlinear optical response of Dirac fermions in graphene. Nat. Commun. **9** (2018). https://doi.org/10.1038/s41467-018-03413-7
25. C. Jürß, D. Bauer, High-order harmonic generation in hexagonal nanoribbons. Eur. Phys. J. Spec. Top. (2021). https://doi.org/10.1140/epjs/s11734-021-00106-z
26. D. Bauer (ed.), *Computational Strong-Field Quantum Dynamics: Intense Light-Matter Interactions. De Gruyter Textbook* (De Gruyter, Boston, 2017). https://books.google.de/books?id=kwXEDgAAQBAJ
27. J.C. Baggesen, L.B. Madsen, On the dipole, velocity and acceleration forms in high-order harmonic generation from a single atom or molecule. J. Phys. B Atom. Mol. Opt. Phys. **44**(11), 115601 (2011). http://stacks.iop.org/0953-4075/44/i=11/a=115601
28. F.J. Harris, On the use of windows for harmonic analysis with the discrete Fourier transform. Proc. IEEE **66**, 51–83 (1978). https://doi.org/10.1109/PROC.1978.10837
29. K.K. Hansen, T. Deffge, D. Bauer, High-order harmonic generation in solid slabs beyond the single-active-electron approximation. Phys. Rev. A **96**, 053418 (2017). https://doi.org/10.1103/PhysRevA.96.053418
30. H. Drüeke, D. Bauer, High-harmonic spectra of hexagonal nanoribbons from real-space time-dependent Schrödinger calculations: data repository (2021). https://doi.org/10.17605/OSF.IO/8RTFU

Author contribution statements

H. Drüeke and D. Bauer: "Interaction-induced directional transport on periodically driven chains" *Physical Review Research* 6.2 (2024), 023032 DOI: 10.1103/PhysRevResearch.6.023032

Helena Drüeke performed the analytical derivations and numerical calculations, analyzed and discussed the results, prepared the figures, and wrote and revised the manuscript. Dieter Bauer proposed the model system, supervised the project, discussed the results, and provided feedback on the manuscript.

H. Drüeke, M. Meschede, and D. Bauer: "Steering edge currents through a Floquet topological insulator" *Physical Review Research* 5.2 (2023), 023056 DOI: 10.1103/PhysRevResearch.5.023056

Helena Drüeke performed the analytical derivations and numerical calculations, analyzed and discussed the results, prepared the figures, and wrote and revised the manuscript. Marcus Meschede derived the topological invariant and wrote the corresponding appendix. Dieter Bauer supervised the project, discussed the results, and provided feedback on the manuscript.

H. Drüeke and D. Bauer: "High-harmonic spectra of hexagonal nanoribbons from real-space time-dependent Schrödinger calculations" *The European Physical Journal Special Topics* 230.23 (2021), 4065–4070 DOI: 10.1140/epjs/s11734-021-00188-9

Helena Drüeke performed the numerical calculations, analyzed and discussed the results, prepared the figures, and wrote and revised the manuscript. Dieter Bauer supervised the project, discussed the results, and provided feedback on the manuscript.

Danksagung

An dieser Stelle möchte ich mich bei Allen bedanken, die mich unterstützt und diese Arbeit ermöglicht haben.

Zuallererst Prof. Dieter Bauer für seine fachliche Unterstützung und Beratung, für die gemeinsame Ideenentwicklung und sein Feedback. Besonders die Ermöglichung meiner zahlreichen Konferenzbesuche weiß ich sehr zu schätzen.

Der gesamten Arbeitsgruppe Quantentheorie und Vielteilchensysteme danke ich für die kollegiale Zusammenarbeit. Ich danke Frau Marina Hertzfeldt für die Unterstützung in allen administrativen Fragen.

Der Studienstiftung des deutschen Volkes danke ich für die finanzielle und ideelle Förderung meines Studiums und meiner Promotion.

Ich danke meiner Familie, dafür dass sie mich immer in meinen Plänen gefördert haben.

Vorallem aber danke ich Till Köster, für seine unermüdliche Unterstützung und Ermutigung.